The Initial Growth of Complex Oxides:
Study and Manipulation

Cover: *Atomic force micrograph of a 50 nm thick $SrRuO_3$ film deposited on a vicinal $SrTiO_3$ substrate, showing a clear step-terrace structure. The roughening of the step edge ledges is a direct result of a "mixed" growth mode. Two-dimensional islands nucleate and grow on the terraces. Coalescence of the propagating steps with these islands results in roughening of the step ledges and a constant step density.*

Samenstelling promotiecommissie:

Voorzitter en secretaris
prof. dr. ir. J.H.A. de Smit (Universiteit Twente)

Promotor
prof. dr. H. Rogalla (Universiteit Twente)

Assistent promotor
dr. ing. D.H.A. Blank (Universiteit Twente)

Leden
prof. dr. J.G. Bednorz (IBM Zurich Research Laboratory, Switzerland)
prof. dr. C.B. Eom (University of Wisconcin-Madison, USA)
prof. dr. J.C. Lodder (Universiteit Twente)
prof. dr. ir. B. Poelsema (Universiteit Twente)
prof. dr. G. Van Tendeloo (Universiteit Antwerpen, België)
prof. dr. E. Vlieg (Katholieke Universiteit Nijmegen)

The work described in this thesis was carried out at the Low Temperature Division of the Department of Applied Physics and MESA$^+$ research institute at the University of Twente, P.O. Box 217, 7500 AE Enschede, the Netherlands.

A.J.H.M. Rijnders
The Initial Growth of Complex Oxides: Study and Manipulation,
Proefschrift Universiteit Twente, Enschede.

ISBN 90-365-1657-9

Druk: Printpartners Ipskamp, Enschede

THE INITIAL GROWTH OF COMPLEX OXIDES: STUDY AND MANIPULATION

PROEFSCHRIFT

ter verkrijging van
de graad van doctor aan de Universiteit Twente,
op gezag van de rector magnificus,
prof. dr. F.A. van Vught,
volgens besluit van het College voor Promoties
in het openbaar te verdedigen
op woensdag 31 oktober 2001 te 15:00 uur

door

Augustinus Josephus Helena Maria Rijnders
geboren op 13 februari 1964
te Lichtenvoorde

Dit proefschrift is goedgekeurd door:

prof. dr. H. Rogalla (promotor) en
dr. ing. D.H.A. Blank (assistent-promotor)

Contents

Chapter 1

Introduction

Complex oxides have attracted great interest since they exhibit a rich spectrum of physical properties such as ferromagnetism, antiferromagnetism, colossal magnetoresistance, ferroelectricity, dielectricity, and superconductivity. Novel heteroepitaxial devices based on these complex oxides, like spin-polarized ferromagnetic tunnel junctions, superconducting devices and piezoelectric devices, have great potential and are currently under investigation in many groups.

The nature of the above-mentioned physical properties in complex oxides is determined by very small characteristic length scales. For instance, the coherence length in cuprate high-T_C superconductors[1] is as small as 10-20 Å[2], comparable to the unit cell lattice parameters of these superconductors[I]. Because of these small characteristic length scales, growth control on an atomic level is essential in epitaxial heterostructures. Furthermore, the terminating atomic layer of each complex oxide thin film in these structures influences the interface properties and, consequently, the device performance. Interfaces therefore play an important role in the physical and electrical properties of the complex oxide devices. Not only growth control, but also interface engineering on an atomic level is essential.

Epitaxial growth of complex oxides involves high growth temperatures. For instance, $REBa_2Cu_3O_{7-\delta}$ (RE123; RE is Y or rare earth element) is grown at temperatures up to 800 °C using a physical vapor deposition (PVD) technique like pulsed laser deposition (PLD)[3,4,5]. Furthermore, the oxidation power during growth should be sufficiently high to enable growth of stable phases[6], which can be

---

[I] Here, the value for the coherence length parallel to the CuO_2 planes is given. The coherence length perpendicular to the CuO_2 planes is even shorter.

achieved using relatively high oxygen pressures, i.e., 10^{-1}-10^{2} Pa. The use of an *in situ* diagnostic tool like reflection high-energy electron diffraction (RHEED) is hampered at these high oxygen pressures due to scattering of the electrons by the ambient gas. With the development of high-pressure RHEED[7], this problem was overcome and real-time growth control at the optimal growth conditions of complex oxides in PLD became feasible. First homoepitaxial growth studies of $SrTiO_3$ with this growth monitoring technique indicated the importance of clean, atomically smooth and crystalline substrate surfaces to obtain defect-free epitaxial growth. To achieve these perfect surfaces, a two-step chemical surface treatment was developed resulting in an atomically smooth $SrTiO_3$ substrate with single TiO_2 termination[8]. Both developments, high-pressure RHEED and single-terminated substrates, contributed to the controlled and improved epitaxial growth of complex oxides and will be discussed in chapter 2.

Stoichiometric deposition is essential during epitaxial growth of multi-component complex oxides and is easily obtained in PLD. This is probably the most frequently mentioned reason to use PLD to grow these materials. However, the high deposition rates attained during the deposition pulse and the variable range of the kinetic energy of the deposited particles are, in fact, more unique for PLD and can be exploited to improve the thin film properties, like crystallinity and surface smoothness. Taking advantage of the growth kinetics at the high supersaturation reached during the deposition pulses, a new approach has been developed, called pulsed laser interval deposition[9], enabling 2-dimensional (2D) growth and, consequently, flat film surfaces. In addition, the pulsed deposition allows the measurement of the kinetic parameters that control the growth. This new deposition approach and growth kinetics measurements will be discussed in chapter 3.

Conductive ferromagnetic oxide $SrRuO_3$[10] has been grown on TiO_2 terminated $SrTiO_3$ substrates as a model system for initial heteroepitaxial growth studies. $SrRuO_3$ has been subject to many studies because of its unique structural, magnetic and electronic properties as well as its chemical stability, even at temperatures up to 1200 K. It is one of the best conducting metallic oxides and, therefore, an eminent candidate as an electrode material in all-oxide electronic devices. Epitaxial growth of $SrRuO_3$ requires a specific regime to avoid decomposition, namely deposition temperatures up to 700 °C and oxygen pressures in the range of 10-20 Pa, making high-pressure RHEED an excellent technique to study its growth behavior. Time-resolved measurements in combination with atomic force microscopy (AFM), presented in chapter 4, reveal an unexpected termination conversion accompanied by a transition from 2D growth to a steady state growth mode.

The electrical transport properties[11] of RE123 high-T_C superconducting thin films are affected by the microstructure[12], e.g., crystallinity, defect structure and surface morphology. Pinning of vortices[13] by defects is believed to be responsible for the higher critical current density found in thin films compared to bulk samples[14.] The origin and nature of these defects, e.g., point defects, line defects and planar defects, have been discussed by many groups[15,16,17]. Most of the defects are growth-induced and, therefore, a direct result of the thin film growth mechanisms. Understanding of these mechanisms is crucial for the improvement and reproducibility of the thin film properties. A literature overview of initial growth studies, focused on the atomic layer stacking sequence at the substrate-film interface and the terminating atomic layer of RE123 is given in chapter 5.

Next, high-pressure RHEED, AFM and high-resolution electron microscopy (HREM) measurements are applied to study the growth of RE123 on single-terminated $SrTiO_3$ substrates. Roughening of the film surface is observed by RHEED and AFM during the initial growth, i.e., during growth of the first unit cell layer, whereas anti-phase boundaries (APB's) are the main crystalline defects at the substrate-film interface observed by HREM. Both roughening and APB formation are caused by the coalescence of growing islands with different atomic layer stacking sequences at the substrate-film interface. Control of the stacking sequence at the substrate-film interface is used to prevent APB's and surface roughening during the initial growth. The initial growth study and control will be discussed in chapter 5 too.

Efforts have been made to grow Y123 by the sub-unit cell layer epitaxy method and will be discussed in chapter 6. Sub-unit cell layers, i.e., $BaCuO_x$ and $YCuO_x$, are sequentially deposited at reduced temperature using the pulsed laser interval deposition approach mentioned above.

References

1 A variety of cuprate superconducting oxides have been synthesized after the discovery in 1986 of superconductivity at 30 K in the La-Ba-Cu-O system: J.G. Bednorz and K.A. Müller, *Z. Phys. B* **64**, 189 (1986). In 1987, the superconducting transition temperature has been raised to 92 K in $YBa_2Cu_3O_{7-\delta}$: M.K. Wu, J.R. Ashburn, C.J. Torng, P.H. Hor, R.L. Meng, L. Gao, Z.J. Huang, Y.Q. Wang and C.W. Chu, *Phys. Rev. Lett.* **58**, 908 (1987)

2 I. Bozovic and J.N. Eckstein, *Appl. Surf. Sci.* **113/114**, 189 (1997)

3 B. Roas, L. Schultz and G. Endres, *Appl. Phys. Lett.* **53**, 1557 (1988)

4 D.H.A. Blank, D.J. Adelerhof, J. Flokstra and H. Rogalla, *Physica C* **162**, 125 (1989)

5 D.H.A. Blank, *High Tc thin films prepared by laser ablation*, PhD thesis ISBN 90-9004058-7, University of Twente

6 R.H. Hammond and R. Bormann, *Physica C* **162-164**, 703 (1989)

7 A.J.H.M. Rijnders, G.Koster, D.H.A. Blank and H. Rogalla, *Appl. Phys. Lett.* **70**, 1888 (1997)

8 G. Koster, B.L. Kropman, G.J.H.M. Rijnders, D.H.A. Blank and H. Rogalla, *Appl. Phys. Lett.* **73**, 2920 (1998)

9 G. Koster, G. J. H. M. Rijnders, D. H. A. Blank, and H. Rogalla, *Appl. Phys. Lett.* **74**, 3729 (1999)

10 J.J. Randall and R. Ward, *J. Am. Chem. Soc.* **81**, 2629 (1959)

11 P. Chaudhari, R.H. Koch, R.B. Laibowitz, T.R. McGuire and R.J. Gambino, *Phys. Rev. Lett.* **58**, 2684 (1987)

12 R. Ramesh, D.M. Hwang, T. Venkatesan, T.S. Ravi, L. Nazar, I. Inam, X.D. Wu, B. Dutta, G. Thomas, A.F. Marshall and T.H. Geballe, *Science* **247**, 57 (1990)

13 T.L. Hylton and M.R. Beasley, *Phys. Rev. B* **41**, 11669 (1990)

14 L. Civale, A.D. Marwick, T.K. Worthington, M.A. Kirk, J.R. Thompson, L. Krusin-Elbaum, Y. Sun, J.R. Clem and F. Holtzberg, *Phys. Rev. Lett.* **67**, 648 (1991)

15 B. Dam, J.M. Huijbrechtse, F.C. Klaassen, R.C.F. van der Geest, G. Doornbos, J.H. Rector, A.M. Testa, S. Freisem, J.C. Martinez, B. Stäuble-Pümpin and R. Griessen, *Nature* **399**, 439 (1999)

16 M. McElfresh, T.G. Miller, D.M. Schaefer, R. Reifenberger, R.E. Muenchausen, M. Hawley, S.R. Foltyn and X.D. Wu, *J. Appl. Phys.* **71**, 5099 (1992)

17 T. Haage, J. Zegenhagen, J.Q. Li, H.-U. Habermeier, M. Cardona, CH. Joos, R. Warthman, A. Forkl and H. Kronmüller, *Phys. Rev. B.* **56**, 8404 (1997)

Chapter 2

Experimental:
Technology and analysis

2.1 Introduction

The fabrication of complex oxide epitaxial thin films involves deposition as well as subsequent growth. Here, growth is the incorporation of the adsorbed atoms (adatoms) at the film surface. Many surface processes during deposition and growth determine the thin film properties such as crystallinity and surface morphology and are, therefore, subject to many studies. Reflection high-energy electron diffraction (RHEED) is most often used to study the mechanisms and film surface processes during growth, whereas scanning probe microscopy (SPM) is usually employed to study the surface morphology after deposition.

Mostly physical vapor deposition (PVD) techniques are used for the fabrication of oxide thin films. Among these are sputter deposition, molecular beam epitaxy (MBE) and pulsed laser deposition (PLD). The latter technique is the most extraordinary because of its unique features: a high pulse deposition rate and the controllable kinetic energy of the deposited particles. With the introduction of high-pressure RHEED[1], growth rate control on an atomic level as well as *in situ* growth studies at the typical oxygen deposition pressures during PLD of complex oxides became possible. In this chapter, a PLD system equipped with high-pressure RHEED will be described, including its unique features.

In epitaxial growth of complex oxides, the surface morphology and the terminating atomic layer of the substrate play an important role. In this thesis, the thin film materials of interest are the ferromagnetic $SrRuO_3$ and high-T_C superconducting $REBa_2Cu_3O_{7-\delta}$ (RE123; RE = Y or rare earth element), both belonging to the class of perovskite oxides with the general crystal structure ABO_3. $SrTiO_3$ is used as the substrate material because of its chemical stability at high temperatures and nearly perfect lattice match with the materials of interest. In this chapter, the control of the terminating atomic layer of $SrTiO_3$ substrates with high-crystalline surface quality using a chemical and thermal treatment will be discussed.

2.2 Pulsed laser deposition

Pulsed laser deposition refers to a thin film deposition technique using laser ablation from a target acting as the particle source. These particles are deposited on a substrate, placed opposite to the target, resulting in thin film growth. The most often mentioned reason to use PLD is the easy stoichiometric transfer of material from target to substrate at high ambient pressure. PLD is, therefore, frequently used for the fabrication of complex oxide thin films, because a high oxygen pressure is favorable during their growth.

PLD became widespread just after the discovery of the high-T_C superconductor $YBa_2Cu_3O_{7-\delta}$ (Y123)[2]. Here, stoichiometric transfer at high oxygen pressure is essential and first attempts at thin film fabrication of this complex oxide with PLD were very successful, leading to increased interest in PLD.

2.2.1 Basic principles

In PLD, a pulsed, highly energetic laser beam[I] is focused on a target, resulting in ablation of material. At the early stage of the laser pulse a dense layer of vapor is formed in front of the target. Energy absorption during the remainder of the laser pulse causes both pressure and temperature of this vapor to increase, resulting in partial ionization. This layer expands from the target surface due to the high pressure and forms the so-called “plasma plume”. During this expansion, internal thermal and ionization energies are converted into kinetic energy (several hundred eV) of the ablated particles. Attenuation of the kinetic energy occurs during expansion into low-pressure background gas due to multiple collisions. Typically, a background pressure of 1 to 50 Pa is used for deposition of complex oxides. At these pressures, thermalization occurs at a penetration length comparable to the target-to-substrate distance. Several models, like the “drag force” and the “shock wave” model[3,4], have been proposed which describe this attenuation in low and high background pressure, respectively. Using an adiabatic thermalization model,[5] a characteristic length scale is determined which defines

---

[I] Usually an excimer laser or high order Nd:YAG laser is used. Both produce high-intense laser pulses in the UV range at frequencies up to several hundreds Hz.

the “plasma range”. Plasma particles thermalize at distances larger than this characteristic length.

Ambient gas parameters, i.e., mass and pressure, determine the interaction with the ablated particles and, subsequently, the kinetic energy of the particles arriving at the substrate. As a consequence, this kinetic energy can be varied from high initial energy in vacuum to low energies resulting from thermalization at sufficiently large ambient pressures. This wide range is a unique feature of PLD and can be used to modify thin film growth. Here, the diffusivity[6,7] and both absorption and desorption probability[8] of the energetic particles at the film surface are the controllable parameters[II].

Another unique feature of PLD is the high deposition rate. In PLD of oxides, for instance RE123, typical deposition rates range from 10^{-2} to 10^{-1} nm/pulse with deposition pulse duration[III] in the order of several μs to ~500 μs[9,10]. As a result, the deposition rate can be as high as 10^{2}-10^{5} nm/sec[11,12]. This value is orders of magnitude higher than other PVD techniques like sputter deposition and MBE, which have typical deposition rates of 10^{-2}-10^{-1} nm/sec. The short duration of the intense deposition pulse has implications for the nucleation and growth processes. This is illustrated by comparing the pulse duration with the mean diffusion time t_D of deposited atoms, which is given by:

$$t_D = \nu^{-1} exp\left(\frac{E_A}{k_B T}\right) \tag{2.1}$$

with ν the attempt frequency for atomistic processes, E_A the activation energy for diffusion, k_B Boltzmann’s constant and T the temperature. Here, the mean diffusion time t_D is of interest because it sets the time scale for the atomistic processes, including collision and nucleation. For complex oxides E_A ranges from a few tenths of an eV to more than 2 eV and typical growth temperatures range from 800 to more then 1100 K. Using eq. (2.1) the mean diffusion time can be estimated. For a wide range of deposition conditions t_D exceeds the deposition pulse duration. As a consequence, the deposition can be regarded as instantaneous for every pulse. In PLD, this instantaneous deposition is followed by a relatively long time interval where no deposition takes place. During this time interval, which is determined by the pulse repetition rate, the adatoms rearrange on the surface by migration and subsequent incorporation through nucleation and growth. This rearrangement can be considered as an anneal process. Because of the instantaneous deposition, the

---

[II] Bombardment with high-energetic particles of the film surface during growth may lead to a defective crystal structure of the film and should be avoided.

[III] Note that the deposition pulse duration differs from the laser pulse duration.

two basic processes, i.e., random deposition and growth through rearrangement are separated in time, which is again unique for PLD[IV].

Parameters, which control the instantaneous deposition rate, are the laser energy density at the target, pulse energy, distance between target and substrate and the ambient gas properties, i.e., pressure and mass. The average growth rate is determined by the pulse repetition rate and can be varied independently from the instantaneous deposition rate.

The extremely high deposition rate leads to a very high degree of supersaturation $\Delta\mu$ [13]:

$$\Delta\mu = k_B T \ln \frac{R}{R_0} \tag{2.2}$$

where k_B is Boltzmann's constant, R the actual deposition rate and R_0 its equilibrium value at temperature T. The high degree of supersaturation $\Delta\mu$ causes two-dimensional (2D) nucleation of a high density of extremely small[V] clusters. Because of the instantaneous deposition at typical PLD conditions, the nucleation takes place after the deposition pulse and can be considered as post-nucleation[14,15]. Sub-critical clusters are unstable in the time interval between the deposition pulses and dissociate into mobile atoms. These nucleate into new clusters or cause stable clusters to grow. The latter process is similar to Oswald ripening where larger islands grow at the expense of small islands or clusters.

The separated random deposition and subsequent growth is, furthermore, advantageous for the study of growth kinetics, as will be shown in chapter 3.

2.2.2 PLD set-up

Figure 2.1 shows the schematic drawing of the PLD system equipped with high-pressure RHEED. In the experiments described here, a KrF excimer laser (Lambda Physic Compex 205, wavelength $\lambda = 248$ nm) with maximum pulse repetition rate of 50 Hz is used. The maximum pulse energy is 650 mJ with pulse duration ~25 nsec. A mask is used to select the homogeneous part of the laser beam, resulting in a spatial energy variation of ~5%. The mask is projected at an inclination of 45° on the target by means of a focusing lens (focal length ~450 mm). The energy density on the target is controlled by adjustment of both mask size and demagnification.

[IV] In most deposition techniques the deposition flux is continuous. As a result, deposition and surface relaxation occurs simultaneously.

[V] In case of PLD, the clusters can be as small as one atom to a few molecular blocks of the complex oxides.

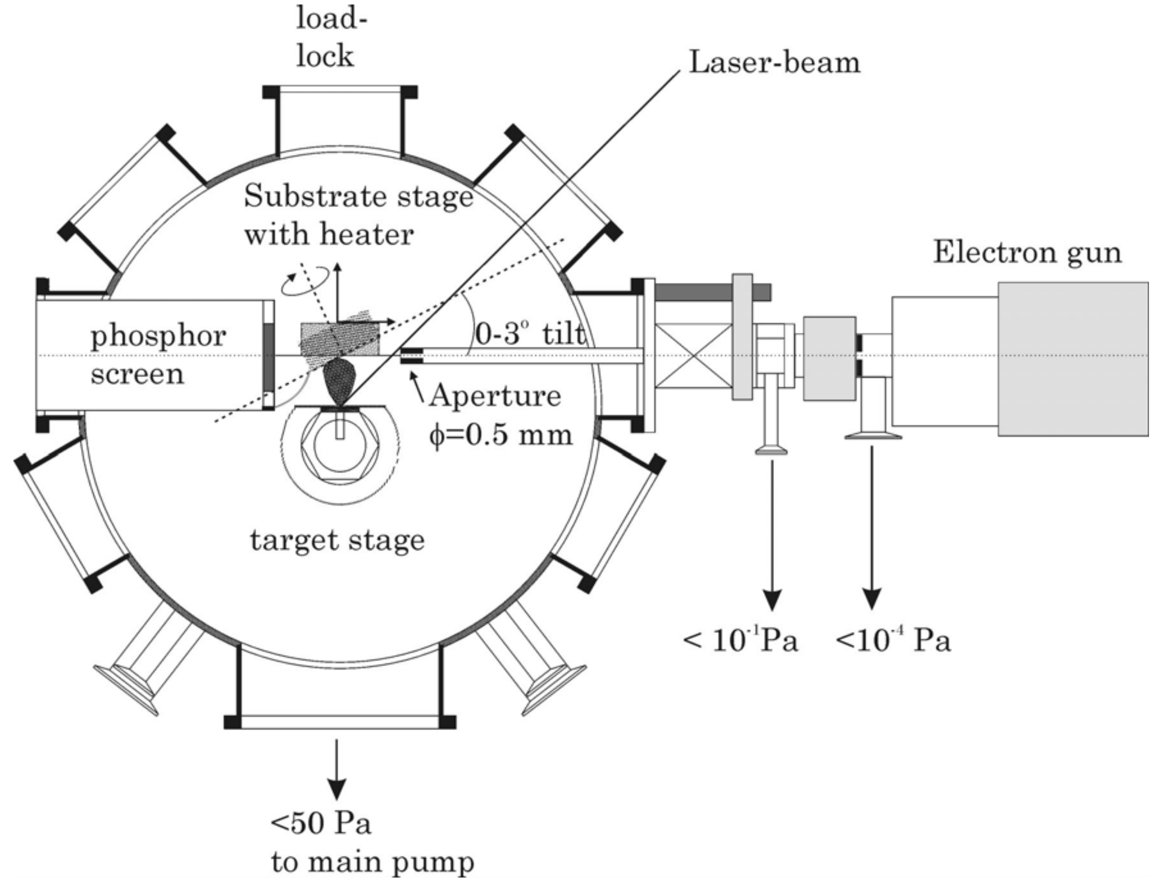

Figure 2.1: A schematic view of the deposition chamber, including the electron source assembly.

The multi-target holder and substrate holder including heater are mounted on a computer controlled XYZ-rotation stage and can be inserted via a load-lock system without breaking the vacuum (base pressure ~10^{-5} Pa). The PID controlled temperature of the heater (resistively heated using thermo-coax wires) is measured using a K-type thermocouple.

Oxygen gas (purity >4.5) as well as inert gasses (He, Ne, Ar, purity >4.0) can be used as deposition gas. The deposition pressure (10^{-1}-10^{2} Pa) is controlled by the effective pump speed and the total gas mass flow (Brooks Instruments, 0-40 ml/min @ 10^{5} Pa). The effective pump speed is adjusted through a variable restriction between the deposition chamber and turbo-molecular drag pump.

The system is fully computer controlled including selection of the targets allowing for automated multi-layer deposition.

2.2.3 Experimental conditions

Stoichiometric transfer of particles from multi-component targets to substrate is essential in PLD of complex oxides. This transfer is affected by the target

Table 1.1: Typical PLD conditions used in the experiments.

	Target type	PO_2 (Pa)	T (ºC)	Energy density (J/cm^2)	Deposition rate (Å/pulse)
SrO	single crystal	4	600-850	2.0	0.2
$SrTiO_3$	single crystal	4-20	600-850	1.3	0.2-0.3
$SrRuO_3$	sintered pellet	14	500-700	2.5	0.2
Y123/Dy123	sintered pellet	14	780	1.3	1
Dy122	sintered pellet	14	780	1.3-8	1
$BaCuO_x$	sintered pellet	10-30	600	1.3	0.4
$YCuO_x$	sintered pellet	10-30	600	1.3	0.07

properties, such as density and homogeneity. The density of target materials should be as high as possible to avoid removal of big clusters from the target during ablation. Deposition of these clusters negatively influences the epitaxial growth and should be avoided. Because of the high density and homogeneous distribution of components, single crystals are preferred as target materials. For many materials, however, single crystals are not easily obtained. In these cases, sintered pellets with the highest possible density are used.

In our experiments we used single crystals of SrO[VI] and $SrTiO_3$[VI], whereas sintered pellets were used for Y123[VII], Dy123[VII], $BaCuO_x$[VII] and $SrRuO_3$[VIII]. $DyBa_2Cu_2O_x$ and $DyCuO_x$ targets were prepared by us using solid-state reactions. Sources for dysprosium and copper were grade pure oxides (Dy_2O_3, 99.99% and CuO, 99.999%), while for barium grade pure carbonate ($BaCO_3$, 99.999%) was used. A mixture of powders with the nominal cationic composition was ball milled with Al_2O_3 balls for 8 h to reach a high degree of homogeneity, followed by a calcination treatment in a Pt crucible at 575 ºC in air for 12 h and, subsequently, at 850 ºC for 15h. The resulting mixture was isostatically pressed at 100 MPa and sintered at 950 ºC for 24 h in flowing oxygen. The resulting targets were then annealed for 12 h at 450 ºC in an O_2 flow.

The most important PLD conditions used in the experiments described in this thesis are given in table 1.1. Both oxygen deposition pressure and growth temperature allows for growth in a stable regime, where no decomposition of the films is observed. The laser energy density at the target has been optimized for stoichiometric transfer and plasma characteristics, i.e., shape, size and impingement energy of the plasma particles at given deposition pressure.

[VI] ESCETE, Enschede, the Netherlands

[VII] Hitec materials Germany, density > 95%

[VIII] Lucent technology, Bell laboratories.

2.3 High-pressure reflection high-energy electron diffraction (RHEED)

Reflection high-energy electron diffraction (RHEED) has become an important tool in surface science because of its high surface sensitivity. It utilizes diffraction of electrons by surface atoms and provides information about the periodic arrangement of the surface atoms. Because of the compatibility with (ultra) high vacuum deposition techniques, it is often used for the investigation of the surface morphology during thin film growth. It requires minimal hardware and thus is a relative low-cost analysis technique.

2.3.1 Geometry and basic principles of RHEED

A schematic drawing of a typical RHEED geometry is sketched in figure 2.2. The incident electron beam (e-beam) strikes the sample surface at a grazing angle θ_i. The electrons are mono-energetic with a typical energy of E~10-50 keV. The corresponding amplitude of the wave vector $\boldsymbol{k_0}$ for these high-energy electrons is given by:

$$|\boldsymbol{k_0}| = \frac{1}{\hbar}\sqrt{2m_0E + \frac{E^2}{c^2}} \tag{2.3}$$

where m_0 is the rest mass of the electrons. Without relativistic correction[IX] the electron wavelength λ can be estimated by:

$$\lambda(\mathring{A}) = \sqrt{\frac{150}{E}} \tag{2.4}$$

with E given in eV. At the typical energies used in RHEED, the electron wavelength λ is ~0.05-0.1 Å, which is an order of magnitude smaller than the thickness of an atomic layer. The angle of incidence is typically set to a few degrees (0.1-5°). At these grazing angles the penetration depth is only a few atomic layers, which makes RHEED a surface sensitive diffraction technique; the electrons are easily scattered by surface steps and terraces. The coherence length[16], which is the maximum distance between reflected electrons that are able to interfere, is determined by the beam convergence and the energy spread of the electrons. This coherence length is typically of the order of several hundreds nm.

[IX] The relativistic mass correction should be a few % for the energies of interest.

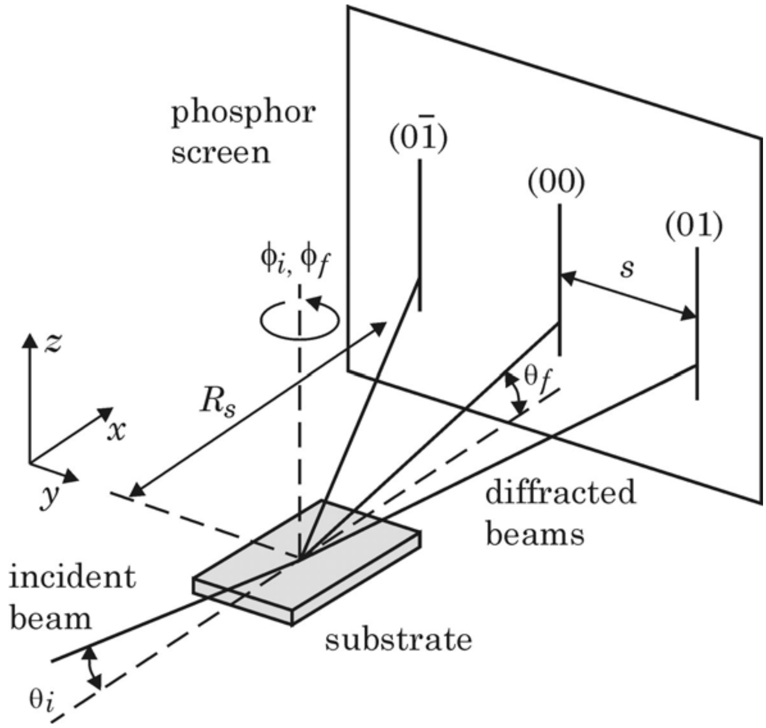

Figure 2.2: Schematic view of the RHEED geometry. θ_i (θ_f) *and* ϕ_i (ϕ_f) *are the incident and azimuthal angles of the incident (diffracted) beam.* R_S *is the distance between substrate and phosphor screen and S the distance between the diffraction spots or streaks.*

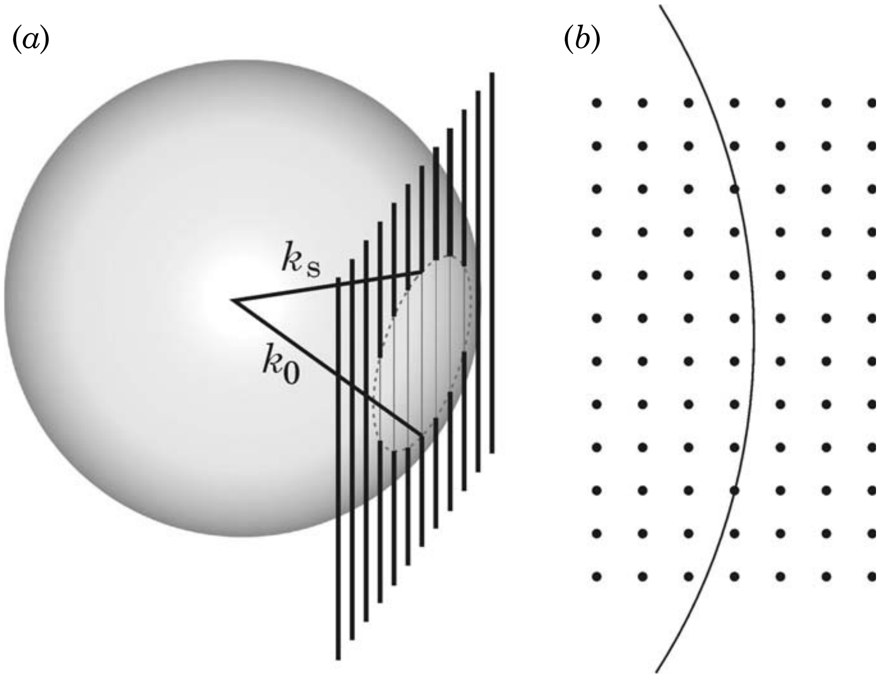

Figure 2.3: Ewald sphere construction in three dimensions (a) and a section of the horizontal z=0 plane (b).

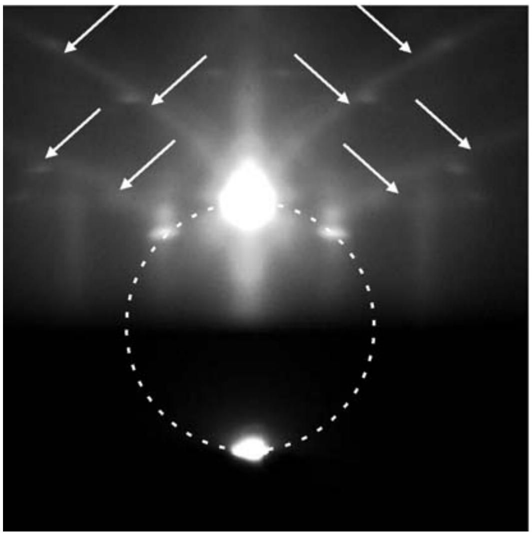

Figure 2.4: Typical RHEED pattern as recorded from a perfect $SrTiO_3$ surface.

The electron gun (e-gun) and phosphor screen (acting as detector) are located far from the sample to avoid interference with the deposition process. In this geometry, electrons are scattered from the crystal surface resulting in a characteristic diffraction pattern on the phosphor screen. This pattern is instantaneously displayed and can be used to define the crystallographic surface structure of, for instance, a growing thin film.

The kinematical[X] scattering theory is used to describe weakly interacting diffraction techniques, like x-ray or neutron diffraction. RHEED, however, involves strong interaction[17] of the electrons with the periodic potential of the crystal surface and can, therefore, not be described quantitatively by the kinematic approach. Nevertheless, the kinematic approach is used for both physical understanding and qualitative description of RHEED.

RHEED diffraction spots are produced when the momentum of the incident beam and that of the diffracted beam differ by a reciprocal lattice vector $\boldsymbol{G}$:

$$\boldsymbol{k_S} - \boldsymbol{k_0} = \boldsymbol{G} \tag{2.5}$$

where $\boldsymbol{k_S}$ and $\boldsymbol{k_0}$ are the wave vectors of the diffracted and incident beams.

A useful geometrical representation of the conditions for diffraction in elastic scattering, i.e., $|\boldsymbol{k_S}| = |\boldsymbol{k_0}|$, is provided by the Ewald sphere construction, depicted in figure 2.3. Here, the reciprocal lattice of a 2-dimensional surface is a lattice of infinitely thin rods, perpendicular to the surface. The tip of the incident wave vector is attached to a reciprocal lattice rod. The Ewald sphere is defined by the sphere around the origin of $\boldsymbol{k_0}$ with radius $|\boldsymbol{k_0}|$ (equals $2\pi/\lambda$ for elastic scattering).

[X] Only single elastic scattering is assumed.

The condition for diffraction is satisfied for all $\boldsymbol{k_S}$ connecting the origin of $\boldsymbol{k_0}$ and a reciprocal lattice rod. For perfect[XI] surfaces, this results in diffraction spots lying on concentric circles, called Laue circles. Figure 2.4 shows a diffraction pattern of a perfect $SrTiO_3$ surface[18]. It exhibits sharp diffraction spots lying on the 0th order Laue circle, i.e., intersections of the $(0k)$ rods with the Ewald sphere. Due to the substrate size and RHEED geometry, i.e., e-beam diameter and grazing angle, part of the e-beam is not blocked by the substrate and is visible in the diffraction pattern. The specular reflected beam is the diffraction spot "lying" on the same rod as the incident beam. It is, therefore, never forbidden, unlike other spots.

Due to the high electron energy, used in RHEED, the Ewald sphere is very large compared to the reciprocal lattice spacing of oxide crystals. As a result, only a few reciprocal lattice rods are intersected at the small grazing incident angle. Essentially, a one-dimensional map of the reciprocal space is obtained, see figure 2.3 (b). Other areas of the reciprocal space are mapped by rotation of the sample about the incident angle or, alternatively, the azimuthal angle ϕ_i.

As mentioned previously, RHEED is a strong interaction diffraction technique and dynamical scattering has to be taken into account. As a result non-linear effects like multiple scattering occur leading to anomalies in the RHEED intensity. One of these anomalies is a phenomenon often observed in RHEED: Kikuchi lines. They originate from diffraction of diffuse scattered electrons and appear as curved lines on the phosphor screen, indicated by arrows in figure 2.4. The intensity of a diffraction spot or streak is affected at intersections with Kikuchi lines, since diffusive scattered electrons contribute to the diffracted intensity. Intensity measurements during growth near such intersections should be avoided.

Kikuchi lines move as if they were rigidly fixed to the crystal and are, therefore, often used to determine the crystal orientation and align the e-beam. The occurrence of clear and sharp Kikuchi lines is an indication of a flat and crystalline surface.

[XI] Here, perfect refers to a clean and atomically flat, single-domain crystalline surface.

2.3.2 Utility of RHEED: surface properties

2.3.2.1 Determination of lattice parameter

From the spot positions in a RHEED pattern of a perfect low index plane one can determine the in-plane lattice constants. Using polar coordinates, the rectilinear projections of the scattering wave vector $\boldsymbol{k_S}$ can be written as:

$$k_{sx} = |\boldsymbol{k_0}|\left(cos\,\theta_f\, cos\,\phi_f - cos\,\theta_i\, cos\,\phi_i\right) \tag{2.6a}$$

$$k_{sy} = |\boldsymbol{k_0}|\left(cos\,\theta_f\, sin\,\phi_f - cos\,\theta_i\, sin\,\phi_i\right) \tag{2.6b}$$

$$k_{sz} = |\boldsymbol{k_0}|\left(sin\,\theta_f + sin\,\theta_i\right) \approx |\boldsymbol{k_0}|(\theta_f - \theta_i) \text{ (for small angles)} \tag{2.6c}$$

with k_{sx} and k_{sy} in the low index plane, k_{sz} perpendicular to the low index plane, θ_i and ϕ_i the incident and azimuthal angles of the incoming beam, and θ_f and ϕ_f the incident and azimuthal angles of the final (diffracted) beam, (see figure 2.2). For the incident beam directed along a low index direction (ϕ_i=0), the lattice parameters d_x (parallel to the incident beam) and d_y (perpendicular to the incident beam) can be derived from the angles of Bragg reflections using eq.'s (2.6) by:

$$\frac{n}{d_x} = \frac{1}{\lambda}\left(cos\,\theta_f - cos\,\theta_i\right) \tag{2.7a}$$

where ϕ_f=0, i.e., for intersections of the Ewald sphere with (h0) rods, and:

$$\frac{n}{d_y} = \frac{1}{\lambda}\left(cos\,\theta_f\, sin\,\phi_f\right) \tag{2.7b}$$

where n is the order of the reflection. The angles can be determined directly by dividing the relative on-screen distances by the sample-to-screen distance R_S, assuming only small angles.

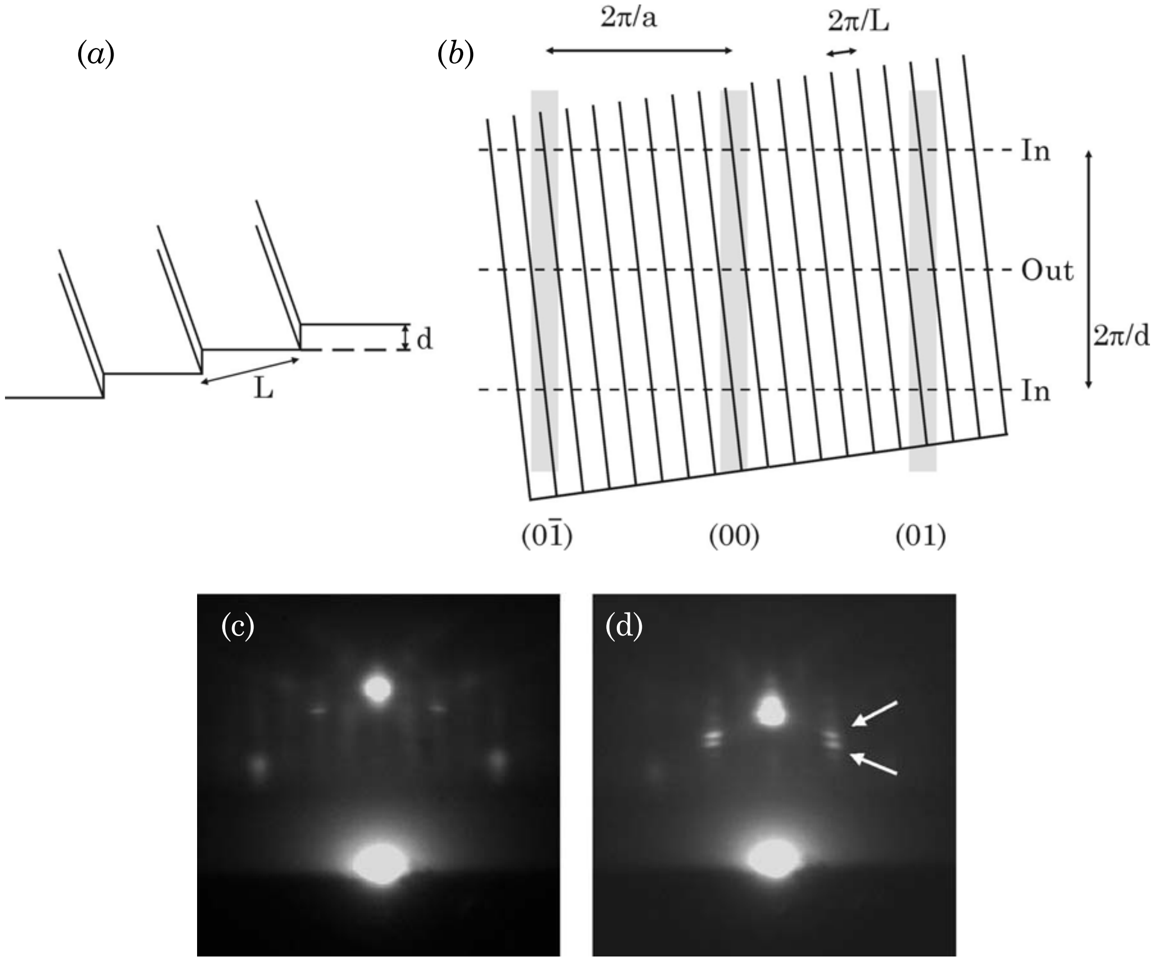

Figure 2.5: Real space (a) and reciprocal space (b) of a vicinal surface with a *the in-plane lattice parameter,* d *the step height and L the terrace width. RHEED patterns as recorded from a vicinal* $SrTiO_3$ *surface with incident beam perpendicular to the step ledges: in-phase condition (c) and out-of-phase condition (d).*

2.3.2.2 Determination of vicinal angle

RHEED can be used to measure the average terrace width on vicinal surfaces. A vicinal surface is created by a slight miscut of the substrate surface along an orientation close to a high symmetry one. It is made up of low index terraces, e.g., (001) or (101), separated by unit cell steps in perovskite substrates. The terrace width is determined by the miscut angle (in the remainder of the text referred to as vicinal angle β), defined as the angle between the actual surface plane and the high symmetry plane. Here, the diffracted intensity is the product of the diffraction due to the in-plane lattice constant on the terraces and the diffraction due to the additional periodicity of the step-terrace structure, see figure 2.5. At the out-of-phase condition, the diffracted intensity is most sensitive for the step-terrace structure on the surface and splitting of the RHEED spot is observed. From the splitting angle $\Delta\theta_f$ the vicinal angle β can be estimated using[19]:

$$\Delta\theta_f = \left(\frac{2\pi}{kd}\right)\frac{\beta \cos\phi_{p,i}}{\beta \cos\phi_{p,i} + \langle\theta_f\rangle} \tag{2.8}$$

where $\beta \cos\phi_{p,i}$ is the projected vicinal angle along the incident beam direction and $\langle\theta_f\rangle$ the average diffraction angle. Figure 2.5 (c) and 2.5 (d) show diffraction patterns[XII] of a vicinal[XIII] $SrTiO_3$ surface at both in-phase and out-of-phase condition, respectively. Here, a value of ~0.25° is determined for the vicinal angle β.

2.3.2.3 Non-perfect surfaces

As shown, intersection of the Ewald sphere with the reciprocal lattice rods of a perfect crystalline surface produces sharp diffraction spots lying on Laue circles. Deviations from such a perfect surface, such as additional roughness and crystal defects, cause broadening of spots or a change in the position of the spots. Figure 2.6 shows RHEED patterns taken from such non-perfect surfaces. In figure 2.6 (a), besides spots lying on the 0th Laue circle, two additional spots are observed marked by the arrows. Here, the RHEED pattern is the sum of diffraction from two different domains of a $SrTiO_3$ substrate surface. Rotation around the azimuthal axis reveals that the two domains have different in-plane orientation, see figure 2.6 (b). The RHEED pattern can be described by adding the reciprocal lattices from both domains in the Ewald sphere construction.

A roughened surface, for instance a surface consisting of a random distribution of terraces and steps, is accompanied by broadening of the lattice rods. As a result, streaks occur due to intersections with the Ewald sphere. As an example a RHEED pattern is shown in figure 2.6 (c) taken after deposition of a 4 unit cell thick Y123 layer, see chapter 5 for experimental details.

Penetration of the e-beam through protrusions, for instance small three-dimensional (3D) islands or small asperities, results in transmission spots. The reciprocal lattice rods are replaced by the bulk reciprocal lattice and, consequently, streaks are replaced with spots. A RHEED pattern of such rough surface is given

---

[XII] Here, the incident beam is directed perpendicular to the step ledges. In the parallel direction no splitting is observed due to the one-dimensional mapping of the reciprocal space in RHEED, section 2.3.1.

[XIII] The step-terrace surface can still be considered as perfect, consisting of atomically flat and crystalline terraces and unit cell height step ledges.

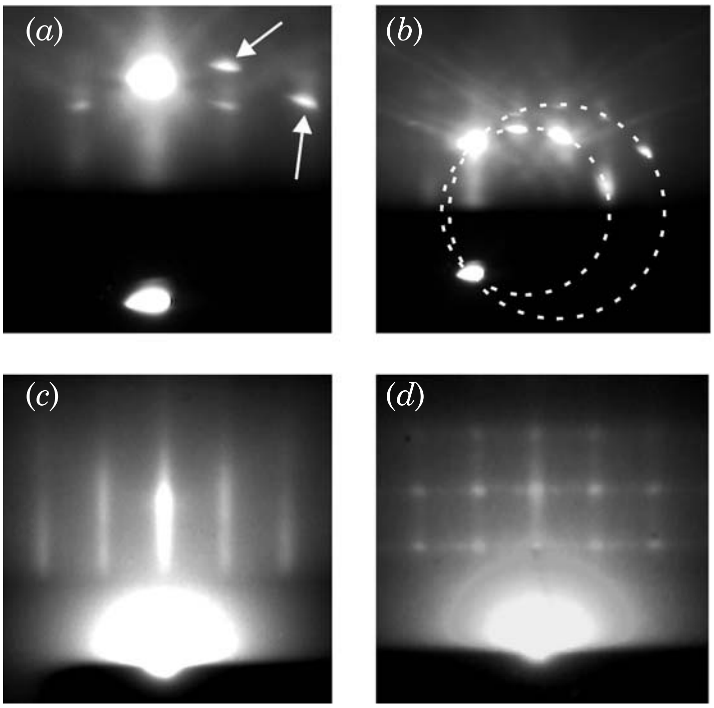

Figure 2.6: RHEED patterns recorded from non-perfect crystalline surfaces: $SrTiO_3$ surface with two-domain structure, azimuthal angle $\phi_i = 0$ (a) and off-azimuthal angle (b), 4 unit cell thick Y123 layer (c) and several unit cell layers of Y123 deposited using non-optimized conditions (d).

in figure 2.6 (d), after non-optimized deposition of several unit cell layers of Y123 on $SrTiO_3$.

2.3.3 Utility of RHEED: monitoring thin film growth

In the early days of RHEED, the surface sensitivity was exploited mainly for the study of cleaved crystals and surface reconstruction. Now, the main applications are thin film growth monitoring and the study of growth kinetics. The existence of intensity oscillations[20] corresponding to the 2-dimensional (2D) growth of atomic or molecular layers is probably the most important reason to use RHEED. Here, the surface is periodically roughened and smoothed during the 2D nucleation and growth, resulting in a periodically varying density of surface steps. Electrons are easily scattered out of the specular beam by the step edges since the layer thickness is much larger than the wavelength of the electrons. As a result, periodic intensity variations are expected during 2D growth, which can be used to determine the growth rate. A detailed description of RHEED intensity variations during 2D growth of complex oxides in PLD will be given in chapter 3.

2.3.4 High-pressure RHEED

2.3.4.1 Electron scattering

The pressure in a RHEED set-up has to be sufficiently low to avoid electron scattering by the ambient gas. Attenuation of the electron beam (e-beam) intensity is to be expected at high ambient pressure due to elastic and inelastic electron scattering[21]. Furthermore, a low pressure is required near the filament[XIV] of the e-gun. With the introduction of the differentially pumped e-gun[XV], the maximum operating pressure was raised to ~1 Pa[22]. To increase the operating pressure in RHEED to the high deposition pressures used in PLD of oxides, both mentioned requirements have to be fulfilled: a low pressure in the e-gun should be maintained and the attenuation of the e-beam intensity has to be minimized. The latter can be expressed as[23]:

$$\frac{I}{I_0} = exp\left(-\frac{l}{L_E}\right) \tag{2.9a}$$

where L_E is the mean free path of the electrons, l is the distance of the traveling path of the electrons and I_0 is the intensity of the beam for $l \ll L_E$, i.e., at sufficiently low pressure. The mean free path L_E is defined as:

$$L_E = \frac{1}{\sigma_T n} \tag{2.9b}$$

where σ_T is the total cross-section[XVI] for scattering and n is the molecular density given by:

$$n = \frac{P}{k_B T} \tag{2.9c}$$

with P the pressure, k_B Boltzman's constant and T the temperature.

[XIV] Usually a heated tungsten filament is used as the electron source. To avoid breakage or a short lifetime, the pressure needs to be well below 10^{-4} Pa.

[XV] Here, the pressure in the e-gun is still well below 10^{-4} Pa.

[XVI] σ_T includes cross-sections due to both elastic and inelastic scattering.

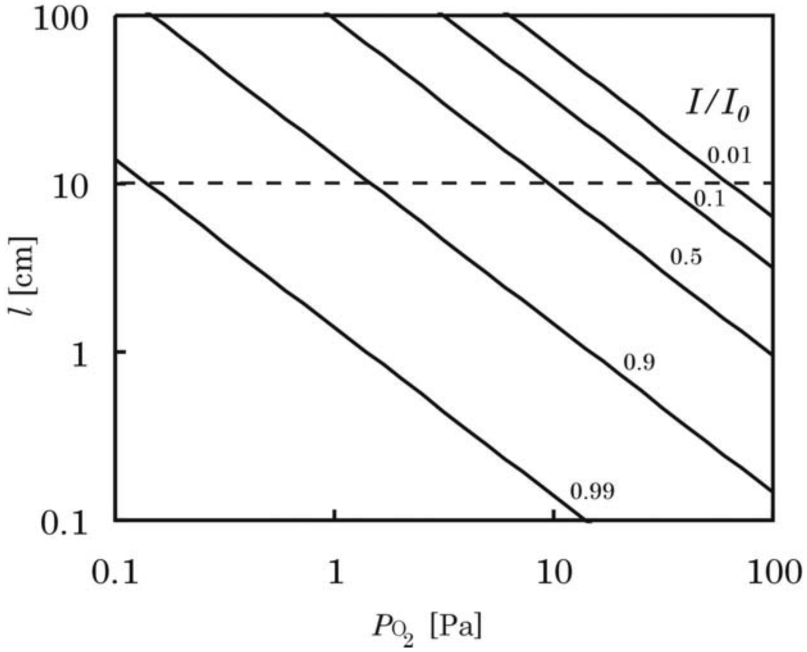

Figure 2.7: Attenuation I/I_0 of a 10 keV electron beam as function of the oxygen pressure Po_2 and travel distance l. The dashed line represents the traveling distance in our high-pressure RHEED set-up.

At the high electron energies used in RHEED the total cross-section σ_T decreases with increasing electron energy[21]. Unfortunately, no experimental data for electron scattering by O_2 at the high electron energies (>10 keV) used in RHEED have been reported. By extrapolating experimental data[21] a value for $\sigma_T \sim 3x10^{-21}$ m^2 at 10 keV is determined. Using this value, the attenuation I/I_0 can be estimated. Figure 2.7 shows the travel distance l for a 10 keV e-beam, calculated using eq. (2.9) as function of the oxygen pressure for several values of I/I_0. From this figure it becomes clear that the traveling distance has to be reduced to minimize electron scattering losses at the high oxygen pressures used in PLD.

2.3.4.2 High-pressure RHEED set-up

To satisfy the two requirements, i.e., low pressure in the e-gun and short traveling distance at high pressure, a two-stage, differentially pumped RHEED system has been developed[1]. A schematic view of this high-pressure RHEED system is depicted in figure 2.1. The e-gun (EK-2035-R, STAIB Instruments) has a minimum beam size of ~ 250 μm (FWHM), even at the working distance of 500 mm. It is mounted on a flange connected to a stainless steel extension tube with an inner diameter of 8 mm. A differential pumping unit is used to maintain a vacuum of better than 10^{-4} Pa in the e-gun. An aperture (diameter 0.5 mm) separates the tube from the deposition chamber. The pressure in the tube, which depends on the

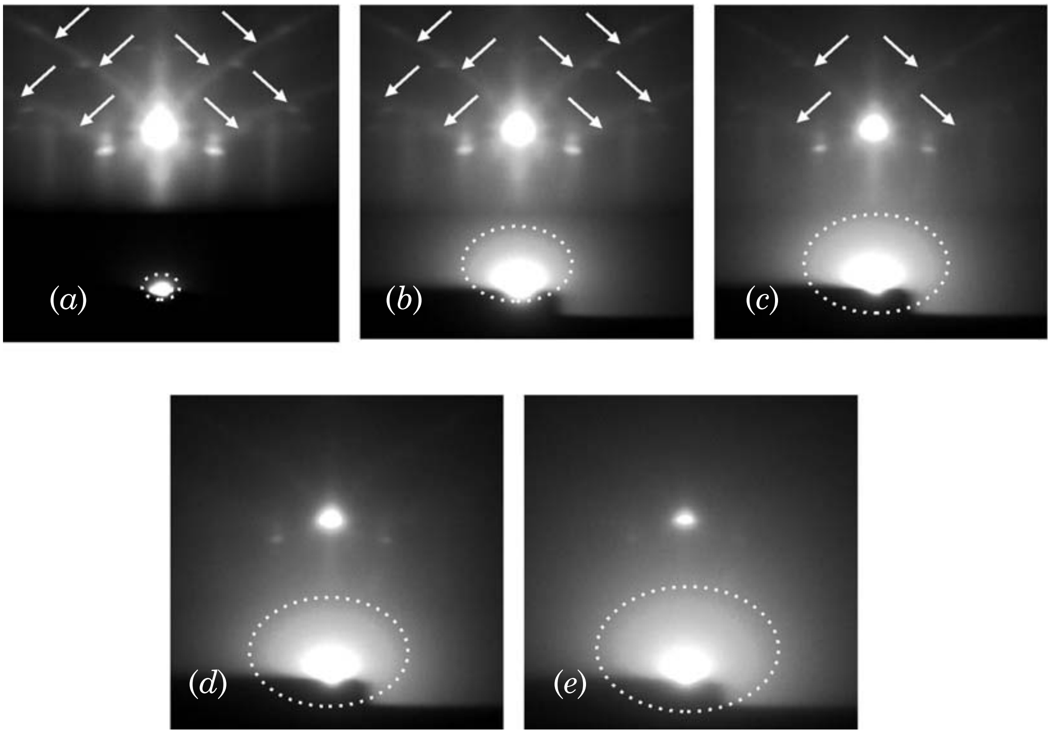

Figure 2.8: RHEED patterns from a perfect $SrTiO_3$ surface recorded at different oxygen pressure: 10^{-5} Pa (a), 10^{-1} Pa (b), 7 Pa (c), 15 Pa (d), 50 (Pa) (e). The arrows indicate the Kikuchi lines, the additional intensity due to the diffuse forward scattered incident electrons is indicated by the dotted lines.

pump speed and the size of the aperture, is kept below 10^{-1} Pa. Using this two-stage pumping system, the pressure in the deposition chamber can be increased up to 100 Pa, maintaining the low pressure in the electron source. The e-beam, which passes through the apertures inside the differential pumping unit and the tube, enters the deposition chamber near the substrate at a distance of 50 mm. The XY deflection capability of the electron source is used to direct the e-beam through the aperture at the end of the tube.

The fluorescent phosphor screen (diameter 50 mm) is mounted on a flange located near the substrate. The distance between the screen and substrate is 50 mm. The screen is shielded from the laser plasma to minimize deposition on the screen. The electron source, including the extension tube, is mounted on a XYZ-stage allowing adjustment of the distance between substrate and end of the tube.

Using the extension tube, the traveling distance in the high-pressure regime is reduced to 100 mm. Intensity losses due to electron scattering inside the extension tube are negligible since the pressure is kept well below 10^{-1} Pa. In the high-pressure regime, however, a significant decrease in the intensity (I/I_0~0.01) is

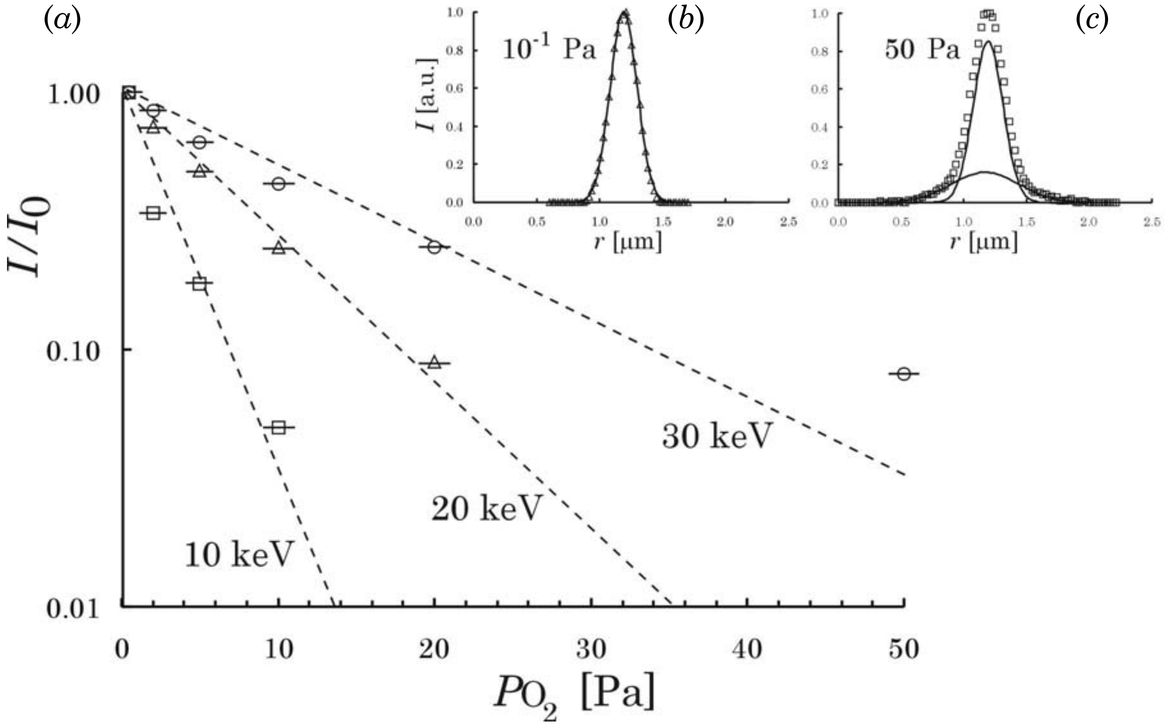

Figure 2.9: Attenuation I / I_0 versus oxygen pressure of the e-beam peak intensity at electron energy of 10 ( ), 20 (Δ) and 30 (O) keV, respectively (a). The insets show the e-beam (20 keV) intensity profile at 10^{-1} Pa (b) and 50 Pa (c); Δ and are measurement points, the solid lines Gaussian fits (travel length electrons l=10 cm).

expected at oxygen pressure P_{O_2}~100 Pa. However, compensation of the scattering losses is possible by adjusting the e-beam current[XVII].

At large working distances, the e-beam is deflected over several millimeters by small magnetic fields, like the earth magnetic field. Therefore, special care has been taken to shield the e-beam from magnetic fields using μ-metal. Furthermore, the substrate can be rotated in order to adjust the angle of incidence and azimuthal angle of the e-beam on the substrate. The diffraction pattern is monitored using a Peltier cooled CCD camera and acquisition software (K-Space Associates). The software allows for time-resolved spot intensity measurement. The minimum acquisition time for each data point is 33 ms.

Figure 2.8 (a)-(e) shows RHEED patterns recorded from perfect $SrTiO_3$ surfaces at several oxygen pressures from 10^{-5} to 50 Pa. As expected, the specular reflected intensity is a clear function of the ambient pressure. At pressures above 10 Pa, features like the sharp Kikuchi lines and a clear shadow edge disappear whereas the background intensity is increased due to the collection of the forward scattered electrons.

[XVII] The total e-beam current can be varied by adjustment of the filament current.

At an oxygen pressure of 50 Pa, the specular reflected spot is still clearly visible. Consequently, growth monitoring is feasible by measurement of the intensity variations of the specular reflected beam.

The attenuation[XVIII] of the e-beam intensity was measured in high $P\text{o}_2$ and electron travel distance l of 10 cm for different values of the electron energies, see figure 2.9. From the slopes, a value of 1.3×10^{-20}, 0.5×10^{-20} and 0.3×10^{-20} m^2 was determined for the total cross-section for scattering σ_T using eq. (2.9) for electron energies of 10, 20 and 30 keV, respectively. As expected, a smaller σ_T is observed at higher electron energy of 30 keV. Increase of the electron energy is, therefore, beneficial for the application of RHEED at high deposition pressure. The insets in figure 2.9 show the typical e-beam shapes for a non-attenuated e-beam at $P\text{o}_2 = 10^{-1}$ Pa (b) and an attenuated e-beam at $P\text{o}_2 = 50$ Pa (c). At low pressure the shape could be fitted by a single Gaussian curve with FWHM ~ 215 μm. At higher pressure, not only broadening of the e-beam (FWHM ~ 240 μm), but also the occurrence of a diffuse background is observed. Electrons are scattered in the forward direction[21] leading to a divergent e-beam[XIX]. The increase of the diffuse intensity of the primary e-beam at the high pressure in figure 2.8 (e) clearly indicates this effect.

2.4 Analysis tools

The crystalline structure and the surface morphology of epitaxially grown films are a direct product of the surface processes during growth. Suitable analysis of the structural properties is, therefore, essential for understanding these processes. Atomic force microscopy is used for analysis of the surface morphology, whereas X-ray diffractometry and high-resolution electron microscopy are used to study the crystalline structure. Experimental details of the analysis tools will be briefly addressed.

2.4.1 Atomic force microscopy

Scanning probe microscopy experiments were performed on a Nanoscope III (DI, Santa Barbara, CA), capable of contact and tapping mode imaging. For the

---

[XVIII] Here, we measured the peak intensity from the spot of the primary e-beam on the phosphor screen using the K-space acquisition equipment. Although non-linearity's are expected, relative measurements are adequate for this purpose. Here, I_0 is the peak intensity of the e-beam at $P\text{O}_2 < 10^{-2}$ Pa. No attenuation is observed at this pressure.

[XIX] The coherence length in RHEED is determined by the spread in both electron energy and beam convergence/divergence. As a result, a smaller coherence length is expected at higher ambient pressure.

contact mode, standard DI Si_3N_4 cantilevers were used with nominal force constants of $k = 0.18, 0.38, 0.58$ Nm^{-1}, whereas for tapping mode Si cantilevers with resonance frequency ranging from 310 to 400 kHz were utilized. Contact forces were kept as low as possible and are estimated to be <10 nN.

Lateral or frictional forces are measured simultaneously by the four-quadrant detector. No attempts have been made to quantify the friction force, since the exact lateral force constants of the cantilevers are unknown; the alignment of the laser on the cantilever changes and the humidity in the laboratory is not constant. In friction force micrographs high frictional forces are displayed as bright white colors and lower forces as dark colors (range of 0.1 V). Imaging took place immediately after a sample was taken out of the deposition chamber to avoid contamination that would affect the quality of the images.

2.4.2 X-ray diffraction

θ-2θ scans are performed on a single-crystal diffractometer (CAD4, Enraf Nonius Delft, the Netherlands) as well as on a thin film diffractometer (Siemens D5000) using a Cu-Kα source.

The instrumental broadening is estimated (from the substrate peaks) to be 0.2° for the CAD4 system. Furthermore, the θ-2θ scans performed on this system usually show additional peaks corresponding to spectral $\lambda/2$ and $\lambda/3$ lines transmitted by the strong $(00l)$ reflections of $SrTiO_3$. The orientation matrix of the substrate crystal was determined and scans were performed along the direction perpendicular to the substrate surface. Here, one has also the possibility to collect a full data set, which can be refined or to record a reciprocal space map around specific reflections. With the aid of a diode laser aimed at the surface acting as a small mirror and φ rotation around the (001) axis, the vicinal angle of the substrate can be accurately (± 0.01°) determined.

2.4.3 High-resolution electron microscopy

Electron microscopy was performed with a Jeol 4000EX, operated at 400kV and having a point resolution of 1.7Å. Image simulations were carried out using the Mac Tempas software. Cross-section samples for transmission electron microscopy (TEM) were cut parallel to the (010) or (100) plane of the $SrTiO_3$ substrate. After mechanically polishing the sample down to a thickness of 10 μm, electron transparency was obtained by ion milling.

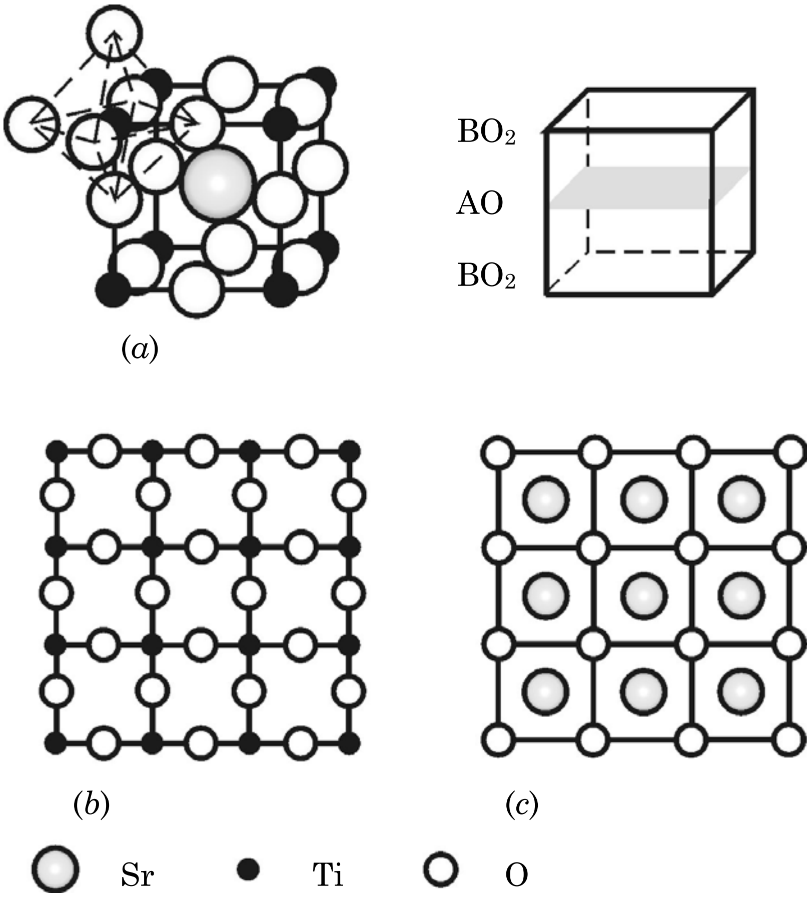

Figure 2.10: Schematic view of the $SrTiO_3$ unit cell with ABO_3 perovskite structure (a). The terminating plane can be either TiO_2, i.e., BO_2 (b) or SrO, i.e., AO (c).

2.5 $SrTiO_3$ substrate surface treatment

$SrTiO_3$, with lattice constant a = 3.905 Å (at room temperature) and thermal expansion coefficient $\alpha = 9 \times 10^{-6}\ K^{-1}$, is often chosen as substrate material for perovskite oxides with compatible lattice parameters, i.e., Y123 and $SrRuO_3$. To obtain epitaxial growth, atomically flat, crystalline surfaces are required, free of contaminants like CO_2 and H_2O. Both criteria are usually fulfilled by proper heat treatment. The resulting surface properties, i.e., morphology and terminating atomic plane of the $SrTiO_3$ substrate, however, affects the epitaxial growth, as will be shown in the following chapters. Since both the terminating atomic plane and surface morphology of as-received substrates are not well defined, additional surface treatment is necessary and will be addressed briefly.

2.5.1 $SrTiO_3$ substrate termination control

The $SrTiO_3$ unit cell, schematically depicted in figure 2.10 (a), consists of Ti occupying the corner position and Sr occupying the body center position. The Ti is 6-fold coordinated by oxygen, forming the corner-sharing oxygen octahedral. The structure of $SrTiO_3$ can be viewed as a stack of alternating SrO and TiO_2 planes along one of the principal axes, visualized in figure 2.10 (b) and 2.10 (c) respectively. This layered structure is of importance since it determines the surface termination of substrates cut perpendicular to one of the principal axes. Depending on the surface energy, the surface terminates either with SrO, TiO_2 or a mixture of both. A preference towards TiO_2 termination is predicted by surface energy calculations[24]. Several groups determined the surface composition of $SrTiO_3$ and showed that thermal treatments in oxygen[25,26,27,28] as well as reducing[29,30,31,32,33] environments result in any of the above-mentioned terminations. A reliable method to obtain a single termination is a chemical treatment. Here, the difference in solubility of SrO and TiO_2 in acids is employed. The first reported chemical procedure[34] to control the surface terminating layer utilizes a NH_4F buffered HF solution (pH ~4.5) for the removal of SrO from the surface without etching of the TiO_2. After subsequent thermal treatment a crystalline TiO_2 terminated $SrTiO_3$ surface is obtained. Using this procedure, however, a high density of etch pits[35] is frequently observed due to strong etching at defects of the crystalline surface. To avoid etch pits being formed a less strong acid has to be used and, consequently, the difference in solubility should be increased. The latter is obtained by soaking $SrTiO_3$ substrates in water[XX]. SrO in the outermost atomic layer of the substrate reacts with water and forms $Sr(OH)_2$ which is easily dissolved in acidic solutions. The Sr-hydoxide complex is removed by a short dip (~30 sec.) in a commercially available buffered HF solution (BHF)[XXI]. The short time in combination with the higher pH value of the solution prevents the formation of etch pits. Thermal treatment[XXII] at 950 °C and 1 atm of oxygen for typically 30 min[XXIII] is used to obtain the desired crystalline perfection of the substrate surface. In conclusion, this chemical procedure[18] enhances the selectivity

---

[XX] Here, we soaked the substrate in demineralised water (R=10-15 MΩcm and pH=6-7) for 10 min. using ultrasonic agitation.

[XXI] The BHF solution (NH_4F:HF=87.5:12.5, pH=5.5) was obtained from Merck.

[XXII] All thermal treatments have been performed in a modified tube-oven, using flowing O_2 (at a rate of 100-500 l/h). The substrates were placed on an aluminum-oxide boat inside a quartz tube.

[XXIII] The time depends on the vicinal angle of the substrates. To obtain straight step ledges at the substrate surface, 30 min. is used for substrates with vicinal angle between 0.1° and 0.5°. Longer time, typically 1-2 h, is necessary for substrates with lower vicinal angles.

in solubility by formation of the Sr-hydroxide complex and perfect crystalline TiO_2 terminated $SrTiO_3$ surfaces are reproducibly obtained.

Just recently, Van der Heide *et al.*[36] studied such TiO_2 terminated (001) $SrTiO_3$ surfaces and observed a well-ordered TiO_2 surface layer. Low-energy electron diffraction (LEED) patterns indicate a (1x1) structure whereas time-of-flight ion scattering and recoiling spectrometry (TOF-ISARS) indicate that the O-atoms are situated 0.1 Å above the Ti surface plane. A reconstructed surface, however, was observed after prolonged annealing ($T > 800$ °C) for several hours in O_2. This disordered surface exhibits a stronger Sr TOF-ISARS signal, whereas x-ray photoelectron spectroscopy (XPS) revealed Sr to be present in the surface plane, indicating Sr segregation towards the surface. A continuous accumulation of SrO on the surface of commercial available $SrTiO_3$ substrates has been observed[37] on prolonged annealing at 1000 °C. This provides evidence that these single crystals have not reached an equilibrium state after the thermal treatment during fabrication.

In conclusion, the (001) $SrTiO_3$ surface termination is very sensitive to surface treatments. Depending on the conditions, i.e., temperature, anneal time and environment, thermal treatments can lead to SrO, TiO_2 and a mixture of both in the terminating atomic plane.

2.5.2 $SrTiO_3$ surface morphology studied by AFM and RHEED

The surface morphology of $SrTiO_3$ substrates after different treatment was studied in detail[38,39]. Here, a few typical morphologies will be shown and discussed.

2.5.2.1 As-received substrate

The surface morphology of an as-received $SrTiO_3$ substrate[XXIV] after low temperature (650 °C) heat treatment in 1 atm of oxygen is shown in figure 2.11 (a). These surfaces typically consist of terraces with disordered step ledges. Both, ~2 Å and ~4 Å step heights have been observed, comparable to half and single unit cell step heights, respectively. From this we concluded a mixed termination, i.e., domains with a different terminating atomic layer, SrO or TiO_2, have been observed. The streaky RHEED pattern confirms the poor crystalline surface quality observed with AFM, see figure 2.11 (b).

[XXIV] $SrTiO_3$ substrates used in this study were obtained from ESCETE, single crystal technology B.V., Enschede, The Netherlands.

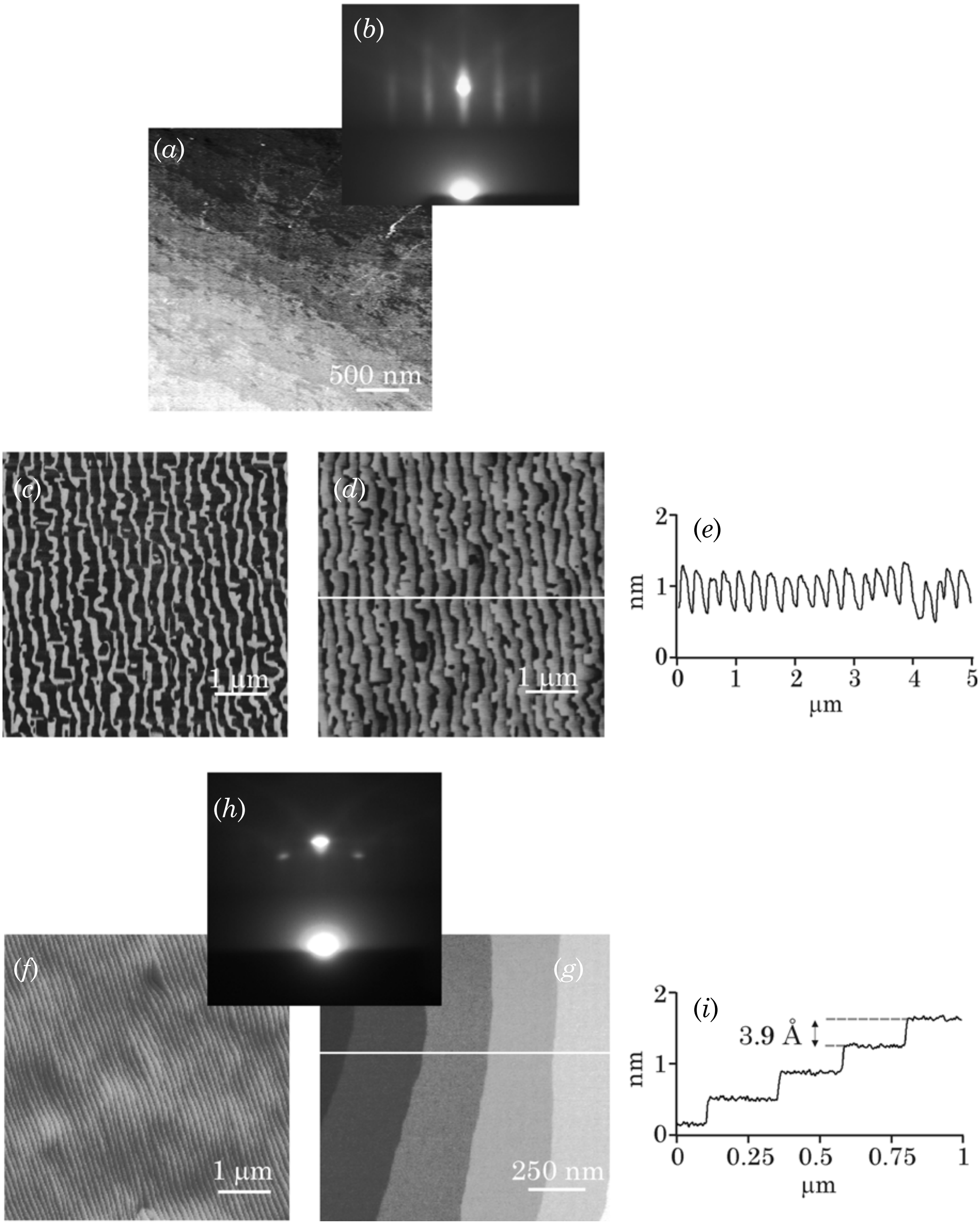

Figure 2.11: AFM micrograph (a) and RHEED pattern (b) of an as-received $SrTiO_3$ substrate. Friction contrast (c), AFM micrograph (d) and cross-section analysis (e) of an $SrTiO_3$ surface after thermal treatment at 950 °C for 4 h. AFM micrographs (f) and (g), RHEED pattern (h) and cross-section analysis (i) of a TiO_2 terminated $SrTiO_3$ surface obtained by chemical and thermal treatment at 950 °C, as described in section 2.5.1.

2.5.2.2 Thermal treatment

Figure 2.11 (d) shows an AFM micrograph of an as-received $SrTiO_3$ surface after thermal treatment at 950 °C in 1 atm of oxygen for 4 h. At this temperature re-crystallization of the surface occurs as shown by the clear step-terrace structure in figure 2.11 (d). Height analysis indicates that the step edge heights are comparable to a single unit cell step, see figure 2.11 (e). A large friction contrast, however, has been observed in the lateral force micrograph, indicative of a different surface termination, see figure 2.11 (c). Here, distinct regions with either SrO or TiO_2 termination are observed. This friction contrast is usually observed[40] on $SrTiO_3$ substrates after thermal treatment in oxygen at temperatures up to 1100 °C.

2.5.2.3 Optimal chemical treatment

Using the chemical treatment prior to the heat treatment, perfect single TiO_2 terminated $SrTiO_3$ substrates were obtained. The AFM micrographs in figure 2.11 (f) and (g) show a clear and regular step-terrace structure, with single unit cell step heights, see figure 2.11 (i). Compared to the thermal treatment, the step ledges have a different character. Without chemical treatment straight terrace ledges, aligned along low-index directions, are observed, whereas with the chemical treatment more rounded ledges are observed. In the latter case, the edge energy is clearly minimized by decreasing the ledge length. No friction contrast has been observed on such surfaces, indicative of the single termination. This perfect crystalline surface produces clear 2D dots in the RHEED pattern, see figure 2.11 (h).

2.6 Conclusions

PLD differs from other PVD techniques because of two unique features: the wide range in the kinetic energy of the ablated particles arriving at the substrate and the high deposition rate during the pulse. Both features can be exploited to manipulate the growth characteristics. A change in the kinetic energy of the impinging particles results in a change of the effective diffusion coefficient, whereas the high supersaturation during the deposition pulse is used to impose layer-by-layer like growth[XXV]. The short deposition pulses, typical for PLD, cause a separation of the deposition and growth in time: almost no nucleation and growth takes place during the deposition pulse. Determination of the kinetic growth parameters from RHEED intensity variations in between the deposition pulses is, therefore, less complicated, see chapter 3 and 4.

[XXV] See chapter 3 for a detailed description

RHEED is considered as an ultra-high vacuum analysis tool in many textbooks. Consequently, RHEED has been utilized in low-pressure thin film growth techniques like MBE. The development of high-pressure RHEED enabled growth monitoring and growth characterization at the high pressures used in PLD. Growth control in PLD on an atomic level is, therefore, feasible; making PLD an advanced research technique.

First growth studies with high-pressure RHEED showed the influence of the substrate morphology on the (initial) growth of complex oxides by PLD. Since the evolution of the film surface morphology is one of the key processes in thin film growth, atomically flat and crystalline substrate surfaces are essential for the controlled growth of atomically flat thin films. In the case of perovskite substrates, not only an atomically flat and crystalline surface but also a single termination is essential for the growth of complex oxides. For instance, the terminating layer of the substrate determines the atomic layer stacking sequence at the substrate-thin film interface in the heteroepitaxial growth of Y123 on $SrTiO_3$, see chapter 5.

Perfect, atomically flat and crystalline $SrTiO_3$ substrate surfaces with TiO_2 termination are obtained using the two-step chemical procedure. Here, the etch selectivity of SrO with respect to TiO_2 is enhanced. Shorter etching time in combination with a higher pH value of the etchant avoid formation of etch pits.

References

1 A.J.H.M.Rijnders, G.Koster, D.H.A.Blank and H.Rogalla, *Appl.Phys. Lett.* **70**, 1888 (1997)

2 M.K. Wu, J.R. Ashburn, C.J. Torng, P.H. Hor, R.L. Meng, L. Gao, Z.J. Huang, Y.Q. Wang and C.W. Chu, *Phys. Rev. Lett.* **58**, 908 (1987)

3 D. B Geohegan, *Thin Solid Films* **220**, 138 (1992)

4 D.B. Geohegan in *Laser Ablation of Electronic Materials: Basic Mechanisms and Applications*, E. Fogarassy and S. Lazare Eds. (North Holland, Amsterdam, 1992), p. 73

5 Mikhail Strikovski and John H. Miller, *Appl. Phys. Lett.* **73**, 1733 (1998)

6 B. Dam, B. Stäuble-Pümpin, *J. Mat. Sci.: Mat. in Elec.* **9**, 217 (1998)

7 D.H.A. Blank, G.J.H.M. Rijnders, G. Koster and H. Rogalla, *Appl. Surf. Sci.* **138-139**, 17 (1999)

8 M. Tyunina, J. Levoska and S. Leppävuori, *J. Appl. Phys.* **83**, 5489 (1998)

9 T. Okada, Y. Nakata, M. Maeda, W.K.A. Kumuduni, *J. Appl. Phys.* **82**, 3543 (1997)

10 J. Cheing, J. Horwitz, *MRS Bulletin* **XVII**, 30 (1992)

11 D.B. Geohegan and A.A. Puretzky, *Appl. Phys. Lett.* **67**, 197 (1995)

12 M.Y. Chern, A. Gupta and B.W. Hussey, *Appl. Phys. Lett.* **60**, 3045 (1992)

13 I.V. Markov, *Crystal growth for beginners*, chapter 1 (World Scientific, 1994)

14 V.M. Fuenzalida, *J. Cryst. Growth* **183**, 497 (1998)

15 V.M. Fuenzalida, *J. Cryst. Growth* **213**, 157 (2000)

16 M.G. Lagally, D.E. Savage and M.C. Tringides in *Reflection high energy electron diffraction and reflection electron imaging of surfaces*, P.K. Larsen and P.J. Dobson Eds. (Plenum Press, London, 1989), pp. 139–174

17 T. Kawamura in *Reflection high energy electron diffraction and reflection electron imaging of surfaces*, P.K. Larsen and P.J. Dobson Eds. (Plenum Press, London, 1989), pp. 501-522

18 G. Koster, B.L. Kropman, G.J.H.M. Rijnders, D.H.A. Blank and H. Rogalla, *Appl. Phys. Lett.* **73**, 2920 (1998)

19 P.R. Pukite, P.I. Cohen and S Batra in *Reflection high energy electron diffraction and reflection electron imaging of surfaces*, P.K. Larsen and P.J. Dobson Eds. (Plenum Press, London, 1989), pp. 427-447

20 J.H. Neave, B.A. Joyce, P.J. Dobson, and N. Norton, *Appl. Phys.* **A 31**, 1 (1983)

21 G. García, F. Blanco and A. Williart, *Chem. Phys. Lett.* **335**, 227 (2001)

22 H. Karl and B. Stritzker, *Phys. Rev. Lett.* **69**, 2939 (1992)

23 G. García, M. Roteta and F. Manero, *Chem. Phys. Lett.* **264**, 589 (1997)

24 S.P. Chen, *J. Mater. Sci.* **13**, 8148 (1998)

25 B. Stäuble-Pümpin, B. Ilge, V.C. Matijasevic, P.M.L.O. Scholte, A.J. Steinfort and F. Tuinstra, *Surf. Sci.* **369**, 313 (1996)

26 F. Wang, M. Badaye, K. Ogawa and T. Morishita, *Appl. Surf. Sci.* **90**, 123 (1995)

27 R. Sum, R. Lüthi, H.P. Lang and H.-J. Güntherodt, *Physica C* **235-240**, 621 (1994)

28 N. Ikemiya, A.. Kitamura, S. Hara, *J. Cryst. Growth* **160**, 104 (1996)

29 T. Matsumoto, H. Tanaka, K. Kouguchi, T. Kawai and S. Kawai, *Surf. Sci.* **312**, 21 (1994)

30 H. Tanaka, T. Matsumoto, T. Kawai and S. Kawai, *Jpn. J. Appl. Phys.* **32**, 1405 (1993)

31 H. Tanaka, T. Matsumoto, T. Kawai and S. Kawai, *Surf. Sci.* **318**, 29 (1994)

32 Y. Liang and D.A. Bonell, *Surf. Sci.* **310**, 128 (1994)

33 Y. Liang, J.B. Rothman and D.A. Bonell, *J. Vac. Sci. Technol.* **A12**, 2276 (1994)

34 M. Kawasaki, K. Takahashi, T. Maeda, R. Tsuchiya, M. Shinohara, O. Ishiyama, T. Yonezawa, M. Yoshimoto and H. Koinuma, *Science* **226**, 1540 (1994)

35 G.Koster, B.L. Kropman, G.J.H.M Rijnders, D.H.A. Blank and H. Rogalla , *Mat. Sci. & Eng.* **B 56**, 209 (1998)

36 P.A.W. van der Heide, Q.D. Jiang, Y.S. Kim and J.W. Rabalais, *Surf. Sci.* **473**, 59 (2001)

37 K. Szot, W. Speier, U. Breuer, R. Meyer, J. Szade and R. Waser, *Surf. Sci.* **460**, 112 (2000)

38 B.L. Kropman, *Self-assembly of alkylsiloxane monolayers on perovskite surfaces.* PhD thesis ISBN 903651200x, University of Twente, chapter 6 (1998)

39 G. Koster, *Artificially layered oxides by pulsed laser deposition*, PhD thesis ISBN 9036513367, University of Twente, chapter 3 (1999)

40 J. Fompeyrine, R. Berger, H.P. Lang, J. Perret, E. Mächler, Ch. Gerber and J.-P. Locquet, *Appl. Phys. Lett.* **72**, 1697 (1998)

Chapter 3

Growth kinetics

3.1 Introduction

The application of thin films in electronic devices, relying on multilayer technology, requires (atomically) smooth film surfaces and interfaces. Understanding of the different mechanisms affecting the growth mode is, therefore, necessary to control the surface morphology during thin film growth.

Two independent processes, i.e., nucleation and growth of islands, play an important role during vapor-phase epitaxial growth on an atomically flat surface. Here, nucleation causes the formation of surface steps and subsequent growth causes the lateral movement of these steps. Both processes are determined by kinetics, since they take place far from thermodynamic equilibrium. These kinetic processes affect the final surface morphology and are, therefore, extensively studied. This chapter gives a brief description of the growth modes mentioned in literature and related kinetic parameters.

The applicability of high-pressure RHEED to extract the kinetic parameters, determining the growth of complex oxides in PLD, will be demonstrated. As mentioned in chapter 2, the deposition and growth are separated in time in PLD. This enables us to measure the kinetic parameters at growth conditions by monitoring the decay of the adatom density between the deposition pulses. In this chapter the homoepitaxial growth of $SrTiO_3$ is used as a model system to study the influence of growth kinetics during PLD.

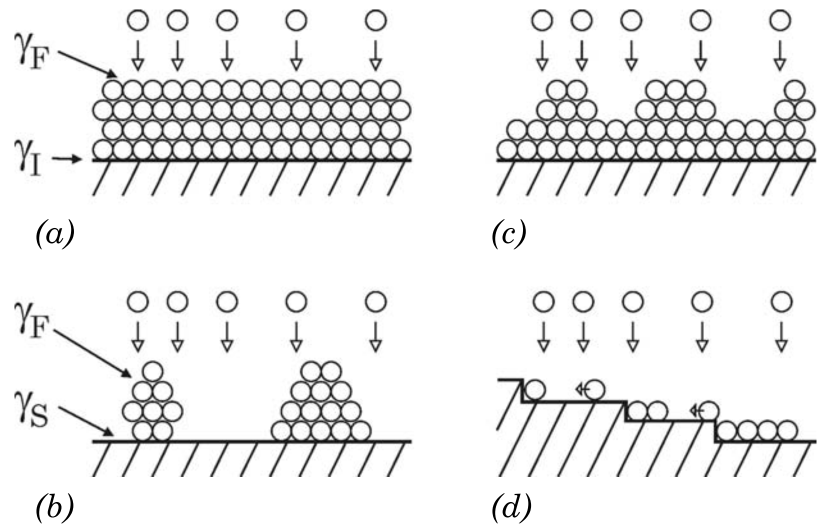

Figure 3.1: Film growth modes: layer-by-layer; Frank-Van der Merwe (a), island; Volmer-Weber (b), Stranski-Krastanov (c) and step flow (d).

3.2 Growth modes at thermodynamic equilibrium

The thermodynamic approach to crystal growth is used to describe crystal growth close to equilibrium, i.e., for a thermodynamically stable system. Local fluctuations from equilibrium lead to nucleation, which give rise to a phase transition from, for instance, the gas to the solid phase. A supersaturated[1] gas phase is a prerequisite for the formation of these nuclei, whereas the formation probability is determined by the activation energy. Nuclei will be formed until a critical density is reached. From this point onwards the nuclei will grow and crystallization progresses.

This thermodynamic approach has been used to determine growth modes of thin films close to equilibrium[2], i.e., only at small or moderate supersaturation. In this approach the balance between the free energies of film surface (γ_F), substrate surface (γ_S) and the interface between film and substrate (γ_I) is used to determine the film morphology. Three different growth modes, schematically depicted in figure 3.1, can be distinguished. In the case of layer-by-layer growth (figure 3.1 (a); Frank-van der Merwe growth mode), the total surface energy of the wetted substrate is lower than the surface energy of the bare substrate. That is, the strong bonding between film and substrate reduces γ_I such that $\gamma_F + \gamma_I < \gamma_S$.

On the other hand, when there is no bonding between film and substrate, three-dimensional (3D) islands are formed. The film does not wet the substrate because this would lead to an increase of the total surface energy. This growth mode is referred to as the Volmer-Weber growth mode, see figure 3.1 (b). In heteroepitaxial growth, the so-called Stranski-Krastanov growth mode can occur, see figure 3.1 (c).

Here, the growth mode changes from layer-by-layer to island growth. During heteroepitaxial growth, the lattice mismatch between substrate and film gives rise to biaxial strain, resulting in an elastic energy that grows with increasing layer thickness. Misfit dislocations at or near the substrate-film interface will be formed if the layer thickness exceeds a critical thickness h_C. At this thickness it is thermodynamically favorable to introduce dislocations because the elastic energy, relieved by the dislocations, becomes comparable to the increase in the interfacial energy. In other words, misfit dislocations are necessarily introduced to relieve the mismatch strain[I] and are, therefore, equilibrium defects.

3.3 Growth kinetics

In many vapor-phase deposition techniques, e.g., PLD, the growing film is usually not in thermodynamic equilibrium and kinetic effects have to be considered. Because of the limited surface diffusion, the deposited material cannot rearrange itself to minimize the surface energy. The high supersaturation of the vapor leads to a large nucleation rate, and kinetic effects will lead to the occurrence of different growth modes.

3.3.1 Homoepitaxial growth modes

In homoepitaxial growth the deposited material is identical to the substrate material and the crystalline structure of the substrate is extended into the growing film. Complicating effects like lattice parameter misfit and thermal expansion coefficients do not play a role. Consequently, only 2D growth modes are expected, depending on the behavior of the deposited species[3]. This behavior is determined by a number of kinetic parameters. Among them are the surface diffusion coefficient (D_S) of the adatoms, the sticking probability of an adatom arriving the edge of a terrace and the additional energy barrier (E_S) for adatoms to descend the edge to a lower terrace. Of the mentioned kinetic parameters, the diffusion coefficient is probably the most important. It determines the average distance an atom can travel on a flat surface before being trapped. This distance is the surface diffusion length l_D and can be defined by:

$$l_D = \sqrt{D_S \tau} \tag{3.1}$$

[I] In order to relieve the misfit strain, the Burgers vector of the dislocation should have a component parallel to the substrate surface. Two extreme cases of misfit dislocations are edge dislocations (Burgers vector is directed perpendicular to the dislocation) and screw dislocations (Burgers vector is directed parallel to the dislocation). Usually, dislocations have a mixed character.

where τ is the residence time before re-evaporation. The surface diffusion coefficient D_S is generally expressed as:

$$D_S = \nu a^2 \, exp\left(-\frac{E_A}{k_B T} \right) \tag{3.2}$$

where E_A is the activation energy for diffusion, ν the attempt frequency and a the characteristic jump distance. From eq. (3.2) it is clear that the deposition temperature is important because it controls the diffusivity of the adatoms. To understand the possible 2D growth modes on both singular and vicinal substrates, two diffusion processes have to be considered. First, the diffusion of atoms on a terrace (intralayer mass transport) and second the diffusion of an atom to a lower[II] terrace (interlayer mass transport). Both processes are determined by the kinetic parameters.

Fast intralayer mass transport will lead to step flow growth on a vicinal surface, see figure 3.1 (d). In this case l_D is sufficiently larger than the average terrace width l_T. The mobility of adatoms is high enough to enable atoms to reach the edges of the substrate steps. Here, steps act as a sink for the deposited atoms diffusing towards the steps and nucleation on the terraces is prevented. As a result, the steps will propagate, leading to step flow growth. A growing vicinal surface will be stable if both the terraces keep the same width and the step ledges remain straight. Otherwise, step meandering or step bunching can occur and, subsequently, the distribution in l_T broadens.

If the intralayer mass transport is not fast enough, nucleation on the terraces occur. Initially, nuclei will be formed until a saturation density is reached. After the saturation, the probability for atoms to attach to an existing nucleus exceeds the probability to form a new nucleus and islands will start to grow. The interlayer mass transport will have a large effect on the growth mode in this case. Two extreme growth modes can be distinguished, i.e., ideal layer-by-layer growth and ideal multilayer growth[III]. To obtain a layer-by-layer growth mode a steady interlayer mass transport must be present; atoms deposited on top of a growing island must, first reach the island edge and second, diffuse to the lower layer. In the ideal case, layer-by-layer growth is obtained if nucleation starts after completion of a layer. When there is no or very limited interlayer mass transport, nucleation will occur on top of islands before these islands have coalesced. This so-

---

[II] Because of the higher coordination number for atoms at a step, diffusion of atoms to a higher terrace is usually neglected.

[III] Here, ideal refers to multilayer growth with no interlayer mass transport.

called second layer nucleation[IV] will lead to multilayer growth. The growth mode in real systems far from equilibrium will be in between the two extreme growth modes.

3.3.2. Homoepitaxial growth study of $SrTiO_3$.

The specular RHEED intensity, monitored during homoepitaxial growth of $SrTiO_3$ at the deposition temperature of 850, 750 and 650 °C is depicted in figure 3.2 (a), (b) and (c), respectively. The oxygen deposition pressure was set to 3 Pa. At these conditions[V], 2D nucleation and growth is observed, indicated by the clear intensity oscillations. The oscillation periods correspond to the deposition time of one unit cell layer. At the highest temperature, full recovery is obtained at completion of every unit cell layer. Here, the growth mode can be described as ideal unit cell layer-by-layer.

The angle of incidence of the electron beam (e-beam) was ~1°, resulting in a diffraction condition corresponding to the in-phase condition. Reflections from unit cell layers at different levels add constructively and a constant maximum intensity is predicted by the kinematic theory[VI] at this condition. Still, RHEED intensity variations are observed at the in-phase diffraction condition, caused by diffuse scattering at surface step edges. As mentioned in chapter 2, electrons are easily scattered out of the specular beam by the step edges since the unit cell layer thickness is much larger than the wavelength of the electrons. The specular RHEED intensity is, therefore, a measure of the surface step density. During 2D nucleation and growth, oscillation of the step density is expected caused by the periodic formation, i.e., nucleation and coalescence, of growing islands. Note that a minimum specular RHEED intensity will be observed at the maximum step density.

[IV] The probability for second layer nucleation is related to a critical island size R_C. It is the mean island radius at a critical time during sub-monolayer growth where stable clusters nucleate on top of the islands. If R_C is small compared to the mean distance between islands in the first layer, islands will nucleate a second layer and multilayer growth will occur. An important parameter, which influences R_C, is the energy barrier for atoms to descend across the step edge to a lower terrace. An additional energy step edge barrier E_S has to be overcome if this energy barrier is large compared to E_A. Large values of E_S will lead to accumulation of adatoms on top of islands, leading to an increased second layer nucleation rate and, therefore, to a smaller value of R_C.

[V] The distance between target and substrate was set to 58 mm, the laser energy density on target to 1.3 J/cm^2 and the spot size to 1.4 mm^2.

[VI] Reflections from unit cell layers at different level add destructively at the out-of-phase condition.

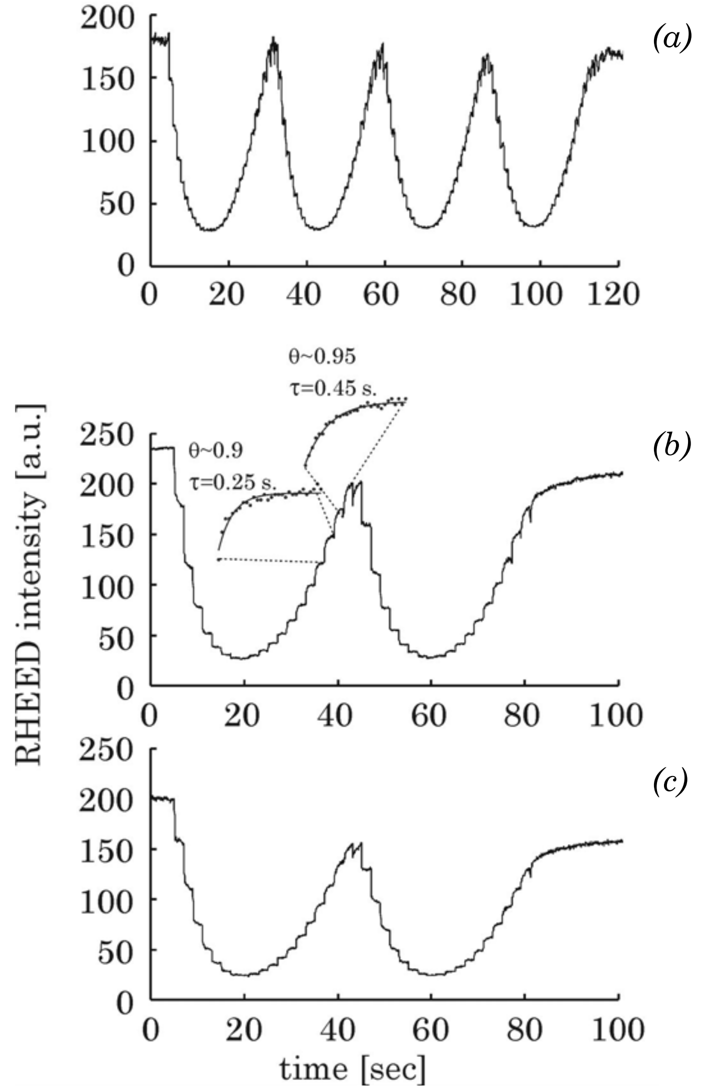

Figure 3.2: Specular RHEED Intensity oscillations during homoepitaxial growth of $SrTiO_3$ at 3 Pa, 850 °C (a), 750 °C (b) and 650 °C (c). The insets in (b) show the enlarged intensities after a laser pulse at different coverage.

Assuming instantaneous nucleation[VII] and subsequent 2D growth of equally spaced islands by step propagation, the step density S can be determined by the widely used step density model[4,5]. Without second layer nucleation, S is given by:

$$S = 2\sqrt{\pi N_S}\left(1-\theta\right)\sqrt{-ln\left(1-\theta\right)} \tag{3.3}$$

[VII] Instantaneous nucleation can be expected during PLD because of the high pulse deposition rate and, subsequently, a high supersaturation within the deposition pulse, see chapter 2.

where N_S is the number of nuclei per unit area. Both the diffusivity of the deposited material and deposition rate determine the quantity N_S and, therefore, the amplitude of the step density oscillation. The shape of the RHEED intensity oscillations, measured at the in-phase diffraction condition during homoepitaxial growth of $SrTiO_3$, supports the applicability of the step density model. A maximum step density $S_{MAX} = \sqrt{2\pi N_S / e}$ is reached at a surface coverage $\theta \sim 0.39$[VIII]. This corresponds to the observed RHEED intensity minimum at θ ~0.4 in figure 3.2.

3.3.2.1. Determination of kinetic growth parameters on singular surfaces.

The RHEED intensities in figure 3.2 are clearly modulated by the laser pulse, giving rise to the typical RHEED intensity relaxations[6,7]. Following the model described above, i.e., instantaneous nucleation just at the start of every monolayer, this relaxation behavior is attributed to particles[IX] diffusing towards the step edges of the islands. Incorporation of these particles at the step edges causes the islands to grow resulting in a change in the step density. The evolution of the step density after every pulse is, therefore, a direct result of the decay of the density of the diffusing particles, which depends on the diffusivity and the average travel distance, see eq. (3.1). This distance is determined by the nucleation density N_S and the average island size. The latter depends on the coverage and gives rise to the coverage dependent characteristic relaxation times, see figure 3.2 (b). This dependence is illustrated by the following proposed model. The density of diffusing particles[X] on top of a circular, 2D island can be found by solving the time dependent diffusion equation[8] given by:

$$\frac{\partial^2 n_S}{\partial r^2} + \frac{1}{r}\frac{\partial n_S}{\partial r} = \frac{1}{D_S}\frac{\partial n_S}{\partial t} \tag{3.4a}$$

with the initial condition $n_S(r,0) = n_0$, the density of instantaneously deposited particles due to one laser pulse. The boundary conditions are given by:

$$n_S(r = r_0) = n_{SE} \tag{3.4b}$$

and

[VIII] At constant rate of nucleation and step propagation a maximum in the step density is expected at coverage $\theta = 0.5$.

[IX] Particles are the metal atoms or metal-oxide molecules.

[X] Here, no nucleation on top of islands is assumed.

$$\left(\frac{\partial n_S}{\partial r}\right)_{r=0} = 0 \tag{3.4c}$$

where n_{SE} is the equilibrium density at the island edge; n_{SE}~0 assuming the edge acts as a perfect sink[XI]. The solution of eq.'s (3.4) is of the form:

$$n_S(r,t) = n_0 \sum_{m=1}^{\infty} A_m(r;r_0)\, exp\left(-\frac{t}{\tau_m}\right) \tag{3.5}$$

where τ_m is given by:

$$\tau_m = \frac{r_0^2}{D_S\left(\mu_m^{(0)}\right)^2} \tag{3.6}$$

$A_m(r;r_0)$ are pre-factors depending only weakly on r and r_0. Eq. (3.5) converges rapidly and, for long enough time, only the first term needs to be considered ($\mu_m^{(0)}$ are the roots of Bessel functions, $\mu_1^{(0)}$=2.40). Without nucleation on top of the 2D island, an exponential decrease in the density of diffusing particles is expected after the deposition pulse. This exponential decrease depends on the size of the growing islands, which depend on the coverage by:

$$\pi {\rho_2}^2(t) = \frac{\theta(t)}{N_S} \tag{3.7}$$

where $\pi {\rho_2}^2(t)$ is the area of the islands, see figure 3.3. Substituting eq. (3.7) into eq. (3.6) gives the exponential decay time of diffusing particles on top of a 2D island as function of the coverage θ:

$$\tau_2 = \frac{\theta}{D_S\left(\mu_1^{(0)}\right)^2 \pi N_S} \tag{3.8}$$

[XI] For this to be true the step edge must be non-reflecting. This is valid if the additional step edge energy barrier E_S~0.

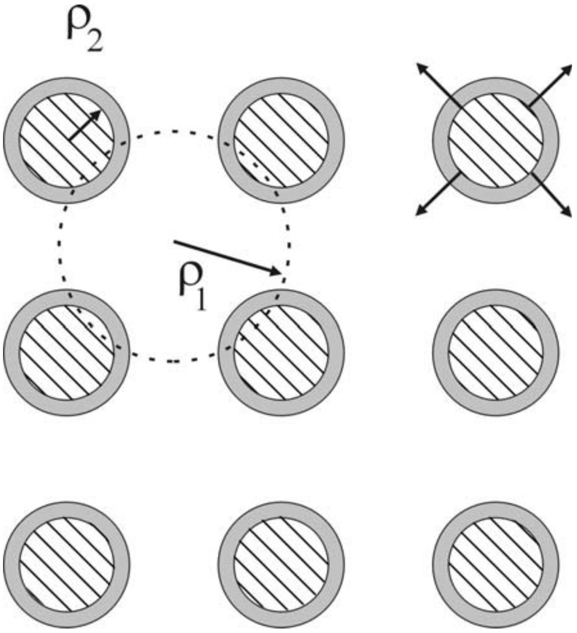

Figure 3.3: Schematic view of the coverage θ*, given by the (hatched) area of the 2D islands. The density is determined by the nucleation density* N_S*.*
ρ_2 *represents the radius of the islands at given coverage* θ*, whereas* ρ_1 *represents the radius of the area between the growing islands, given by* $1\text{-}\theta$*. The grey area represents the change in coverage due to one deposition pulse.*

The index 2 indicates diffusing particles at the 2nd level, i.e., on top of the islands. The same approach can be followed for diffusing particles deposited between the islands. Here, the maximum travel distance of a diffusing particle is also determined by the coverage dependent size of the islands (see figure 3.3). The area between the islands can be approximated by:

$$\pi\rho_1^{\,2}(t) = \frac{1-\theta(t)}{N_S} \tag{3.9}$$

Substituting eq. (3.9) into eq. (3.6) gives the exponential decay time (now indexed 1) of diffusing particles between 2D islands as function of the coverage θ:

$$\tau_1 = \frac{1-\theta}{D_S\left(\mu_1^{(0)}\right)^2 \pi N_S} \tag{3.10}$$

From the equations above, it follows that with increasing coverage the decay time in the density of diffusing particles on top of a growing island increases. On the other hand, the decay time in the density of diffusing particles between islands decreases with increasing coverage.

The change in the coverage $\Delta\theta(t)$ after a deposition pulse can be approximated by:

$$\Delta\theta_n(t) = \frac{\theta_{n-1}}{n_P}\left(1 - exp\left(-\frac{t}{\tau_2}\right)\right) + \frac{(1-\theta_{n-1})}{n_P}\left(1 - exp\left(-\frac{t}{\tau_1}\right)\right) \tag{3.11}$$

where θ_{n-1} is the coverage before applying the pulse and n_P the number of pulses needed for completion of one monolayer, i.e., $\theta = 1$. Here, $\frac{1}{n_P}$ represents the density of deposited particles. Multiplication of this density with θ_{n-1} and $(1-\theta_{n-1})$

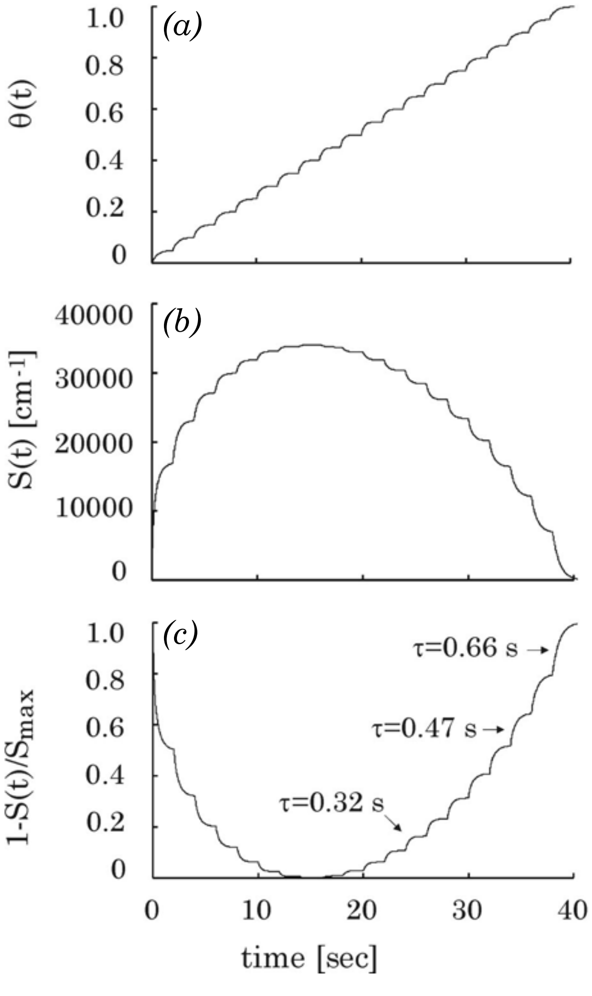

Figure 3.4: Calculated coverage $\theta(t)$ *during monolayer growth (a), the corresponding surface step density* $S(t)$ *(b) and corresponding RHEED intensity, given by* $1 - S(t)/S_{max}$ *(c). Here, the nucleation density* N_S *is* $2x10^{11}/cm^2$*, the temperature is 850 °C, the energy barrier of diffusion* E_A *is 2.2 eV and the number of pulses for one monolayer* n_P *is 20.*

gives the total number of particles, expressed in θ, deposited on top and in between the islands, respectively.

Figure 3.4 (a) shows $\theta(t)$ for N_S = 2x10^{11}/cm^2, T = 850 °C, E_A = 2.2 eV and n_P = 20, calculated using the model described above[XII]. Using eq. (3.3) the evolution of the step density $S(t)$ can be calculated, see figure 3.4 (b). Assuming a direct coupling between $S(t)$ and the diffuse scattering of electrons, the reflected RHEED intensity is approximated by:

$$I(t) \propto 1 - \frac{S(t)}{S_{max}} \tag{3.12}$$

which is shown in figure 3.4 (c) for the parameters given above. The simple model describes the observed RHEED intensity variations in figure 3.2 qualitatively, as shown by the coverage dependent characteristic relaxation time after every pulse. However, the observed RHEED intensity shows a pronounced decrease in the intensity just after each pulse is applied. This effect is especially visible in figure 3.2 (b) at coverage close to unity. This difference can be explained by the contribution of the diffusing particles. Not only surface steps, but also the diffusing particles themselves act as diffuse scatterers[9] for electrons. The decay in the particle density n_S on top and between the islands is described by eq. (3.5) using the time constants given by eq. (3.8) and eq. (3.10), respectively. Assuming a direct coupling of the averaged particle density and the diffusive scattered intensity, an exponential increase of the intensity is expected, given by:

$$I \sim I_0\left(1 - exp\left(-\frac{t}{\tau}\right)\right) \tag{3.13}$$

where I_0 is determined by the particle density just after the deposition pulse and τ given by eq. (3.8) and (3.10) for particles deposited on top and in between the island. Here, only the first term of eq. (3.5), i.e., m=1 is used.

The evolution of the step density and the density of diffusing particles determine the relaxation behavior of the RHEED intensity. The time dependence of both is expected to be comparable, since the two contributions are coupled. At coverage close to unity (θ = 0.7-1), most of the deposited material is deposited on top of the growing islands and only one time constant has to be considered.

At these values of the coverage, the characteristic relaxation times can be used to estimate the activation energy for diffusion E_A. Figure 3.5 (a) and (b) show the

---

[XII] The parameters are chosen such that the density of diffusing particles is approximately zero before the next pulse is applied.

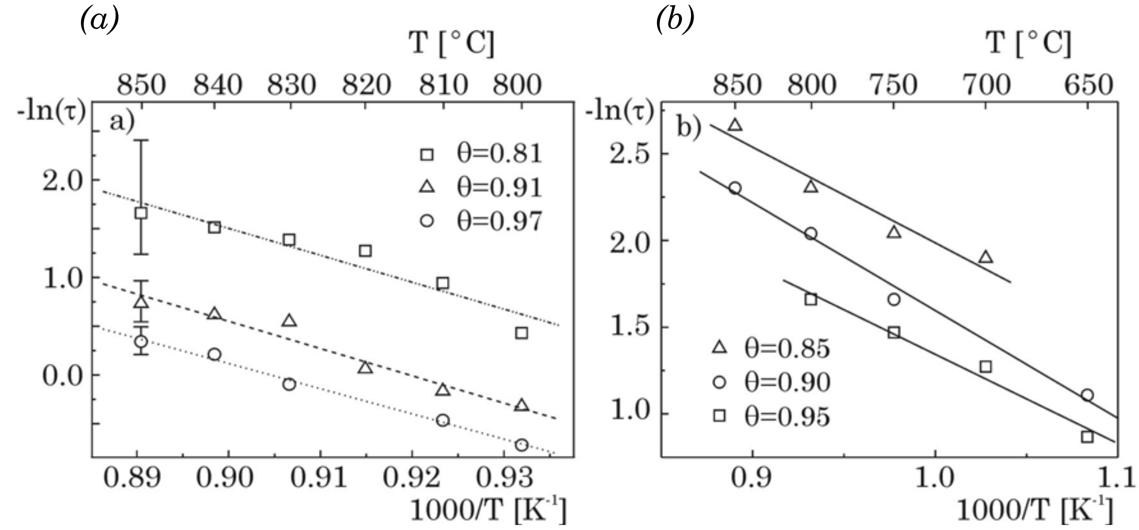

Figure 3.5: The Arrhenius plot for the relaxation times obtained from a fit with eq. (3.13) for different coverage and temperature at oxygen deposition pressure of 20 Pa (a) and 3 Pa (b).

characteristic relaxation time versus temperature for different values of the coverage during the homoepitaxial growth of $SrTiO_3$ at a deposition pressure of 20 and 3 Pa, respectively. A value for E_A of 2.2 ± 0.2 eV is derived for a deposition pressure of 20 Pa, and 0.48 ± 0.05 eV for a deposition pressure of 3 Pa. The difference is attributed to the kinetic energy of the arriving particles at the substrate.

At the pressure of 20 Pa the visible plasma range was smaller than the target-to-substrate distance and the particles are expected to be thermalized[10], see chapter 2. At the lower pressure of 3 Pa the kinetic energy of the particles is expected to be larger, leading to a reduced effective energy barrier for diffusion.

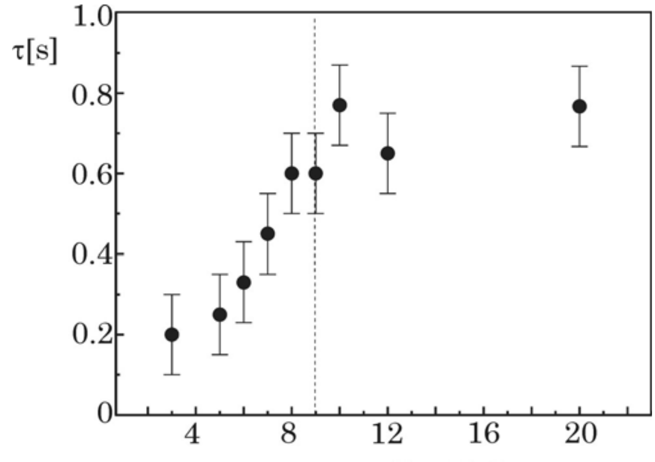

Figure 3.6: Relaxation time versus oxygen deposition pressure for θ ~0.95 and substrate temperature of 850 °C.

In figure 3.6, the relaxation times are plotted versus the oxygen deposition pressure at a constant temperature of 850 °C. At deposition pressures below 9 Pa, an increase in the relaxation time is observed at increasing deposition pressure and, consequently, a smaller kinetic energy of the arriving particles. However, above 9 Pa, the relaxation time is almost independent of the deposition pressure. At these higher pressures, the arriving particles are expected to be thermalized.

Reliable determination of the activation energy for diffusion E_A from the temperature dependent characteristic relaxation times is only possible assuming the average travel distance for diffusing particles to be approximately constant in the temperature range of interest. That is, only small variations in the step density S are allowed and, as a consequence, only small variations of the coverage θ and the nucleation density N_S are allowed, see eq. (3.8) and (3.10). The first requirement is easily obtained by depositing a sufficiently small amount of material in one pulse. The latter, however, is affected by the supersaturation $\Delta\mu$ and diffusivity D_S of the material. Both depend on the substrate temperature; with increasing temperature $\Delta\mu$ decreases and D_S increases. Consequently, the nucleation density N_S is not expected to be constant in a wide temperature range. A higher nucleation density N_S at lower temperature decreases the average travel length of the deposited material and the corresponding relaxation times will decrease, see eq. (3.8) and (3.10).

In conclusion, varying the temperature not only changes the diffusivity D_S but also N_S. As a result, the slope in the Arrhenius plots decrease and, subsequently, a smaller value for E_A is determined.

To overcome the temperature dependent nucleation density and corresponding change in the average travel distance, step flow growth can be employed. No nucleation takes place during this growth mode, resulting in a steady average travel distance. Extraction of the energy barrier for diffusion during step flow growth is, therefore, more reliable, as will be discussed in the following section.

3.3.2.2. Determination of kinetic growth parameters on vicinal surfaces.

The transition from 2D to step flow growth on a vicinal substrate is often used to determine the adatom diffusion length. Either the substrate temperature, determining the surface diffusion length l_D, or the vicinal angle, determining the terrace width l_T, is changed. A transition occurs when the diffusion length of adatoms becomes comparable to the terrace width, i.e., $l_D \approx l_T$. It has been proposed[11] to use RHEED to determine this transition as a function of the growth conditions. This technique has been used by several groups[12,13,14] to estimate the surface migration parameters. The RHEED intensity is expected to be constant during step flow growth, whereas RHEED intensity oscillations occur during 2D nucleation and growth.

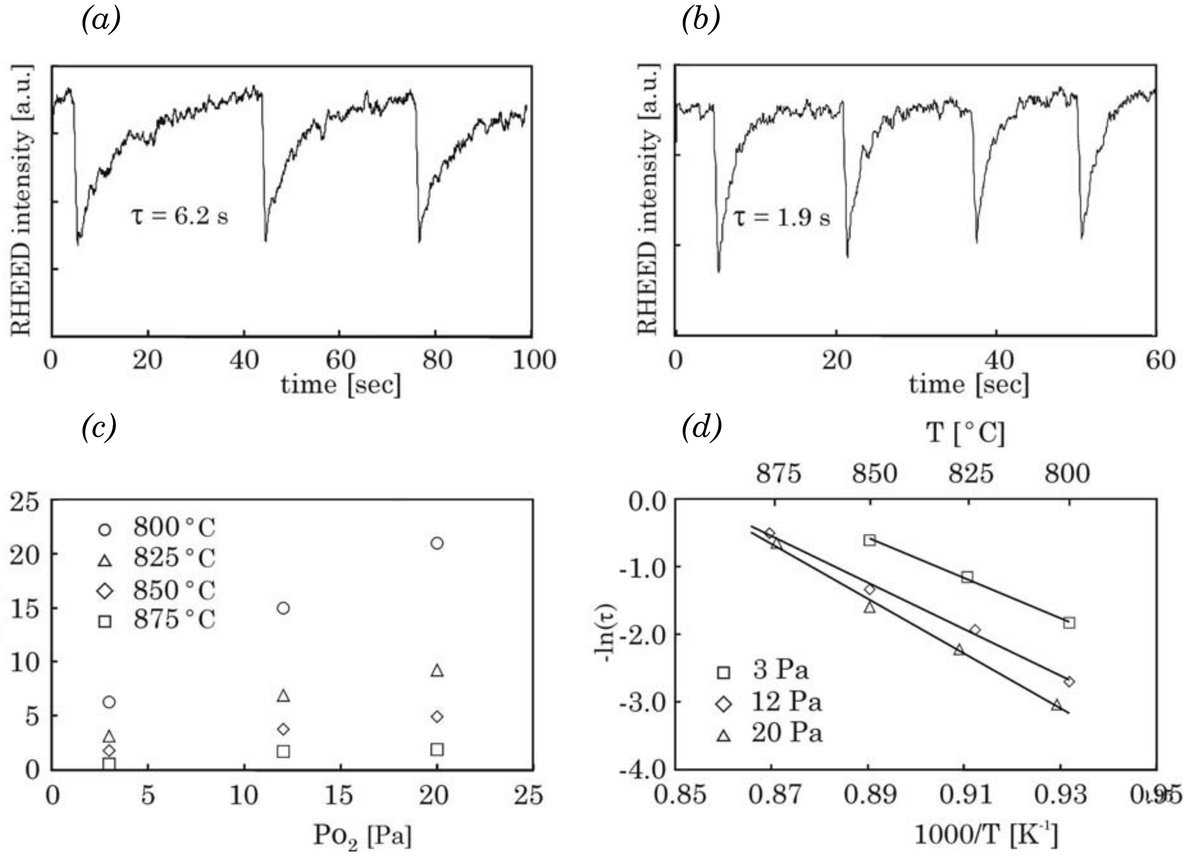

Figure 3.7: Specular RHEED intensity variations during homoepitaxial step flow growth of $SrTiO_3$ at oxygen deposition pressure of 3 Pa and 800 °C (a) and at 20 Pa and 875 °C (b). Relaxation times obtained from a fit with eq. (3.13) for different temperature and oxygen deposition pressure (c) and the same values in the Arrhenius form (d).

However, nucleation, being a stochastic process, can take place on a terrace smaller than the diffusion length. Furthermore, the absence of RHEED intensity oscillations is not always a clear signature of pure step flow growth. Even when a steady RHEED intensity is observed, nucleation on the terraces may occur. Such a "mixed" growth mode causes a constant step density and, therefore, a constant RHEED intensity. This growth behavior is observed during growth of $SrRuO_3$ on vicinal TiO_2 terminated $SrTiO_3$ and will be discussed in chapter 4.

During step flow growth, the step ledges of the vicinal substrates act as a sink for diffusing particles and nucleation on the terraces is prevented, resulting in a steady step density, determined by the vicinal angle of the substrate. The coverage dependent average island size in 2D nucleation and growth is replaced by the constant average terrace width of the vicinal substrate. Measurements of RHEED characteristic relaxation times during step flow growth at different temperature can, therefore, be used to determine the energy barrier for diffusion more reliably. The relaxation time is inversely proportional to the diffusivity:

$$\tau \sim \frac{C}{D_S} \tag{3.14}$$

where C is a constant, determined by the vicinal angle of the substrate.

Figure 3.7 (a) and (b) show the RHEED intensity variations during homoepitaxial step flow growth of $SrTiO_3$ at different oxygen deposition pressures and temperatures, using a substrate with vicinal angle of ~2°, corresponding to an average terrace width of ~10 nm. Full intensity recovery is observed in these cases, indicating step flow growth. The characteristic relaxation time[XIII], obtained by a fit using eq. (3.13), versus oxygen deposition pressure for different temperatures is given in figure 3.7 (c). A clear dependence of the relaxation times on the oxygen deposition pressure is observed. The sharp transition observed during 2D growth is, however, not observed at step flow conditions. In figure 3.7 (d), the data is presented in an Arrhenius plot. From the slopes, values for the energy barrier of diffusion E_A of 2.6 ± 0.3, 3.0 ± 0.3 and 3.5 ± 0.3 eV have been derived for oxygen deposition pressure of 3, 12 and 20 Pa, respectively. As expected, these values are larger than the values derived during 2D growth. Still a lower value for E_A is found at the lowest oxygen deposition pressure, which can be attributed to the kinetic energy of the particles arriving at the substrate.

The activation energy E_A for the diffusing particles is expected to be smaller than the estimated values[15]. Due to the high supersaturation in the deposition pulse, nucleation of a high density of 2D clusters does occur, see chapter 2. These clusters are, however, unstable after the deposition pulse and dissociate into mobile particles. The absolute values of E_A are, therefore, related to the dissociation of the clusters as well as the diffusion of the particles.

3.4 Pulsed laser interval deposition

As shown in chapter 2, the possibility to control the growth during PLD using high-pressure RHEED allows for atomic engineering of oxide materials and growth of heterostructures with atomically smooth interfaces. Layer-by-layer growth[XIV] is

---

[XIII] Single deposition pulses are applied and full recovery of the specular RHEED intensity is observed at all investigated conditions given in figure 3.7

[XIV] To obtain atomically smooth film surfaces, a 2D growth mode is essential. It can either be layer-by-layer growth or step flow growth. However, in case of step flow growth, rate control with RHEED is not possible.

a prerequisite: nucleation of each next layer may only occur after the previous layer is completed. Occasionally, the deposition conditions such as the substrate temperature and oxygen pressure can be optimized for true 2D layer-by-layer growth, e.g., homoepitaxy on $SrTiO_3$ (001), see figure 3.2 (a). The relatively high temperature in combination with a low oxygen pressure enhances the diffusivity of the adatoms on the surface. As a result, the probability of nucleation on top of a 2D island is minimized, i.e., the adatoms can migrate to the step edges of the 2D islands and nucleation only takes place on fully completed unit cell layers.

The probability of second layer nucleation, however, increases at lower substrate temperature and/or higher deposition pressure, leading to multilevel growth. This is indicated by the damping of RHEED intensity oscillations. See for example figure 3.8 (a), where $SrTiO_3$ is depositing at a temperature of 800 °C and oxygen pressure of 10 Pa with a continuous pulse repetition rate of 1 Hz.

In general, roughening of the surface is observed during deposition of different kinds of materials, i.e., metals, semiconductors and insulators. Assuming only 2D nucleation, determined by the supersaturation, limited interlayer mass transport results in nucleation on top of 2D islands before completion of a unit cell layer. Still, one can speak of a 2D growth mode. However, nucleation and incorporation of adatoms at step edges is proceeding on an increasing number of unit cell levels, which is seen by damping of the RHEED intensity oscillations.

Several groups[16,17,18] investigated the possibility of growth manipulation by enhancement of the interlayer mass transport. Two different temperatures, two different growth rates or periodic ion bombardment was applied to increase the number of nucleation sites and thus to decrease the average island size. This will enhance the transport of material from an island to a lower level. Usually, for epitaxy of complex oxide materials, the regime of temperatures and pressures is limited by the stability of the desired phases, e.g., $YBa_2Cu_3O_{7-\delta}$ (Y123) can only be grown in a specific temperature and pressure regime[19]. At low temperatures a-axis oriented films are formed whereas at high temperatures the material decomposes. Periodic ion bombardment is very difficult to realize in view of the stoichiometry of oxide materials[20]. Improvement of the interlayer mass transport by applying temperature variations or periodic ion bombardment during growth of complex oxides is, therefore, mostly infeasible. Manipulation of the growth rate, i.e., both the instantaneous and average growth rate, can be used to impose layer-by-layer growth. Here, the unique features of PLD are employed. As discussed in previous chapters, a high density of small 2D nuclei is formed due to the high supersaturation just after the deposition pulse. Subsequently, larger islands are formed through recrystallization in between deposition pulses, exhibited by the typical relaxation of the RHEED intensity of the specular spot during PLD. As a result, the probability of second layer nucleation on the growing islands increases.

Hence, to decrease this probability, coarsening should be avoided. This can be achieved by maintaining the high supersaturation for a longer time by decreasing the time between the deposition pulses. The latter is easily achieved at high repetition rates[XV]. For that reason we introduced a growth method[21], based on a periodic sequence: fast deposition of the amount of material needed to complete one unit cell layer in a short[22,XVI] interval followed by a long interval in which no deposition takes place and the deposit can reorganize by recrystallization. This makes it possible to grow in a unit cell layer-by-layer fashion in a growth regime (temperature, pressure) where otherwise island formation would dominate the growth.

Figure 3.8 (b) shows the RHEED intensity during 10 cycles of $SrTiO_3$ deposition[XVII] (at 10 Hz) and a subsequent period of no deposition, using the same oxygen pressure and substrate temperature as in figure 3.8 (a), following the new approach. In this case the number of pulses needed per unit cell layer was estimated to be 27 pulses. Formation of a multilayer growth front is suppressed, indicated by the small decay of the intensity after each unit cell layer; in figure 3.8 (c) the intensities at each maximum of both methods are compared.

The small decrease of the maximum intensity is ascribed to the fact that only an integer number of pulses can be given to complete one unit cell layer, resulting in small deviations between the deposited and the required amount of material. A higher number of pulses decreases this deviation and is, therefore, favorable. The deposition time for one unit cell layer, however, should be smaller or comparable to the characteristic relaxation time. This is visualized in figure 3.8 (d) where, the intensity change during deposition of one unit cell layer at 10 Hz is shown. The shape of the intensity curve at 10 Hz strongly resembles a parabola when calculating the intensity change of a two-level growth front with randomly distributed islands and island sizes using eq. (3.3).

From the shape of the curve it can be seen that the time needed to deposit one unit cell layer is still too long. This is because the deposition time interval of 2.7 sec. is longer than the characteristic relaxation time (~0.5 sec.). However, a significant suppression of the formation of a multilevel system has already been achieved. This suppression is clearly noticed by comparison of the surface morphologies after deposition using “standard” PLD and the new approach, see

---

[XV] Nowadays, intense UV-lasers are commercially available with pulse repetition rates up to several hundred Hertz.

[XVI] The deposition interval should be in the order of the characteristic relaxation time, typically 0.5 s.

[XVII] An $SrTiO_3$ substrate with a small vicinal angle (<0.2°) was selected for this study to exclude step flow like growth behaviour.

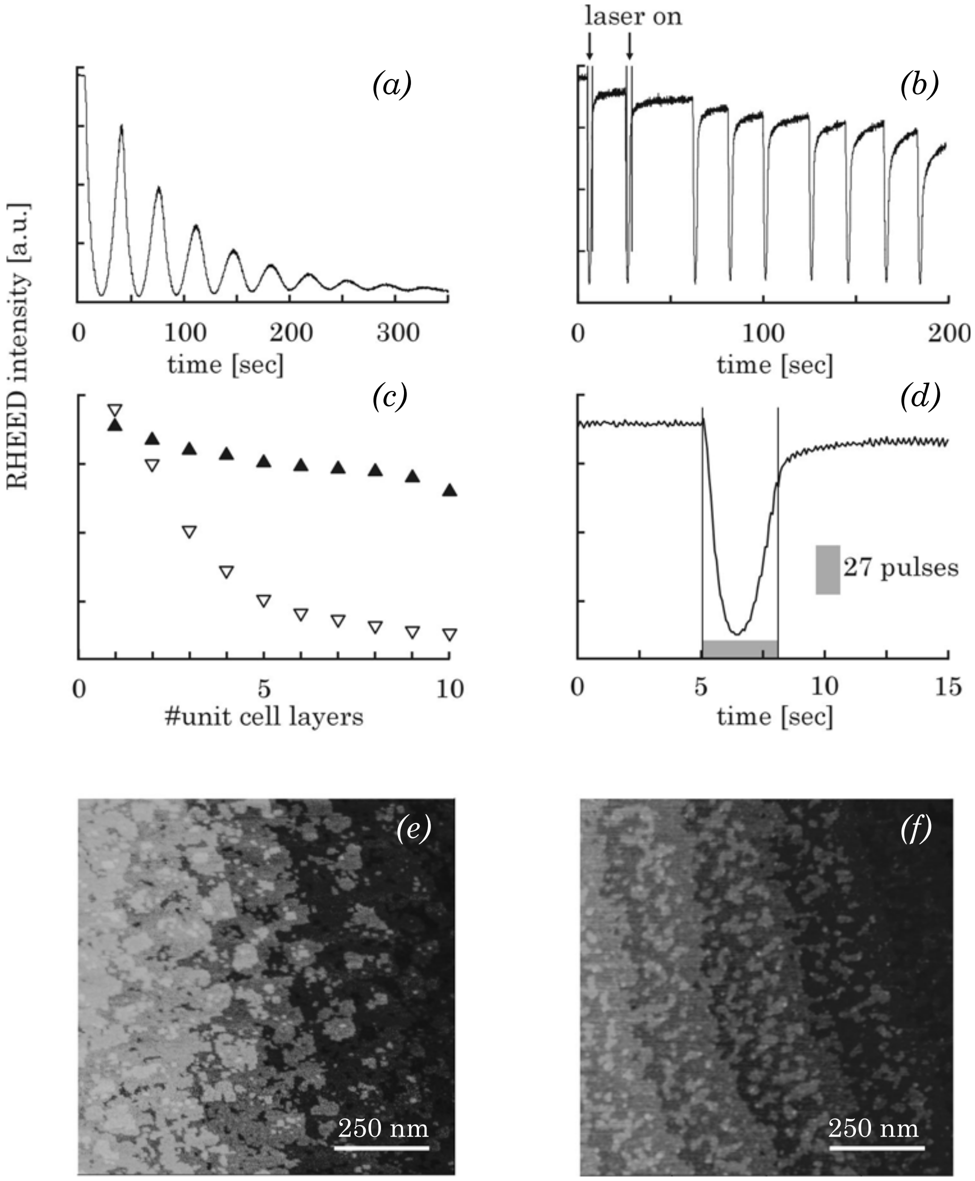

Figure 3.8: Specular RHEED intensity recorded during homoepitaxial growth of $SrTiO_3$ at 10 Pa and 800 °C using "standard" PLD (a) and interval PLD (b). Intensity maxima using "standard" PLD:▽ and interval PLD: ▲ (c). Intensity variation during one deposition interval (d). The surface morphologies of ~30 nm thick $SrTiO_3$ films are depicted in the AFM micrographs: "standard" PLD (e) and interval PLD (f).

figure 3.8 (e) and (f), respectively. At least four levels are observed on the terraces in figure 3.8 (e), compared to only two levels in figure 3.8 (f).

Using the above-presented method[21,23,24] it is possible to impose a single-level 2D growth mode or layer-by-layer growth mode with PLD despite unfavorable deposition conditions for $SrTiO_3$ with respect to mobility. The value of this method is demonstrated in the epitaxial growth of the infinite layer structure

$SrCuO_2$/$BaCuO_2$[8,25], for which the choice of temperature and pressure is more critical, proving the importance of this growth method. The method is also applied in the growth of Y123 by the sub-unit cell layer epitaxy method, as described in chapter 6.

3.5 Conclusions

The growth of complex oxides is far from thermal equilibrium and, therefore, dominated by kinetic processes. High-pressure RHEED is used to extract the energy barrier for diffusion E_A and shows a dependence of E_A on the oxygen deposition pressure attributed to the kinetic energy of the deposited particles. Reliable determination of E_A is feasible at step flow growth conditions. Here, a steady step density causes a constant average travel distance for the diffusing particles. It is shown that this constant distance is essential for the reliable determination of E_A.

It is shown that a single-level 2D growth mode or layer-by-layer growth mode for $SrTiO_3$ can be imposed with PLD despite unfavorable deposition conditions with respect to mobility. Depositing every unit cell layer at a very high deposition rate followed by a relaxation interval, the typical high supersaturation in PLD is extended, keeping the average island size as small as possible. Therefore, the interlayer mass transport is strongly enhanced and the formation of a multi-level growth front does not occur. This technique, which we call Pulsed Laser *Interval* Deposition, is unique for PLD, no other technique has the possibility to combine very high deposition rates with intervals of no deposition in a fast periodic sequence.

References

1 I.V. Markov, *Crystal growth for beginners* (World Scientific, London, 1995), pp. 81-86

2 E. Bauer, *Z. Kristallographie* **110**, 372 (1958)

3 G. Rosenfeld, B. Poelsema and G. Comsa in *Growth and Properties of Ultrathin Epitaxial Layers,* D. A. King and D.P. Woodruff Eds. (Elsevier Science B.V., 1997) chapter 3

4 S. Stoyanov, *Surface Science*, **199**, 226 (1988)

5 S. Stoyanov, M. Michailov, *Surface Science*, **202**, 109 (1988)

6 H. Karl and B. Stritzker, *Phys. Rev. Lett.* **69**, 2939 (1992)

7 V.S. Achutharaman, N. Chandresekhar, O.T. Valls and A.M. Goldman, Phys. Rev. B **50**, 8122 (1994)

8 G. Koster, *Artificially layered oxides by pulsed laser deposition*, PhD thesis ISBN 9036513367, University of Twente The Netherlands, (1999)

9 J.P.A. Van der Wagt, *Reflection High-Energy Electron Diffraction during Molecular-Beam Epitaxy*, PhD thesis, Stanford University USA, (1994)

10 M. Strikovski and J.H. Miller, *Appl. Phys. Lett.* **73**, 1733 (1998)

11 J.H. Neave, P.J. Dobson, B.A. Joyce, J. Zhang, *Appl. Phys. Lett.*, **47**, 100 (1985)

12 T.Shitara, D.D. Vvedensky, M.R. Wilby, J.Zhang, J.H. Neave and B.A. Joyce, *Phys. Rev. B* **46**, 6825 (1992)

13 T. Shitara, J. Zhang, J.H. Neave and B. A. Joyce, *J. Appl. Phys.* **71**, 4299 (1992)

14 H.J.W. Zandvliet, H.B. Elswijk, D. Dijkkamp, E.J. van Loenen and J. Dieleman, *J. Appl. Phys.* **70**, 2614 (1991)

15 M. Lippmaa, N. Nakagawa, M. Kawasaki, S. Ohashi and H. Koinuma, *Appl. Phys. Lett.* **76**, 2439 (2000)

16 G. Rosenfeld, R. Servaty, C. Teichert, B. Poelsema and G. Comsa, *Phys. Rev. Lett.* **71**, 895 (1993)

17 G. Rosenfeld, B. Poelsema and G. Comsa, *J. Cryst. Growth* **151**, 230 (1995)

18 V.A. Markov, O.P. Pchelyakov, L.V. Sokolov, S.I. Stenin ans S. Stoyanov, *Surf. Sci.* **250**, 229 (1991)

19 R.H. Hammond and R. Bormann, *Physica C* **162-164,** 703 (1989)

20 A different approach is the use of surfactants, see for instance J. Vrijmoeth, H.A. van der Vegt, J.A. Meyer, E.Vlieg and R.J. Behm, *Phys. Rev. Lett.* **72**, 3843 (1994). However, a suitable candidate for complex oxides has to our knowledge not yet been found.

21 G. Koster, G. J. H. M. Rijnders, D. H. A. Blank, and H. Rogalla, *Appl. Phys. Lett.* **74**, 3729 (1999)

22 G. Koster, A.J.H.M. Rijnders, D.H.A. Blank, H. Rogalla, *Mater. Res. Soc. Symp. Proceedings* **526,** 33 (1998)

23 G. Rijnders, G. Koster, V. Leca, D. Blank and H. Rogalla, *Appl. Surf. Sci.* **168**, 223 (2000)

24 D.H.A. Blank, G. Koster, G.A.J.H.M. Rijnders, E. van Setten, P. Slycke and H. Rogalla, *J. Cryst. Growth* **211**, 98 (2000)

25 G. Koster, K. Verbist, G. Rijnders, H. Rogalla, G. van Tendeloo and D.H.A. Blank, *Physica C* **353**, 167 (2001)

Chapter 4

Initial growth of $SrRuO_3$

4.1 Introduction

Since the discovery, 40 years ago[1], of ferromagnetism in $SrRuO_3$, many studies have been carried out to determine its structural, magnetic and electronic properties. $SrRuO_3$ shows a metallic temperature dependence of the electrical resistivity. In fact, it is one of the best conducting metallic oxides. Because of its chemical stability, even at temperatures up to 1200 K, it is a useful candidate as electrode material in (all-oxide) electronic devices.

$SrRuO_3$ is paramagnetic at room temperature and ferromagnetic below the Curie temperature of 160 K. It exhibits a strong magneto-crystalline anisotropy in single-domain thin films as well as crystals. Single-domain[2] crystalline $SrRuO_3$ thin films are successfully grown on vicinal $SrTiO_3$ substrates[3,4,5], allowing for studying of intrinsic anisotropic magnetotransport properties[6,7,8]. In these studies, a controlled growth mechanism, by careful selection of the vicinal angle of the substrate, is proposed[9] to obtain a single-domain structure. A recent study[10] showed that the proposed growth mechanism could not be responsible for the single-domain structure. The substrate induced domain formation is, therefore, under debate, since a clear dependence of the domain formation on the vicinal angle of the $SrTiO_3$ substrate was still found.

The above-mentioned studies utilized *ex situ* analysis tools like scanning probe microscopy (SPM) and X-ray diffractrometry (XRD) to determine the surface morphology and domain structure of the $SrRuO_3$ thin film and, subsequently, the growth mechanism.

High-pressure reflection high-energy electron diffraction (RHEED) enables *in situ* study of the influence of the substrate surface morphology, affected by the vicinal angle. In this chapter the initial growth of $SrRuO_3$ on vicinal $SrTiO_3$ substrates will be discussed, focussing on the growth mechanism and terminating atomic layer of $SrRuO_3$.

4.2 Structural properties of $SrRuO_3$

Like many ABO_3 perovskite compounds, $SrRuO_3$ exhibits an orthorhombic symmetry at room temperature, see figure 4.1. It has a distorted, perovskite structure with lattice parameters a=5.5670, b=5.5304, and c=7.8446 Å. The degree of this distortion can be described by tilting of the RuO_6 octahedra. An orthorhombic cell is typically observed when the A-O bond length is less than √2 times the B-O length, which results in rotations of the BO_6 octahedra. With increasing temperature the degree of the orthorhombic distortion decreases, and the structure transforms to other perovskite structures.

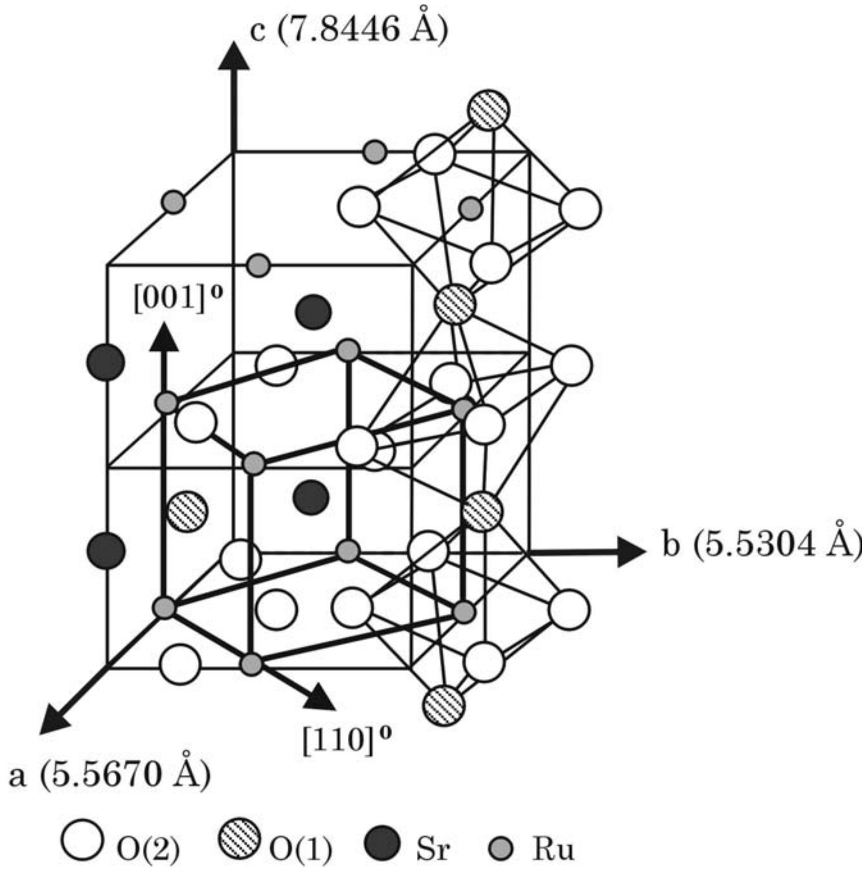

Figure 4.1: Schematic view of the orthorhombic unit cell of $SrRuO_3$.

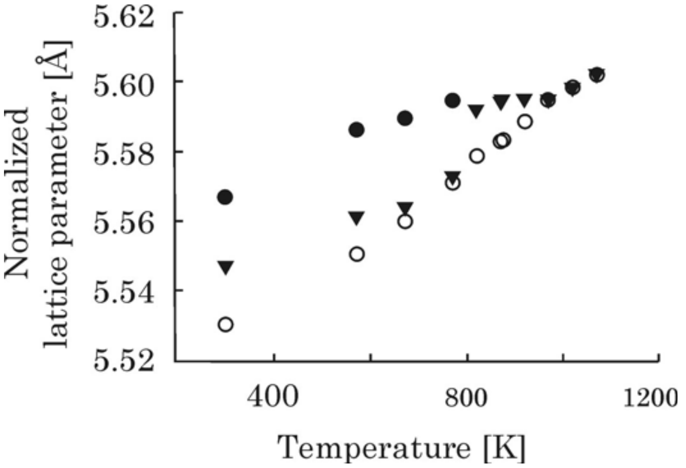

Figure 4.2: Normalized lattice parameter of powder SrRuO$_3$ as function of temperature. (●): a-lattice parameter, (▼): b-lattice parameter and (○): c-lattice parameter. Data taken from ref [13].

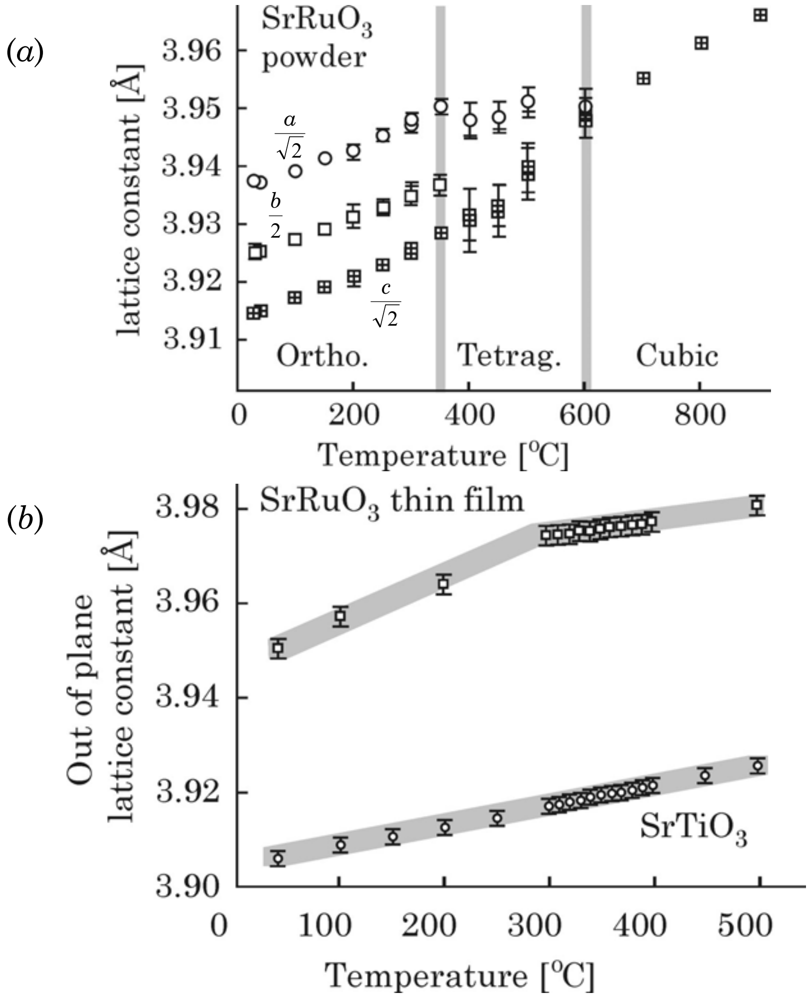

Figure 4.3: Lattice constant of powder SrRuO$_3$ (a) and out-of-plane lattice constant for a SrRuO$_3$ film deposited on SrTiO$_3$ (b) versus temperature. Data taken from ref [10], the parameters given correspond to the pseudo-cubic unit cell.

4.2.1 Structural properties of bulk $SrRuO_3$

High-resolution powder neutron diffraction studies[11,12] have demonstrated $SrRuO_3$ to be isostructural with $GdFeO_4$. A transition[13] is observed from the orthorhombic phase, found at room temperature, to a tetragonal phase at 550 °C, see figure 4.2. This tetragonal phase persists until approximately 680 °C. At this temperature a transition to the standard cubic perovskite structure is observed. Recent powder x-ray diffraction experiments[10], however, show a transition from the orthorhombic to the tetragonal phase at significantly lower temperature, i.e., 350 °C, as shown in figure 4.3 (a).

4.2.2 Structural properties of thin film $SrRuO_3$

As mentioned before, $SrRuO_3$ has an orthorhombic structure at room temperature. A pseudo-cubic perovskite structure, however, can be constructed with lattice parameter very close to the lattice parameter of the cubic perovskite $SrTiO_3$ (a=3.905 Å). The lattice mismatch at room temperature is approximately 0.64 %. Various studies have shown that untwinned, single-crystalline thin films can be grown on vicinal $SrTiO_3$ using sputter deposition[3,8,9,14], molecular beam epitaxy[17], reactive electron beam evaporation[5] and pulsed laser deposition[4].

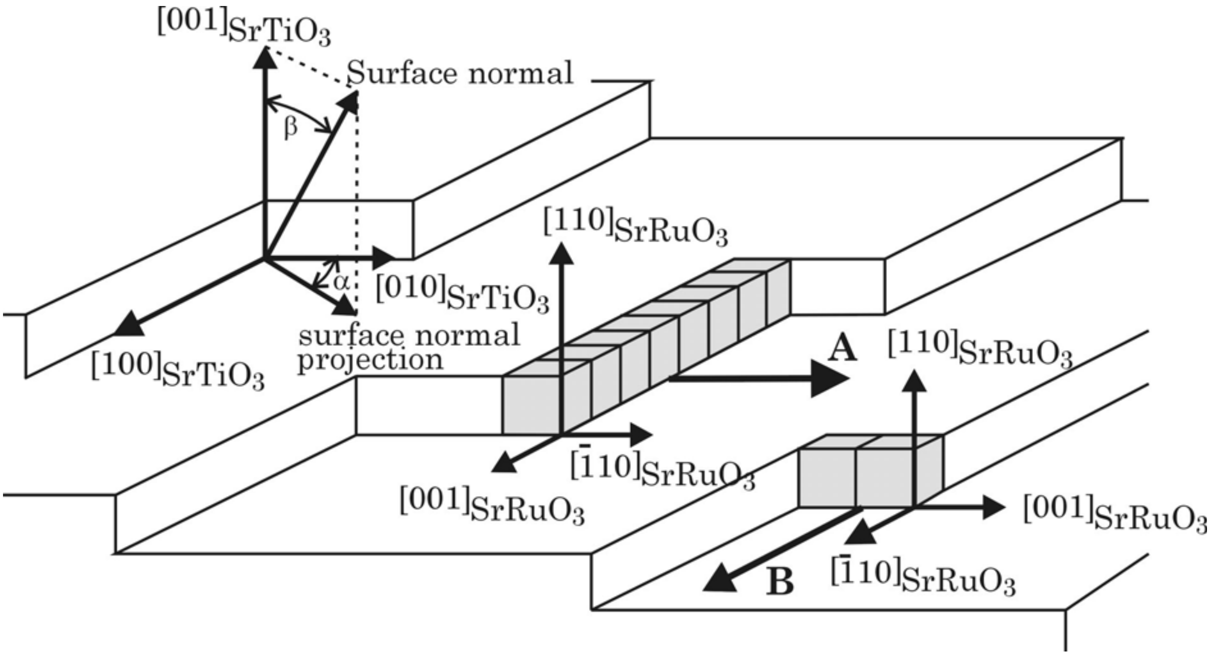

Figure 4.4: Schematic view of a vicinal substrate. The vicinal angle is represented by α *and* β*, respectively. Two epitaxial step flow type growth directions, A and B, are shown. For simplicity only the pseudo-cubic unit cell is drawn. For* $SrRuO_3$*, the orthorhombic frame was used to refer to the crystalline directions. Picture taken from [9].*

The effect of the vicinal angle (determined by α and β, see figure 4.4) of (001) $SrTiO_3$ substrates on the in-plane epitaxial arrangement of $SrRuO_3$ has been clarified by Gan *et al.*[9]. It is shown that, using substrates with large vicinal angle (β>1.9°) with α close towards the [010] axis, single-domain $SrRuO_3$ with good crystalline quality can be grown. The fourfold symmetry of $SrTiO_3$ (001) is broken by exposing both the (010) and (100) planes at the surface steps, as shown in figure 4.4. Two in-plane epitaxial arrangements are possible depending on the direction of step flow: $SrRuO_3$[001]//$SrTiO_3$[100] and $SrRuO_3$[$\bar{1}$10]//$SrTiO_3$[010], or $SrRuO_3$ [001]//$SrTiO_3$ [010] and $SrRuO_3$ [$\bar{1}$10]//$SrTiO_3$ [100], which are marked by "A" and "B," respectively, as shown in figure 4.4. By alignment of the substrate steps with respect to the $SrTiO_3$ crystal axes, step flow in one direction occurs resulting in single-domain thin films. Step flow growth, with the orthorhombic unit cell as the smallest growth unit, and no 2D nucleation on terraces are a prerequisite in the proposed model.

From high-temperature x-ray experiments, however, it is concluded[10] that thin film $SrRuO_3$ is in the cubic phase during deposition at temperatures above 600 °C. That is, the cubic unit cell is expected to be the smallest growth unit at deposition conditions. Only at relatively low temperatures (below 350 °C) $SrRuO_3$ is in the orthorhombic phase. As a result, step flow growth of $SrRuO_3$ cannot provide the untwinned orthorhombic texture. Still, there is a clear dependence on the domain formation in $SrRuO_3$ and the alignment of the substrate steps[9]. Therefore, it is expected that the surface morphology of the substrate plays an important role in domain formation. J-P Maria *et al.*[10] proposed that the $SrRuO_3$/$SrTiO_3$ interface characteristics at both the terraces as well as the step ledges are responsible for the untwinned symmetry. The asymmetric interfacial strains, due to thermal expansion and lattice constant mismatch provided by the vicinal substrate on the cubic $SrRuO_3$ cell, are believed to be responsible for the alignment of the orthorhombic symmetry upon cooling. The transition to the orthorhombic symmetry involves a tilting of the oxygen octahedra and an angular distortion of the unit cell. They postulated that a combination of the asymmetric thermal expansion and epitaxial stresses applied to those unit cells located at the step corners result in a preferential alignment of the rotation axis. This preferential orientation is propagated through the remainder of the film upon cooling.

4.3 Growth studies of $SrRuO_3$ on $SrTiO_3$

Using high-pressure RHEED, the growth of $SrRuO_3$ has been studied *in situ* on $SrTiO_3$ substrates with single TiO_2 termination. The main objective is to determine the growth mode on vicinal substrates with well-defined surface morphologies.

4.3.1 Growth conditions

To obtain epitaxial growth of $SrRuO_3$, stoichiometric deposition is essential. Both the energy density at the target and the deposition pressure affect the stoichiometric deposition and were optimized. An optimum energy density of 2.5 J/cm^2 (spotsize=2.6 mm^2, pulse energy= 65 mJ) on the $SrRuO_3$ target[I] was determined to obtain stoichiometric ablation[II]. The deposition pressure was set to 13 Pa of oxygen. At this pressure the visible plasma was smaller than the target-to-substrate distance (d_{TS}) of 58 mm, resulting in deposition of thermalized particles. A substrate temperature of 600 °C and a pulse repetition rate of 2 Hz resulted in an average deposition rate of approximately 140 nm/h (0.2Å/pulse).

Using these deposition conditions, typical values for the resistivity ρ of ~200-300 $\mu\Omega$cm was found at room temperature with a residual resistivity ratio RRR ($R_{300K}/R_{4.2K}$) of ~2-4. These values are typical for $SrRuO_3$ films made by PLD[15,16] and sputter deposition[14], whereas higher values of RRR have been found in films made by molecular beam epitaxy (MBE) using an atomic oxygen source[17]. The impingement of high-energetic particles[18] and non-stoichiometric transfer from target to substrate can be responsible for the lower RRR values found in PLD. Stoichiometric transfer of thermalized particles is expected in the depositions described in this work and can, therefore, not be responsible for the relatively low RRR value. The oxidation power of atomic oxygen used in MBE was found to be important for the oxygenation of $SrRuO_3$[17]. Although the oxidation power of molecular oxygen in PLD is sufficiently high to stabilize the $SrRuO_3$ structure, lower degree of oxidation can be expected, which could affect the RRR values of the as-deposited films.

The Curie temperature of the $SrRuO_3$ films was ~150 K, which is slightly less than the value of ~160 K obtained in bulk single crystals. It is believed that the reduction of the Curie temperature originates from the elastic strain in the coherently grown $SrRuO_3$ film. Due to the small lattice mismatch with $SrTiO_3$ the epitaxial films are subjected to a compressive strain in the plane[14].

Figure 4.5 shows typical XRD ϕ-scans of an $SrRuO_3$ film deposited on a vicinal (0.2°) $SrTiO_3$ substrate. Here, a single-domain structure, indicated by the two-fold symmetry, with in-phase epitaxial orientation relationship of $SrRuO_3[001]//SrTiO_3[100]$ and $SrRuO_3\ [\bar{1}10]//SrTiO_3[010]$ was found[III].

[I] A sintered pellet of stoichiometric $SrRuO_3$ was used as target.

[II] The optimum energy density is determined by studying the ablated area with scanning electron microscopy. Stoichiometric ablation is expected at energy densities producing flat surfaces at the irradiated area.

[III] The orthorhombic frame was used to refer to the crystalline directions.

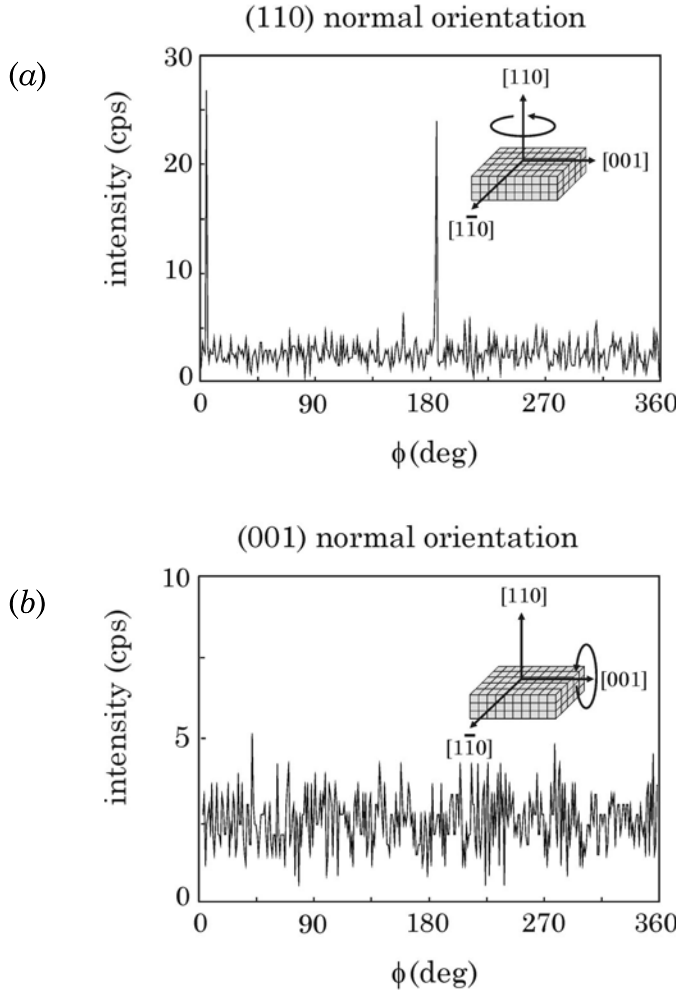

Figure 4.5: Typical XRD ϕ-scans indicating a single-domain structure of $SrRuO_3$ *on vicinal (0.2°)* $SrTiO_3$*. The two-fold symmetry in (a) and the absence of peaks in (b) indicate the single-domain structure.*

Using the PLD conditions mentioned above, perfect single-crystalline $SrRuO_3$ films can be reproducibly obtained on TiO_2 terminated vicinal (0.1°-0.5°) $SrTiO_3$ substrates.

4.3.2 Initial growth studies using AFM and RHEED.

The AFM micrograph, depicted in figure 4.6 (a), of an $SrRuO_3$ film, deposited on TiO_2 terminated vicinal (0.2°) $SrTiO_3$ substrate using the conditions given in 4.3.1, shows a clear step-terrace structure. The surface morphology of the substrate can still be seen. The step heights, determined from AFM cross-section analysis, are approximately 4 Å. Clear finite thickness fringes are observed in x-ray diffraction measurements, see figure 4.6 (b), indicating a smooth surface. From these fringes a film thickness of 50 nm was deduced, which indeed corresponds to a deposition rate of 0.2 Å/pulse.

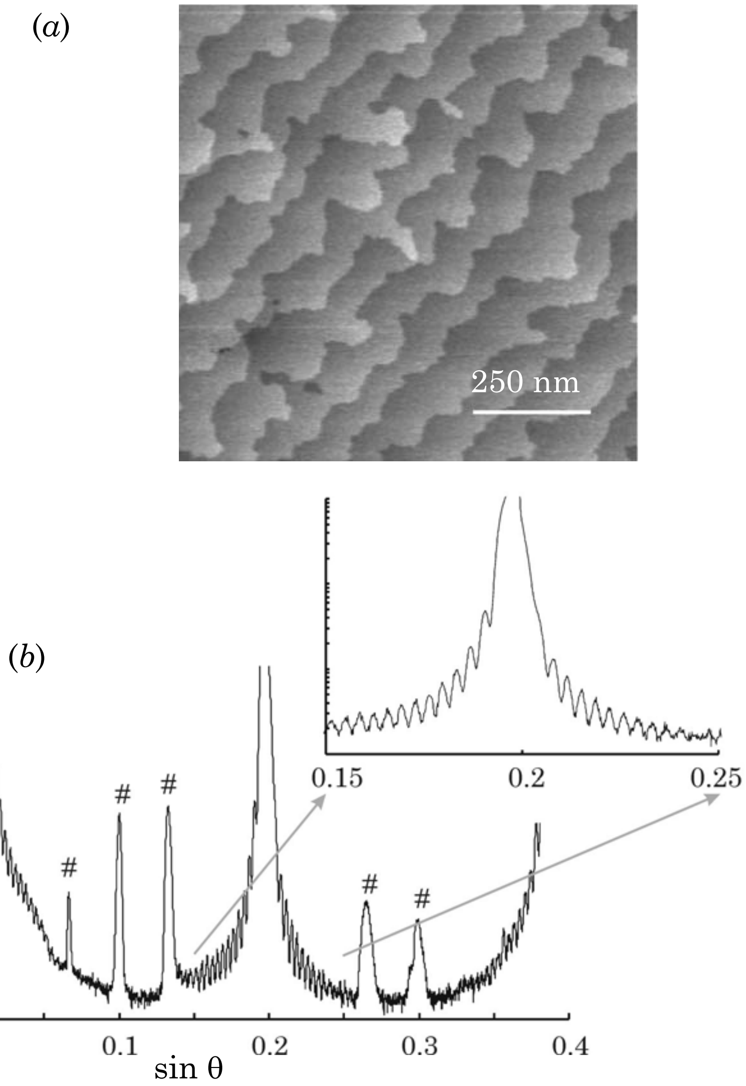

Figure 4.6: Typical AFM micrograph of a 50 nm thick $SrRuO_3$ film (a). XRD measurement show clear finite thickness fringes in the θ-2θ *scan (b). Spectral contributions ($\lambda/2$ and $\lambda/3$) are indicated with a cross.*

The intensity of the specular RHEED spot (20 keV, ~1° incidence angle, ~10° azimuthal angle[IV]) as recorded during growth is shown in figure 4.7. Clearly, the initial growth, i.e., deposition of the first unit cell layer, is characterized by 2-dimensional (2D) nucleation and growth, as shown by the cusp-like intensity variations[V]. After deposition of approximately 4 unit cell layers the intensity oscillations are damped and the average RHEED intensity stays constant during subsequent deposition.

[IV] An off-azimuthal angle was used to avoid interference between the diffracted beams. This is the so-called one-beam condition.

[V] See chapter 3 for a detailed description.

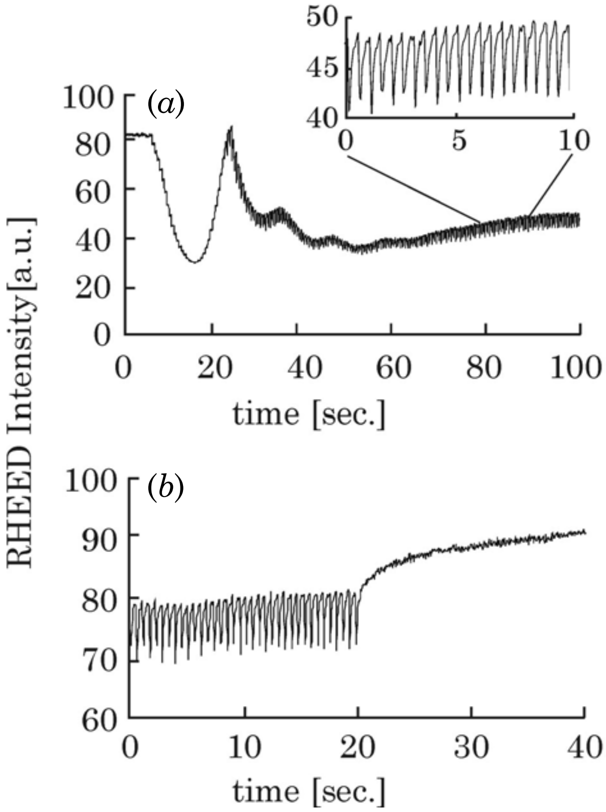

Figure 4.7: RHEED intensity recorded during growth of 50 nm $SrRuO_3$ on TiO_2 terminated $SrTiO_3$ at 600 °C; at initial growth (a), at end of growth (b). The inset of (a) shows an enlargement of the RHEED intensity.

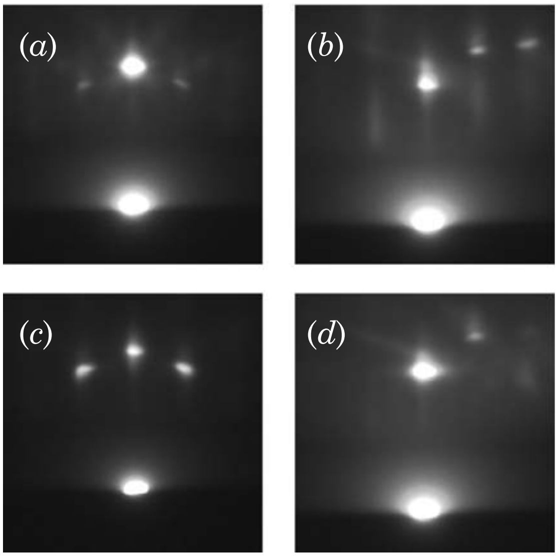

Figure 4.8: RHEED patterns recorded before (a) and (b), and after (c) and (d) deposition of $SrRuO_3$. The azimuthal angle was set to 0° in (a) and (c) and 10° in (b) and (d).

The absence of oscillations indicates an increased roughness due to three-dimensional (3D) growth or a step flow growth mode. The first is not evident because of the high RHEED intensity, whereas the latter assumption is indeed supported by AFM data, see figure 4.6. In this regime, only intensity variations due to the pulsed deposition are visible, see inset in figure 4.7 (a). This feature of the RHEED intensity suggests the occurrence of step flow growth. Because of the pulsed laser, the deposition is discontinuous, resulting in a modulated RHEED intensity. During the deposition pulse a very fast deposition takes place followed by a rearrangement (*relocation*) of the deposit[VI]. This manifests as a relaxation-like behavior of the RHEED intensity. The amplitude and time constant of the RHEED intensity relaxation increase if step flow growth is dominating because of an increased diffusion length and a flat film surface.

The RHEED intensity variations, as recorded during initial growth of $SrRuO_3$ on $SrTiO_3$, clearly show a transition from growth by the formation and coalescence of 2-dimensial islands to growth by step advancement[19]. When the deposition is stopped, the RHEED intensity increases due to the decrease in the density of diffusing particles[VII], see figure 4.7 (b). Furthermore, smoothing of the step edges is expected after deposition, leading to a further increase of the RHEED intensity. The RHEED patterns before and after deposition at an azimuthal angle of 10° and 0° are shown in figure 4.8. Clear dots are observed, indicating an atomically smooth surface.

To verify step flow, experiments were carried out with different vicinal substrates. The RHEED intensity of the specular spot monitored during deposition of $SrRuO_3$ on vicinal, TiO_2 terminated $SrTiO_3$ substrates, with a vicinal angle of 0.36°, 0.22°, and 0.11°, respectively, is shown in figure 4.9. As can be seen from the number of intensity oscillations, the vicinal angle has a large influence on the transition to step flow growth. The number of RHEED oscillations increases with increasing terrace length. In all cases the final growth mode is step flow like: no oscillations of the RHEED intensity are observed. Since, apart from the terrace length, all other deposition parameters are kept constant, it is expected that the diffusion length and ripening effects are identical.

Because only one oscillation is observed with the highest vicinal angle, the migration length of the deposited $SrRuO_3$ is expected to be, at least comparable to the terrace width (65 nm). For smaller vicinal angles, the probability of nucleation on the terraces is increased. As a result, islands are formed, indicated by the RHEED intensity oscillations. Coalescence of these islands with the advancing

---

[VI] See chapter 2 for a detailed description.

[VII] The long relaxation behaviour after deposition is also related to the decrease of the step density due to the coalescence of mobile islands with the step edges.

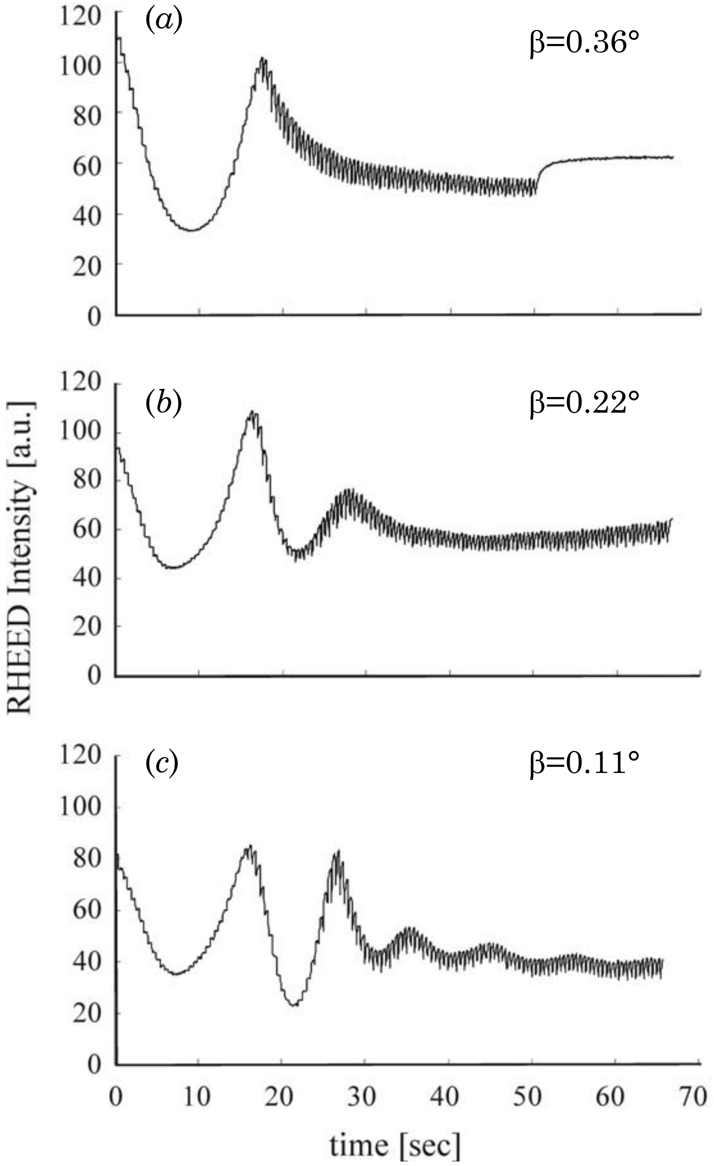

Figure 4.9: RHEED intensity of specular spot recorded during growth of $SrRuO_3$ on vicinal TiO_2 terminated $SrTiO_3$ substrates: 0.36° (a), 0.22° (b) and 0.11° (c).

steps will lead to rough step edges. This process, i.e., formation of islands between the flowing steps and the coalescence of the islands with the flowing steps, will take place continuously resulting in a constant step density and, therefore, a steady RHEED intensity.

In the AFM micrographs in figure 4.10 this steady state can be seen; the average distance between the step edges of both islands and terraces on substrates with small vicinal angle becomes of the same order as on substrates with high vicinal angles. Note that the observed growth mode cannot be described by “pure” step flow growth since nucleation on the terraces takes place. The advancing steps

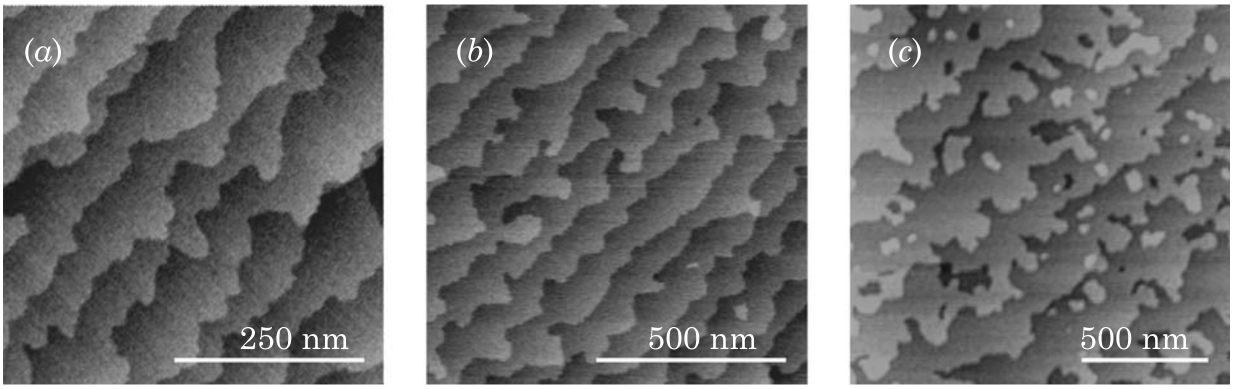

Figure 4.10: AFM micrographs of 50 nm thick $SrRuO_3$ films on vicinal TiO_2 terminated $SrTiO_3$ substrates: 0.34° (a), 0.25° (b) and 0.10° (c).

engulf islands growing on the terraces. Although this growth behavior has been mentioned in literature before[20], this is the first time it is observed in a complex system like $SrRuO_3$.

The number of pulses at the first RHEED intensity maximum is approximately 34 and independent of the vicinal angles used, see figure 4.9. This number is much larger than the number of pulses needed to complete one unit cell layer. A deposition rate of 0.2 Å/pulse, mentioned before, would lead to ~20 pulses necessary for deposition of one unit cell layer.

To elucidate this discrepancy, depositions at different substrate temperatures have been performed. The specular RHEED intensity, recorded during growth at 500, 600 and 700 °C, is shown in figure 4.11. The number of pulses at the first RHEED intensity maximum depends strongly on the deposition temperature. At 700 °C, the number of pulses is almost equal to the number of pulses needed to deposit two unit cell layers (as can be seen from the dashed lines in figure 4.11). The shape of the first RHEED oscillation is asymmetric. A minimum of the intensity is reached after approximately 27 pulses, equivalent to approximately 1.5 unit cell layers.

Figure 4.12 (a) shows an AFM micrograph of an $SrRuO_3$ film deposited at 700 °C, interrupting the growth at this minimum. Many small islands can be observed. The height of these islands is determined to be approximately 4 Å (~ c-lattice parameter of the pseudo-cubic cell). During subsequent growth, coalescence of the islands occurs until an almost closed layer is obtained, see figure 4.12 (b). Here, the growth is interrupted at the first RHEED intensity maximum after 37 pulses, equivalent to the deposition of approximately 2 unit cell layers.

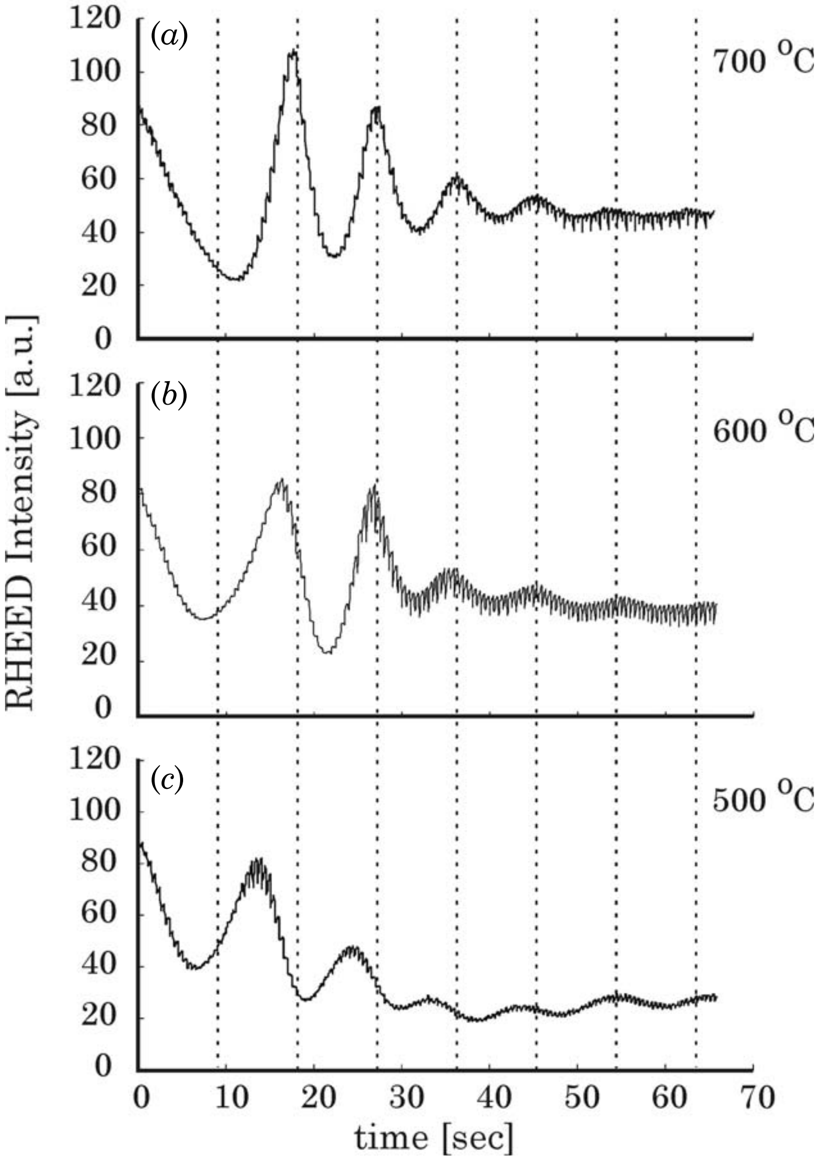

Figure 4.11: RHEED intensity of specular spot recorded during growth of $SrRuO_3$ on TiO_2 terminated $SrTiO_3$ using a deposition temperature of 700 °C (a), 600 °C (b), and 500 °C (c). The vicinal angle β was 0.11°. The distance between the dashed lines correspond to the time necessary for deposition of one pseudo-cubic unit cell layer at 700 °C.

Discussion

From the RHEED and AFM data the following conclusions can be made:

(1) At 700 °C, the first RHEED minimum is observed after deposition of the material needed for approximately 1.5 unit cell layers, whereas the first RHEED maximum is observed after deposition of the material needed for approximately 2 unit cell layers.

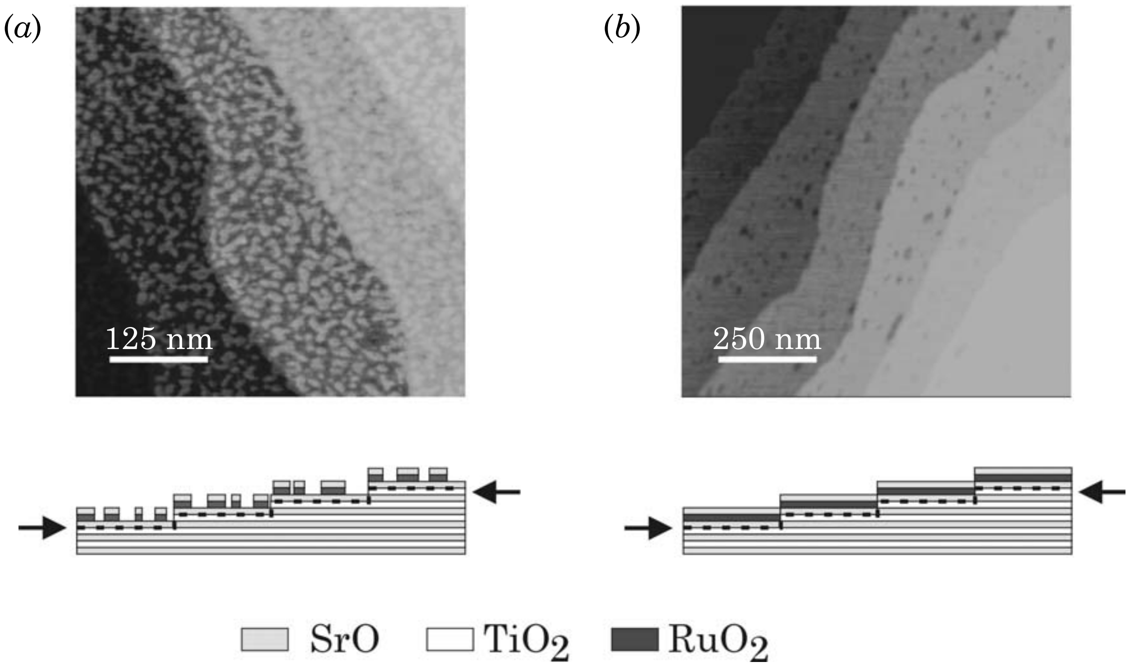

Figure 4.12: AFM micrographs of $SrRuO_3$ deposited on TiO_2 terminated $SrTiO_3$ at a deposition temperature of 700 °C and schematic cross-section views. The number of pulses applied is 27, corresponding to the first HEED minimum (a) and 40, corresponding to the first RHEED maximum (b), respectively. The arrows indicate the $SrTiO_3$-$SrRuO_3$ interface.

(2) The position of the minimum and the maximum RHEED intensity depend on the growth temperature.
(3) AFM micrographs taken after interrupting the growth at 700 °C at the first RHEED minimum show islands only about 4 Å high. Step heights comparable to 1.5 unit cell have never been observed.

Combining the experimental results, the following initial growth behavior is proposed, visualized in figure 4.12:

(1) During growth of $SrRuO_3$, no RuO_2 termination will occur, i.e., SrO is the termination atomic layer.
(2) At 700 °C, after deposition of the equivalent of 2 unit cell layers, a closed layer of $SrRuO_3$ with SrO termination is observed, see figure 4.12 (b).
(3) After completion of this $SrRuO_3$ unit cell layer, subsequent stoichiometric deposition leads to unit cell layer-by-layer growth, indicated by the equidistant RHEED intensity oscillations after the first maximum, see figure 4.11 (a).
(4) Depending on the average terrace length, the growth mode converts to a steady state growth mode, see figure 4.9 and 4.10.

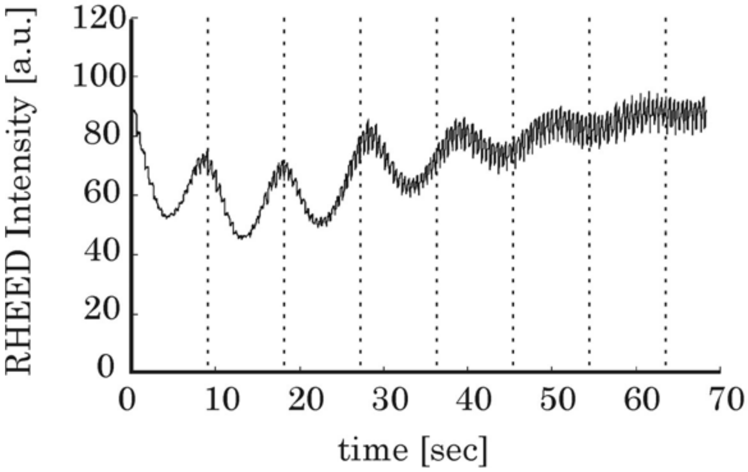

Figure 4.13: RHEED intensity of specular spot recorded during growth of $SrRuO_3$ *on SrO terminated* $SrTiO_3$ *using a deposition temperature of 600 °C. The distance between the dashed lines is the same as in figure 4.11.*

As a consequence of this proposed behavior, a termination conversion has to occur from B-site (TiO_2 terminated $SrTiO_3$) to A-site (SrO terminated $SrRuO_3$) during deposition of the first unit cell layers. Preserving perovskite stacking one should expect a RuO_2 termination after stoichiometric deposition of the first unit cell layer, accompanying a maximum in the RHEED intensity. Since this maximum was never observed, we conclude that RuO_2 termination is not stable at these deposition conditions. During the deposition of the first unit cell layer, $SrRuO_3$ decomposes to SrO and the highly volatile Ru_xO_y. As a result, the latter evaporates from the surface leaving SrO as the terminating surface layer. This decomposition stops after the terminating layer is completely converted from TiO_2 to SrO. A schematic view of the expected cross-section at both RHEED maximum and minimum is sketched in figure 4.12.

The desorption of RuO_2 is most likely due to the relatively low oxidation power at the PLD conditions used. At these conditions, the RuO_2 terminating layer cannot be stabilized leading to the formation of Ru_xO_y. Among the Ru oxides only RuO_2 is found to be stable[21], while other forms, e.g., Ru_2O, are volatile[VIII,22]. The temperature has a large influence on the evaporation of the Ru_xO_y[23], causing the distributed transition in the oscillation period, observed at lower temperatures, see figure 4.11.

[VIII] Deposition of pure RuO_2 from a stoichiometric target did not result in a measurable deposition rate at the mentioned deposition conditions of $SrRuO_3$. Many groups have proposed RuO_2 as a metallic like conducting oxide for use as electrode material. Using deposition techniques like sputter deposition and PLD the deposition temperature is limited to 600-700 °C. Higher temperatures leads to re-evaporation of the deposited material.

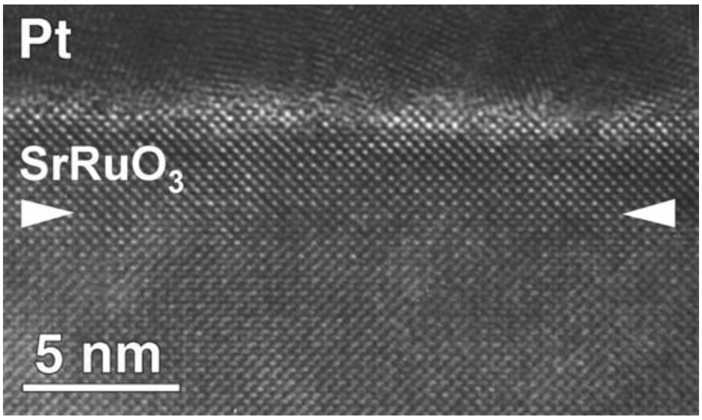

Figure 4.14: Cross-section electron micrograph of ~7 unit cell thick $SrRuO_3$*, deposited on* TiO_2 *terminated* $SrTiO_3$*. A Pt layer is used as protection layer. The arrowheads indicate the interface between substrate and film, determined from the deposited layer thickness of 7 unit cell layers.*

To verify the above proposed termination conversion, deposition was performed on SrO terminated[IX] $SrTiO_3$ substrates. From figure 4.13 it can be seen that the first maximum of the RHEED oscillation is indeed completed after deposition of one unit cell layer. Here, the termination conversion and the accompanying evaporation of Ru_xO_y at the initial growth stage of $SrRuO_3$ do not occur.

To verify the perovskite stacking sequence at the substrate-film interface, high-resolution electron microscopy (HREM) was performed. Figure 4.14 shows a cross-section overview of a ~7 unit cell[X] thick $SrRuO_3$ layer deposited on TiO_2 terminated $SrTiO_3$. On top of the $SrRuO_3$ layer a thin Pt layer was deposited. No interface dislocations appear in this overview. The interface between film and substrate is atomically flat and no amorphous or secondary phases were observed. The unit cells are clearly visible and the epitaxy is perfect all over the film with a perovskite stacking sequence at the substrate-film interface. Unfortunately, the interface between $SrRuO_3$ and Pt deteriorated, probably during HREM sample preparation and, thus, determination of the terminating atomic layer was not possible.

[IX] To obtain this termination a monolayer of SrO was deposited on TiO_2 terminated $SrTiO_3$ prior to the deposition of $SrRuO_3$.

[X] Here, we refer to the pseudo-cubic unit cell.

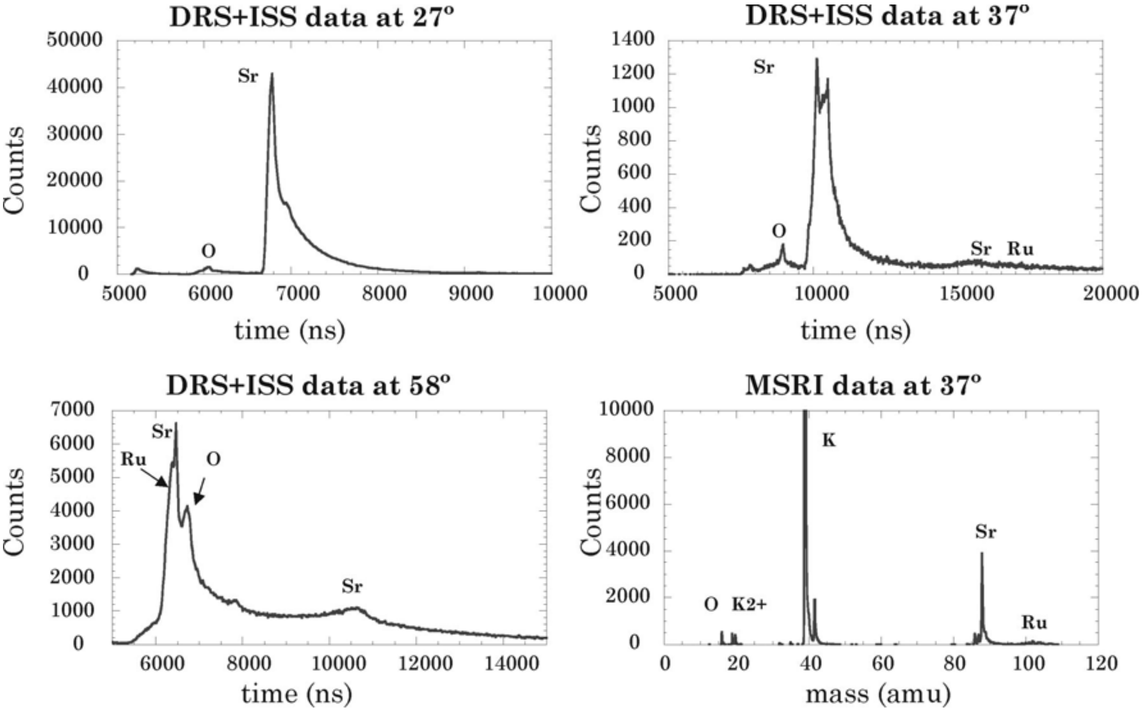

Figure 4.15: Ex situ TOF ISARS spectra of $SrRuO_3$ film collected at [100] direction at different incident angles. The spectra show clear Sr peaks whereas relative small Ru peaks are observed.

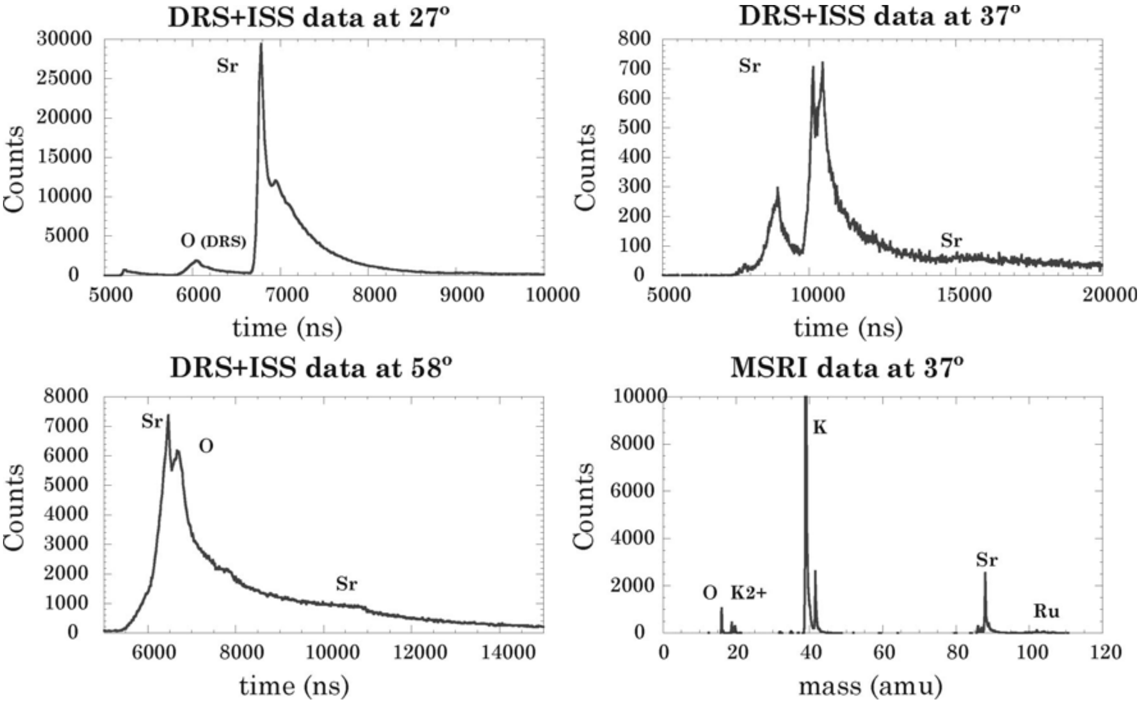

Figure 4.16: Ex situ TOF ISARS spectra of $SrRuO_3$ film collected at [110] direction.

Using *ex situ* ion scattering spectroscopy (TOF-ISARS[XI]), the topmost atomic layer was determined. TOF-ISARS combines several ion spectroscopy techniques with very high surface sensitivity. Ion scattering[XII] spectroscopy (ISS) and direct recoil spectroscopy (DRS) provide both chemical and structural information. Mass spectroscopy of recoiled ions (MSRI) is similar to secondary ion mass spectroscopy (SIMS) but capable of high-resolution surface analysis at higher ambient pressures, making it well suited for realtime, *in situ* analysis of film growth processes.

Figure 4.15 and 4.16 show ISS and DRS spectra at different incident angles of the ion beam and MSRI spectra of a 50 nm thick $SrRuO_3$ film. Measurements were performed *ex situ* at two different orientations, i.e., [100] and [110], using the pseudo-cubic frame as reference. To clean the surface, the film was heated to 450 °C in vacuum[XIII]. MSRI indicates mostly Sr and O while small amounts of Ru have been observed. The most prominent peak shown in ISS and DRS is SrO[24], supporting the termination conversion mentioned above[XIV].

4.4 Determination of the energy barrier for diffusion

From RHEED measurements it is concluded that the diffusivity, parameterized by the activation energy for diffusion E_A, is enhanced after the termination conversion from TiO_2 to SrO. It is shown that the termination conversion depends on the growth temperature. At 700 ºC the conversion is completed during growth of the first unit cell layer whereas at lower temperatures the conversion is distributed throughout the growth of more unit cell layers. The nucleation density is expected to change during the termination conversion. Reliable determination of the activation energy for diffusion E_A from recovery RHEED data during the termination conversion is, therefore, not possible. After the conversion is complete, however, E_A can be determined from RHEED intensity recovery data, using the method presented in section 3.3.2.2. In this method, the fixed step density during step flow growth is utilized and, by monitoring the recovery of the specular reflected RHEED intensity after a deposition pulse, the decay of the adatom

---

[XI] TOF-ISARS is an acronym for Time-of-Flight Ion-Scattering and Recoil Spectroscopy Analysis. Measurements were performed at OXXEL GmbH, Bremen, Germany.

[XII] Here, K-ions are used.

[XIII] The ISS and DRS spectra measured at room temperature only showed O, H and C on the surface.

[XIV] These measurements were performed *ex situ*. Thermal treatment at moderate temperature was necessary to clean the surface. Although modification of the surface is not expected, it can not be excluded.

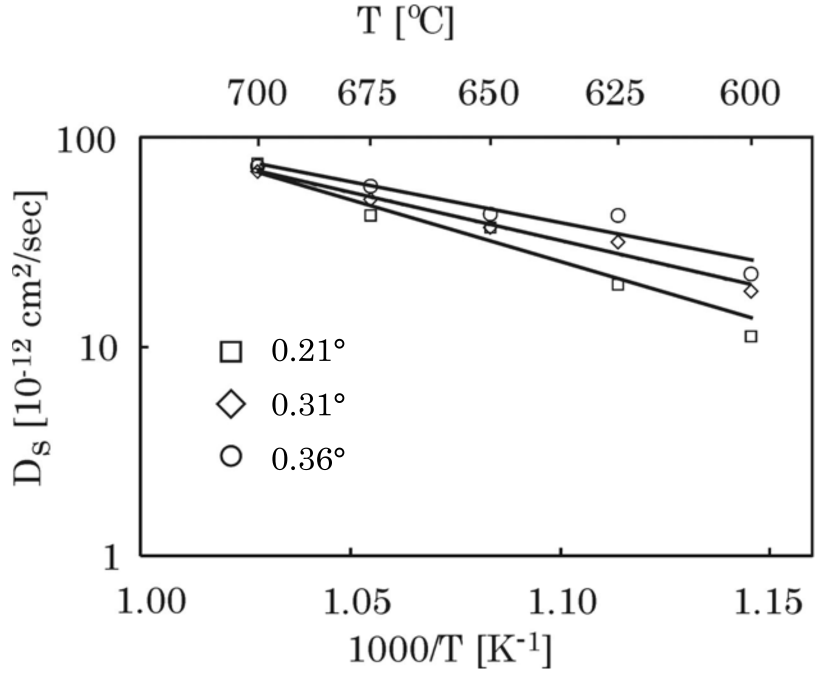

Figure 4.17: The diffusivity, estimated from the recovery time of RHEED intensity using eq. (4.1), for different vicinal angles and temperature in the Arrhenius form.

density on the terraces is monitored. From the temperature dependent decay time the activation energy for diffusion E_A could be determined.

Zhu[25] proposed a method to determine the diffusivity at epitaxial step flow conditions[XV]. Here, from the terrace width l_T and the decay time of the adatom density on the terraces, the diffusivity is given by:

$$D_S \sim \frac{4 l_T^2}{\pi^2 \tau} \tag{4.1}$$

where the characteristic decay time τ is determined from the recovery of the RHEED intensity after interrupting the deposition.

Figure 4.17 shows the diffusivity D_S for SrRuO$_3$ on SrO terminated SrRuO$_3$ versus the inverse temperature for 3 different vicinal angles, i.e., 0.21, 0.31 and 0.36°, and, therefore, 3 different mean terrace widths, i.e., 110, 74, and 64 nm, respectively. Before measurement of the RHEED intensity recovery a few unit cell layers of SrRuO$_3$ were deposited to obtain SrO termination. After deposition, the

---

[XV] Additionally, the step edge sticking probability S_S and the step edge energy barrier E_S can be extracted. The terrace width distribution, however, should be narrow to maintain a characteristic length scale for the terrace width. When the distribution becomes too wide, both, S_S and E_S cannot be determined reliably.

average terrace width is still comparable to the terrace width calculated from the vicinal angle. No step bunching is observed at the highest vicinal angle. At the lowest vicinal angle of 0.21° used in this study no islands have been observed on the terraces after deposition. In both cases, however, the step ledges were roughened, resulting in an increased terrace width distribution. A clear dependence of the vicinal angle on the RHEED intensity recovery time is observed and the diffusivity can, therefore, be determined using eq. (4.1). Recovery measurements were performed using single deposition pulses at different temperatures. The amount of deposited material is estimated to be ~0.05 unit cell layer with every pulse. Only when full recovery of the RHEED intensity is reached after every applied pulse, the growth is assumed to be step flow. If, after deposition, no full recovery is obtained, nucleation on the terrace is assumed and the data point is not used. From the slopes in figure 4.17 the activation energy E_A for diffusion can be extracted using eq. (3.2). Here, a value for E_A of 1.0 ± 0.2 eV is determined.

4.5 Monte Carlo simulations

From the growth studies of $SrRuO_3$ on vicinal $SrTiO_3$ we concluded that, after the termination conversion, the step density changes from the initial step density, determined by the vicinal angle of the substrate, to a steady step density. As a result, the RHEED oscillations, due to 2D nucleation and growth, are damped and a steady RHEED intensity is observed. The transition depends on the vicinal angle of the substrate, while the steady step density is almost independent of the vicinal angle, see figure 4.9 and 4.10. To elucidate this growth behavior we utilized the solid-on-solid (SOS) model introduced by Weeks and Gilmer[26,27]. Using this model, the crystallization process on the surface during growth can be described by the diffusion of the deposited material in terms of single particle lattice hopping[XVI].

The diffusion kinetics is described by an Arrhenius hopping process on an $l \times l$ matrix, determined by the diffusion barrier E_D. The latter is comprised of two terms: $E_D = E_S + nE_N$, with E_S being the diffusion barrier of a free particle, n the nearest-neighbor co-ordination (n=0,1..,4) of each particle along the surface and E_N the energy of each bond formed with a nearest neighbor.

[XVI] Here, we assume that the particles are cubes with the size of one (pseudo-cubic) unit cell deposited on a simple cubic crystal lattice.

The hopping probability k is then given by:

$$k = k_0 \, exp\left(-\frac{E_S + nE_N}{k_B T}\right) \tag{4.2}$$

where k_0 represents the attempt frequency for atomic processes.

Note that a change in E_D is expected after deposition of one unit cell layer, due to a different atomic termination or epitaxial misfit strain[28]. The termination layer has an effect on the diffusion barrier E_S, while the epitaxial strain has an effect on both E_S and the detachment rate coefficient, determined by E_N. Misfit strain causes a reduction in the effective binding energy with a concomitant increase in the detachment rate[29]. The latter is increased more for large islands than for small islands. As a consequence, misfit strain will hamper formation of large islands. Both a decrease and enhancement of the energy barrier E_D are possible. A decrease of the energy barrier will increase the rate of surface diffusion and favors step flow growth because more atoms reach the terrace edge. A decrease of the rate of surface diffusion, due to an enhancement of the energy barrier, will increase the nucleation probability on the terraces.

The Monte Carlo simulation method applied here is extensively described[30] and a detailed description can be found elsewhere[31]. The pulsed nature of PLD is simulated by repetitive, instantaneous generation of a number of particles. These are randomly "deposited" on the surface with periodic boundary conditions. After deposition, the particles are allowed to diffuse[XVII].

The step density model for the $l \times l$ matrix is calculated by[32]:

$$S = \frac{1}{l^2} \sum_{i,j} \left| h_{i,j} - h_{i,j+1} \right| cos\, \phi + \left| h_{i,j} - h_{i+1,j} \right| sin\, \phi \tag{4.3}$$

where S is the step density, $h_{i,j}$ the step heights on the surface and ϕ the azimuthal angle of the electron beam with respect to the principal directions of the matrix. The RHEED intensity is estimated by:

$$I_{RHEED} \propto 1 - S \tag{4.4}$$

[XVII] Here, evaporation is neglected. Evaporation from the SrO terminated $SrRuO_3$ is expected to be negligible.

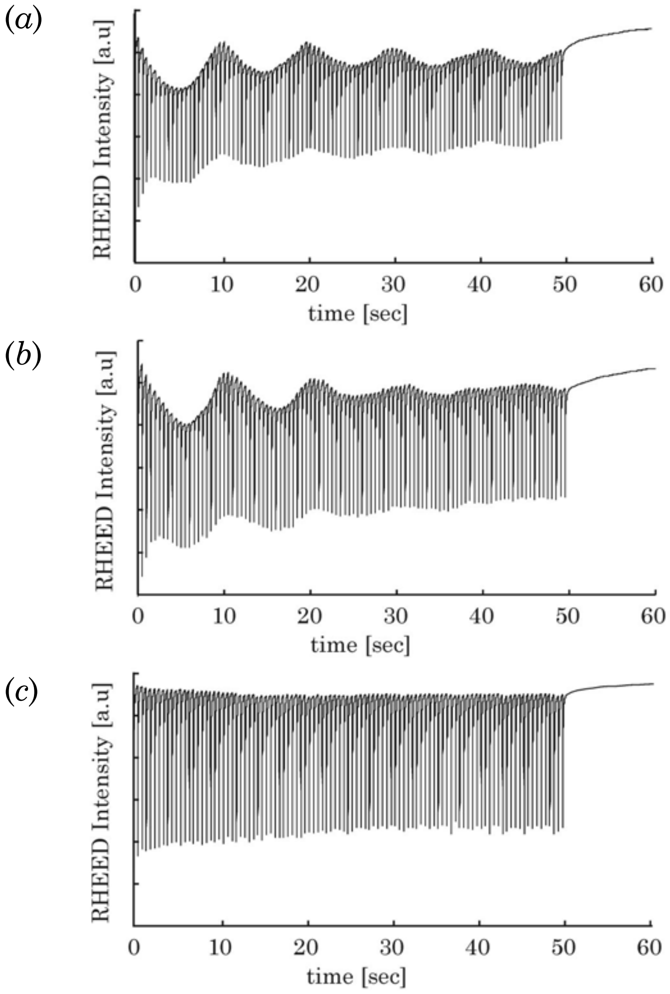

Figure 4.18: Simulated RHEED intensity variations during growth of 5 unit cell layers on substrates with different vicinal angles of 0.45° (a), 0.6° (b) and 1.0° (c). The deposition temperature was set to 600 °C, E_S = 0.75 eV and E_N = 0.6 eV, the pulse repetition rate = 2 Hz and the number of pulses needed for completion of one unit cell layer is 20.

Using the SOS model, the growth of $SrRuO_3$ on the SrO termination layer, i.e., after the termination conversion, has been simulated. Figure 4.18 (a), (b) and (c) show the simulated RHEED intensity variations during growth of 5 unit cell layers on substrates with different vicinal angles of 0.45, 0.6 and 1.0°. The values for E_S and E_N were 0.75 and 0.6 eV, respectively. These values[XVIII] resulted in growth

---

[XVIII] A value of 1e13 for the attempt frequency k_0 has been used, while ϕ was set to zero. A matrix size of 490x490 is used, corresponding to 200x200 nm. Because of this limited matrix size, the values for the vicinal angles used in the simulations are larger than the vicinal angles used in the RHEED experiments. The values for E_N and E_S resulted in simulated growth modes comparable to the experimental observed growth modes.

behavior comparable to the observed growth behavior at 600 °C and a pulse repetition rate of 2 Hz.

Step flow growth is observed at the highest vicinal angle of 1.0°, indicated by the steady RHEED intensity. No intensity oscillations are observed and the diffusion length of the diffusing particles is expected to be, at least, comparable to the terrace width. At the smaller vicinal angles, however, the growth is dominated by 2D nucleation and growth, indicated by the initial intensity oscillations. The oscillations damp during subsequent growth until a steady intensity and, therefore, a steady step density is reached. The transition to the steady step density depends on the vicinal angle and is distributed in time during growth of several unit cell layers.

Figure 4.19 shows several “snap-shots” of the simulated surface morphology during growth. Both the 2D island growth on the terraces and step advancement are clearly visible during growth of the first unit cell layer. Nucleation on the terraces takes place and subsequent deposition causes the islands to grow until they coalesce with the advancing steps. This process continues during the remainder of the deposition. The coalescence causes roughening of the step ledges and the transition to the steady step density. After deposition of ~4 unit cell layers, a steady state surface step density is reached on the substrate with vicinal angle of 0.6° and a “constant” surface morphology is observed. At smaller vicinal angle, the steady state is not reached after deposition of 5 unit cell layers. A clear difference is observed in the surface morphology at full and half unit cell layer coverage.

Although a steady RHEED intensity is observed during growth on the substrate with vicinal angle of 1.0°, see figure 4.18, nucleation and 2D growth does occur on the terraces, indicated by the dashed circles in figure 4.19.

4.6 Conclusions

The initial growth of $SrRuO_3$ on well-defined vicinal $SrTiO_3$ substrates with TiO_2 termination is studied. The following growth features have been observed using *in situ* RHEED intensity measurements:

(1) The terminating atomic layer converts[33] from B-site (TiO_2 terminated $SrTiO_3$) to A-site (SrO terminated $SrRuO_3$) caused by the evaporation of Ru_xO_y products. The latter takes place since the RuO_2 terminating atomic layer is not stable at the PLD conditions used.

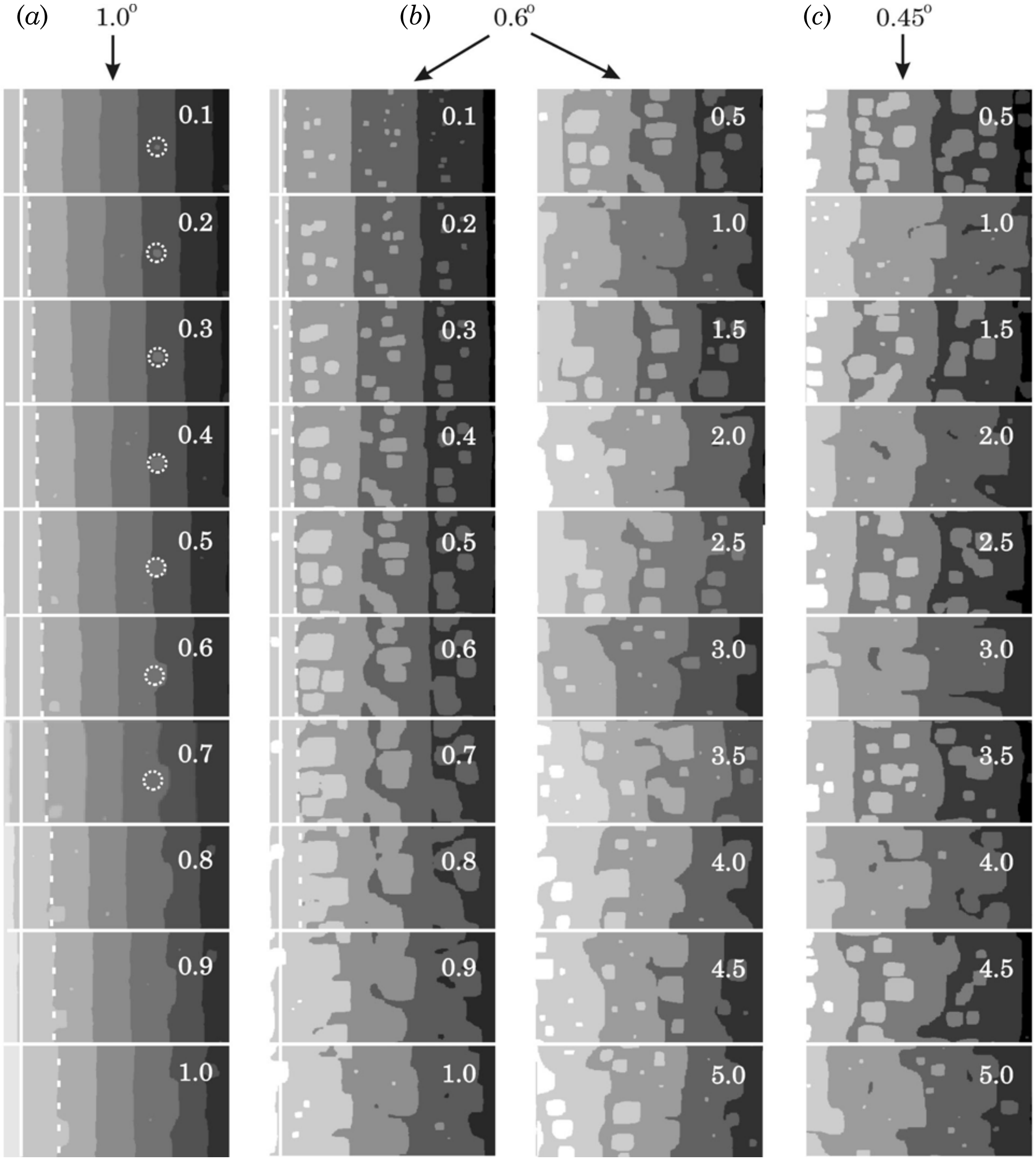

Figure 4.19: Simulated surface morphologies at different stages during growth from 0.1 - 5 unit cell layers on substrates with different vicinal angles of 1.0° (a), 0.6° (b) and 0.45° (c). The advancing steps, indicated by the dashed lines, coalesce with the growing islands on the terraces.
The deposition temperature was set to 600 °C, E_S = 0.75 eV and E_N = 0.6 eV, the pulse repetition rate = 2 Hz and the number of pulses needed for completion of one unit cell layer is 20.

(2) The conversion is accompanied by an enhanced surface diffusivity. A surface energy diffusion barrier E_A of 1.0 ± 0.2 eV is found after completion of the termination conversion. During initial growth, i.e., first unit cell layer, 2D growth is observed, whereas after the termination conversion the growth is dominated by step advancement.

(3) At low vicinal angle, nucleation of islands on the terraces occurs. During subsequent deposition, coalescence of the advancing steps with the spreading islands leads to a constant step density, independent of the vicinal angle. The latter can be seen as a self-organization of the step density and, as a result, a constant RHEED intensity is observed.

As shown, the growth of $SrRuO_3$ on $SrTiO_3$ cannot be described by pure step flow growth since nucleation on the terraces occurs on vicinal substrates with the terrace width comparable to the diffusion length of the deposit. This growth mechanism was simulated using the SOS model. The simulated RHEED intensity variations, calculated from simulated step density, showed remarkable resemblance with the observed RHEED intensity. The cubic unit cell is found as the growth unit, deduced from the step heights of both step ledges and island ledges. No evidence is found of preferential nucleation of the orthorhombic unit cell at substrate step ledges.

References

1 J.J. Randall and R. Ward, *J. Am. Chem. Soc.* **81**, 2629 (1959)

2 C.B. Eom, R.J. Cava, R.M. Fleming, J.M. Philips, R.B. van Dover, J.H. Marshall, J.W.P. Hsu, J.J. Krajewski and W.F. Peck*,* *Science* **258**, 1766 (1992)

3 R. A. Rao, Q. Gan and C. B. Eom, *Appl. Phys. Lett.* **71**, 1171 (1997)

4 J.C. Jiang, W. Tian, X.Q. Pan, Q. Gan and C.B. Eom, *Appl. Phys. Lett,* **72**, 2963 (1998)

5 A.F. Marshall, L. Klein, J.S. Dodge, C.H. Ahn, J.W. Reiner, L. Mieville, L. Antognazza, T.H. Geballe and M.R. Beasley, *J. Appl. Phys.* **85**, 4131 (1999)

6 D.B. Kacedon, R.a. Rao and C.B. Eom, *Appl. Phys. Lett.* **71**, 1724 (1997)

7 Y. Kats, L. Klein, J.W. Reiner, T.H. Geballe, M.R. Beasley and A. Kapitulnik, *Phys. Rev. B* **63**, 054435 (2001)

8 R. A. Rao, D. B. Kacedon and C. B. Eom, *J. Appl. Phys.* **83**, 6995 (1998)

9 Q. Gan, R. A. Rao and C. B. Eom, *Appl. Phys. Lett.* **70**, 1962 (1997)

10 J-P Maria, H.L. McKinstry and S. Trolier-McKinstry, *Appl. Phys. Lett.* **76**, 3382 (2000)

11 R.J. Bouchard and J.L. Gillson, *Mater. Res. Bull.* **7**, 873 (1972)

12 C.W. Jones, P.D. Battle, P. Lightfoot and T.A. Harrison, *Acta Crystallogr.,Sect. C: Cryst. Struct. Commun.* **45**, 365 (1989)

13 B.J. Kennedy and B.A. Hunter, *Phys. Rev. B* **58**, 653 (1998)

14 Q. Gan, R. A. Rao, C. B. Eom, J.L. Garrett and M. Lee, *Appl. Phys. Lett.* **72**, 978 (1998)

15 C.L. Chen, Y. Cao, Z.J. Huang, Q.D. Jiang, Z. Zhang, Y.Y. Sun, W.N. Kang, L.M. Dezaneti, W.K. Chu and C.W. Chu, *Appl. Phys. Lett.* **71**, 1047 (1997)

16 N.D. Zakharov, K.M. Satyalakshmi, G. Koren and D. Hesse, *J. Mater. Res.* **14**, 4385 (1999)

17 C.H.S. Ahn, *Growth and properties of epitaxial complex oxides*, PhD thesis, Stanford University, chapter4 (1996)

18 J-P Maria, S. Trolier-McKinstry, D.G. Schlom, M.E. Hawley and G.W. Brown, *J. Appl. Phys.* **83**, 4373 (1998)

19 J. Choi, C.B. Eom, G. Rijnders, H. Rogalla and D.H.A. Blank, *Appl. Phys. Lett.* **79**, 1447 (2001)

20 Z. Sh. Yanovitskaya, I.G. Neizvestny, N.L. Shwartz, M.I. Katkov, I.P. Ryzhenkov, *Appl. Surf. Sci.* **123/124,** 729 (1998)

21 J.-G. Lee. Y.T. Kim, S.-K Min and S.H. Choh, *J. Appl. Phys.* **77**, 5473 (1995)

22 D.P. Vijay, S.B. Desu and W. Pan in *Ferroelectric Thin Films III*, E.R. Myers, B.A. Tuttle, S.B. Desu and P.K. Larsen ed. (Materials Research Society, Pittsburg, PA, 1993) pp. 133

23 Q.X. Jia, S.G. Song, X.D. Wu, J.H. Cho, S.R. Foltyn, A.T. Findikoglu and J.L. Smith, *Appl. Phys. Lett.* **68**, 1069 (1996)

24 Private communication with V. Matijasevic (OXXEL GmbH, Bremen, Germany). The resolution of Sr with Ru is not very good in most of the spectra, but there is not much Ru in the spectra, or at most it would be a shoulder.

25 X.D. Zhu, *Phys. Rev. B* **58**, 10975 (1998)

26 D.D. Vvedensky, S. Clarke, K.J. Hugill, A.K. Myers-Beaghton and M.R. Wilby in *Kinetics of Ordering and Growth at Surface*, M. G. Lagally ed. (Plenum Press, London, 1990) pp. 297-311

27 J.D. Weeks and G.H.Gilmer, *Adv. Chem. Phys.* **40**, 344 (1979)

28 C. Ratch, and A. Zangwill, *Appl.Phys. Lett.* **63**, 2348 (1993)

29 C. Ratch, M.D. Nelson and A. Zangwill, *Phys. Rev. B* **50**, 14489 (1994)

30 P.A. Maksym, *Semicond. Sci. Technol.* **3**, 594 (1988)

31 E. van Setten, masters thesis, University of Twente (1999)

32 V.S. Achutaraman, N. Chandrasekhar, O.T. Valls and A. M. Goldman, *Phys. Rev. B* **50**, 8122 (1994)

33 G. Rijnders, J.H. Choi, C.B. Eom, H. Rogalla and D.H.A. Blank, to be published

Chapter 5

Initial growth of $REBa_2Cu_3O_{7-\delta}$

5.1 Introduction

The structural properties, i.e., defect structure, crystalline structure and surface morphology, of $REBa_2Cu_3O_{7-\delta}$ (RE123) thin films influence the electrical properties and determine their applicability in multilayer structures. For instance, structural defects, grain boundaries and anti-phase boundaries (APB's) play an important role in the flux pining mechanism[1,2,3,4], whereas the surface morphology of RE123 thin films is important in multilayer structures which require smooth surfaces. Both structural properties and surface morphology are a direct result of the thin film growth, influenced by deposition conditions and substrate properties. At the initial stage of the growth, the stacking sequence of the individual atomic layers in RE123 at the interface with the substrate is influenced by the substrate surface properties, i.e., the terminating atomic layer and the crystalline structure. During subsequent deposition, the lattice mismatch between the substrate and the growing film becomes dominant.

Various deposition techniques, most frequently physical vapor deposition (PVD), are applied for the growth of RE123 thin films. Among them are reactive co-evaporation, molecular beam epitaxy (MBE), laser-MBE and pulsed laser deposition (PLD). Reflection high-energy electron reflection (RHEED) is most often used to study the growth of RE123 *in situ*. Independent of the deposition technique, oscillation of the RHEED intensity is observed caused by the two-dimensional (2D), unit cell layer-by-layer growth of RE123[5] when all constituents are provided simultaneously. It is found that the oscillation period corresponds precisely to the time necessary for deposition of one unit cell layer in the c-axis

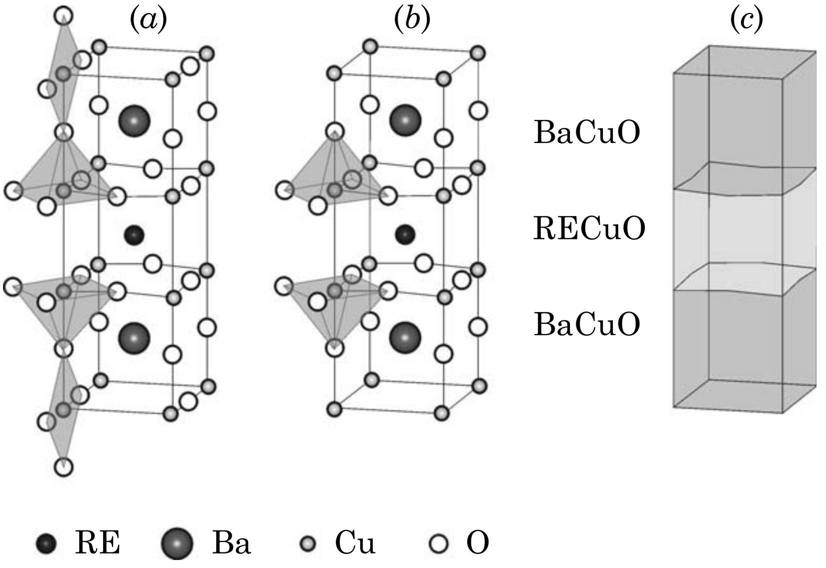

Figure 5.1: Schematic representation of the unit cell of $REBa_2Cu_3O_7$ *(a) and* $REBa_2Cu_3O_6$ *(b) consisting of three perovskite blocks (c). Note that the Cu-chain layer, i.e., the topmost layer in (b), is oxygen depleted in* $REBa_2Cu_3O_6$.

direction. In general, it is believed that in epitaxial growth of ionic oxides the growth unit with a certain chemical composition has to satisfy charge neutrality. In the case of RE123 this minimum growth unit is the unit cell consisting of 6 atomic layers, see figure 5.1.

Growth in charge neutral unit cells has implications in the 2D epitaxial growth of RE123. First, a specific stacking sequence of the atomic layers should exist and, second, the growth unit should always terminate with the same atomic layer. Since the first atomic layer is determined by both substrate and film, the following questions arise:

(1) Is the charge neutral growth unit during the initial, heteroepitaxial growth, i.e., deposition of the first unit cell layer, also the unit cell of RE123 consisting of 6 atomic layers?
(2) Is the terminating atomic layer of the RE123 thin film depending on the terminating atomic layer of the substrate or is it thermodynamically determined by RE123 itself?
(3) Is the terminating atomic layer influenced by the deposition conditions?

In this chapter a state-of-the-art overview is given of the complex growth mechanisms of RE123 on $SrTiO_3$ substrates. Combined with experimental results, the questions mentioned above will be addressed and, if possible, answered. *In situ* RHEED, *ex situ* atomic force microscopy (AFM), and high-resolution electron microscopy (HREM) have been applied to study the growth of RE123 on $SrTiO_3$ at typical PLD conditions.

5.2 Nucleation stage and initial growth

Several groups have studied the initial growth of RE123 on $SrTiO_3$ in detail. The most important subjects of these studies were the interface between RE123 and $SrTiO_3$ and the terminating atomic layer of the first unit cell layer(s). Various techniques are applied such as x-ray standing waves (XSW), HREM and surface sensitive ion scattering spectroscopy.

5.2.1 Atomic layer stacking sequence at the interface between RE123 and $SrTiO_3$

Using HREM, Wen *et al.*[6] determined the stacking sequence of Y123, prepared by different techniques including evaporation, sputter deposition and PLD, on $SrTiO_3$. They found, independent of the growth technique, the stacking sequence to be: *bulk-SrO-*TiO_2*-BaO-*CuO_2*-Y-*CuO_2*-BaO-CuO-bulk*. To determine the proposed stacking sequence, the terminating atomic layer of the substrate needs to be TiO_2. Without proper treatment, however, mixed terminated $SrTiO_3$ substrates are expected[7] enabling other stacking sequences. Still, from the high-resolution images it was found that the perovskite stacking sequence is preserved at the interface between Y123 and $SrTiO_3$. Using XSW, the interface structure of c-axis oriented Gd123 and Eu123 films on $SrTiO_3$ substrates was determined by Nakanishi *et al.*[8]. The experimental results indicated that for Gd123 as well as Eu123 neither the CuO nor the CuO_2 layer can be the first atomic layer on TiO_2 terminated $SrTiO_3$ and neither the BaO layer nor the oxygen depleted RE layer can be the first atomic layer on SrO terminated $SrTiO_3$. Therefore, a perovskite stacking sequence is proposed. Zegenhagen *et al.*[9] demonstrated, using soft XSW, that the stacking sequence of Y123 (prepared using evaporation) on $SrTiO_3$ is perovskite-like at the interface.

5.2.2 Terminating atomic layer of RE123

The surface of a fully oxidized, orthorhombic RE123 ($\delta \sim 0$) crystal can have several atomic layers at the (001) surface: CuO_2, CuO, BaO and the oxygen deficient RE layer. These surfaces are differentiated by their composition and depend on the sequence of the underlying atomic layers.

Tanaka *et al.*[10] investigated the surface structure of Y123 deposited by ozone-assisted reactive co-evaporation on $SrTiO_3$ using *in situ* low-energy electron diffraction (LEED) and low-energy ion scattering spectroscopy (LEISS). From their LEED measurements it was concluded that the surface of the film is clean, crystalline and atomically flat. The films have an in-plane epitaxial relation of [100]Y123//[100]$SrTiO_3$ and [110]Y123//[110]$SrTiO_3$. LEISS shows Cu and O atoms in the terminating layer of the surface. Through anneal experiments and measuring the O_2 desorption from the film it is concluded that the CuO chain layer is the terminating layer. Using depth profiling[11] the second layer is determined to be BaO. The stacking sequence of the top unit cell layer is found to be *BaO-CuO_2-Y-CuO_2-BaO-CuO*. Shimura *et al.*[12] confirmed this stacking sequence by cross-sectional HREM.

Matijasevic *et al.*[13,14] studied the growth mechanism of co-evaporated (by reactive MBE) Sm123 thin films using atomic force microscopy (AFM) and high-resolution electron microscopy (HREM). AFM studies of less than one unit cell thick Sm123 films show preferential nucleation at the substrate steps. By changing the cation stoichiometry it was shown that irrespective of the composition, nucleation of molecular units with the same height occurred. Based on the height analysis of the Sm123 nucleation islands, a 1:3:3 cation stoichiometry for nucleation on TiO_2 terminated[I] $SrTiO_3$ has been found, while x-ray photon spectroscopy (XPS) shows BaO termination. To match the proposed stacking sequence of the nucleated islands with AFM height measurements a reaction of the terminating BaO layer with air had to be taken into account. This reaction leads to a $BaCO_3$ top layer and, subsequently, to a height increase of 2 Å.

Behner *et al.*[15] studied Y123 prepared by DC-magnetron sputter deposition *in situ* using XPS and found a uniform BaO termination. The proposed stacking sequence is: *bulk-BaO-CuO_2-Y-CuO_2-BaO-CuO-BaO*. From *ex situ* XPS it was concluded that carbonates are formed on the film surface within the first few hours due to reaction with CO_2 upon exposure in air.

Pennycook *et al.*[16] concluded from amorphization experiments, induced via oxygen ion implantation at room temperature, that Y123 films, deposited with PLD using molecular oxygen, terminate with the CuO chain plane. Z-contrast electron microscopy demonstrates growth to be unit cell layer-by-layer through sequential nucleation and coalescence of islands. It was concluded that the unit cell terminates with the CuO chain layer. They considered amorphization as the reverse of the growth process.

Badaye *et al.*[17,18] used atomic resolved AFM to determine the terminating layer of Nd123[19] made by PLD. They found the CuO chain layer to be the terminating layer, which was confirmed by total reflection angle X-ray spectroscopy (TRAXS)[20]. In order to perform these spectroscopic measurements, the samples had to be cleaned *in situ* at 200 °C for 20 min with an atomic oxygen beam.

Rao *et al.*[21] determined the surface layer of Y123 with the glancing incident exit x-ray diffuse scattering (GIEXS) technique. It was shown that for a heat-treated

---

[I] The terminating atomic layer of the substrate was deduced from HREM measurements.

PLD film the terminating layer is a mixture of BaO_2 and BaO. The topmost layer was shown to be the CuO plane after a heat treatment in a radical O* atmosphere.

Huibregtse *et al.*[22] concluded from AFM analysis of sub-unit cell Y123 films the terminating atomic layer to be CuO on TiO_2 terminated $SrTiO_3$. The proposed stacking sequence for the first unit cell layer is *bulk-SrO-*TiO_2*-BaO-*CuO_2*-Y-*CuO_2*-BaO-CuO.* On SrO terminated $SrTiO_3$, on the other hand, BaO is expected to be the terminating layer. In this case the stacking sequence is *bulk-SrO-BaO-*CuO_2*-Y-*CuO_2*-BaO.* In the latter case the remaining CuO leads to the formation of CuO_x precipitates. Sub-unit cell deposition, however, leads to nucleation of a cubic $(Y,Ba)CuO_3$ phase[23] due to minimization of surface and interface energies. Determination of the terminating atomic layer of Y123 from AFM analysis is, therefore, not straightforward.

5.2.3 Discussion

Both the starting and terminating atomic layer of RE123 on $SrTiO_3$, deposited using various techniques, have been experimentally determined. An overview is listed in table 5.1. In most cases, a perovskite stacking sequence has been found at the interface. The starting atomic layer could only be determined assuming the terminating atomic layer of the $SrTiO_3$ substrate to be predetermined, i.e., either SrO or TiO_2. Without correct treatment of $SrTiO_3$ substrate surfaces, however, the termination is not well defined. Most of the experiments reported in literature concerning the first atomic layer of RE123 on $SrTiO_3$ have been performed on heat-treated substrates. Since a mixed termination is expected using heat treatments, the first atomic layer remains unclear. Nonetheless, a perovskite stacking sequence has been found in most cases. The first atomic layer of RE123 is, therefore, determined by the substrate terminating atomic layer.

The experimental results, reported in literature, concerning the terminating atomic layer of RE123 thin films are controversial and, therefore, the terminating layer remains ambiguous. Independent of the RE element, BaO[14,15,21,22,24,25,26] as well as the CuO[10,11,12,16,17,20,22] chain layer have been found as the terminating layer. Experimental determination of the terminating layer, however, is not straightforward. The terminating layer will depend on the environment, i.e., temperature and oxygen pressure[II], during growth and post deposition treatments. *Ex situ* measurements usually involve surface treatments like annealing and/or ion bombardment to clean the surface prior to the measurement. Since modification of the surface is to be expected, determination of the terminating layer is difficult. For instance, a BaO termination was found after heat treatment, whereas treatment in radical O* environment a CuO was found to be the terminating layer[21].

[II] The oxidation power depends on the oxygen source used, e.g., molecular or atomic oxygen, ozone, NO_2, etc.

Table 5.1: Overview of the experimentally determined starting and terminating atomic layers of RE123.

Authors	RE123	Deposition technique	Ambient gas	Analysis technique	Starting atomic layer	Terminating atomic layer	Remarks
Wen *et al.*[6]	Y123	Reactive coevaporation	Ozone	*Ex situ* HREM	BaO		
Nakanishi *et al.*[8]	Gd123* Eu123#	*Coevaporation #Magnetron sputter deposition	O_2	*Ex situ* XSW			Perovskite stacking sequence at substrate-film interface.
Matijasevic *et al.*[13,14]	Sm123	Reactive MBE	Ozone	*Ex situ* AFM	BaO	BaO	First unit cell layer has 1:3:3 cation stoichiometry.
Zegenhagen *et al.*[9]	Y123	MBE	O_2	*Ex situ* XSW	BaO		Perovskite $BaCu(Ti)O_x$ unit cell at interface.
Haage *et al.*[23]	Y123	PLD	O_2	*In situ* UHV STM			Non-unit cell nucleation.
Nakamura *et al.*[11]	Y123	Reactive co-evaporation	Ozone	*Ex situ* LEISS		CuO	Second layer BaO determined by depth profiling.
Tanaka *et al.*[10]	Y123	Reactive co-evaporation	Ozone	*In situ* LEISS		CuO	
Shimura *et al.*[12]	Y123	Co-evaporation	Ozone	*Ex situ* HREM	BaO	CuO	
Badaye *et al.*[17,18]	Nd123	PLD	O_2	*Ex situ* AFM		CuO	
Liu *et al.*[20]	Nd123	PLD	O_2	*Ex situ* TRAXS		CuO	Surface cleaned with atomic oxygen.

Table 5.1: Overview of the experimentally determined starting and terminating atomic layers of RE123 (continued).

Pennycook *et al.*[16]	Y123	PLD	O_2	*Ex situ* HREM		CuO	Determined through oxygen ion implantation.
Behner *et al.*[15]	Y123	Magnetron sputter deposition	O_2	*In situ* XPS		BaO	*Ex situ* XPS shows carbonate formation.
Rao *et al.*[21]	Y123	PLD	O_2	*Ex situ* GIEXS		BaO_x/ CuO	BaO termination after heat treatment/ CuO termination after treatment by radical oxygen bombardment.
Kawasaki *et al.*[24]	Y123	PLD	O_2	*Ex situ* scanning tunneling spectroscopy		BaO	
Frank *et al.*[25]	Y123	Thermal evaporation	O_2	*Ex situ* angle resolved XPS		BaO	
Huijbrechtse *et al.*[22]	Y123	PLD	O_2	*Ex situ* AFM	BaO	BaO/ CuO	BaO termination plus CuO_x precipitation on SrO terminated $SrTiO_3$. CuO termination on TiO_2 terminated $SrTiO_3$.
Rijnders *et al.*[26,59]	Y123	PLD	O_2	*In situ* RHEED/ *Ex situ* HREM	BaO	BaO	Perovskite stacking at interface and BaO termination on both SrO and TiO_2 terminated $SrTiO_3$. (CuO_x precipitation on TiO_2 terminated $SrTiO_3$).

Employing amorphization by oxygen ion implantation at room temperature[16], it was demonstrated that Y123 thin films, deposited by PLD in molecular oxygen, terminate with the CuO chain layer. Growth, however, takes place at elevated temperature and low oxygen pressure. Decomposition of the CuO chain plane is more likely at these temperatures compared to room temperature. Therefore, the terminating atomic layer during growth can be different from the terminating atomic layer of a treated RE123 film. The CuO chain layer has zero net charge and has been predicted[27] as the most stable surface. In the case of oxygen depleted tetragonal RE123 ($\delta \sim 1$) the BaO surface possesses neutral charge and becomes the stable terminating atomic plane.

During growth, the oxygen content in the surface layer is in equilibrium with both the oxygen in the film and gas phase. To stabilize the RE123 film a certain amount of oxygen has to be incorporated in the surface. The deposition pressure during growth of RE123 depends on the deposition technique. While low pressures (typically below 10^{-2} Pa) are used in MBE and laser-MBE, higher pressures (between 1 and approximately 100 Pa) are used in PLD and sputter deposition. The oxidation power of molecular oxygen at these high pressures has been proven to be sufficient to stabilize the RE123 film[28],[III] at deposition conditions. At low deposition pressures, however, more adequate oxidants like oxygen ions, atomic oxygen, ozone or nitrogen peroxide have to be used. Consequently, RE123 films can be stabilized at both low and high deposition pressure using suitable oxidation gasses. The termination layer, however, also depends on the oxidation power at deposition conditions. As mentioned earlier, at high temperatures, for example deposition temperatures, Cu-O bonds are easily broken, resulting in desorption of oxygen. A high oxidant flux density is necessary to avoid the decomposition and, subsequently, to stabilize the CuO chain layer. Because of the different oxidation power used in the mentioned deposition techniques it is, therefore, expected that stabilization of the CuO chain layer depends on the deposition conditions. As a result, the terminating layer of the as-deposited film will depend on the deposition conditions and is not always thermodynamically determined by the RE123 itself.

5.3 Influence of substrate properties on RE123 growth

The growth mode as well as the atomic stacking sequence at the substrate-film interface is affected by the substrate properties. The surface step density of $SrTiO_3$ substrates and the lattice mismatch with RE123 have an especially large influence on the growth mode and will be discussed.

[III] At PLD conditions the RE123 film will be oxygen depleted resulting in the tetragonal phase, Lopez *et al.*[28].

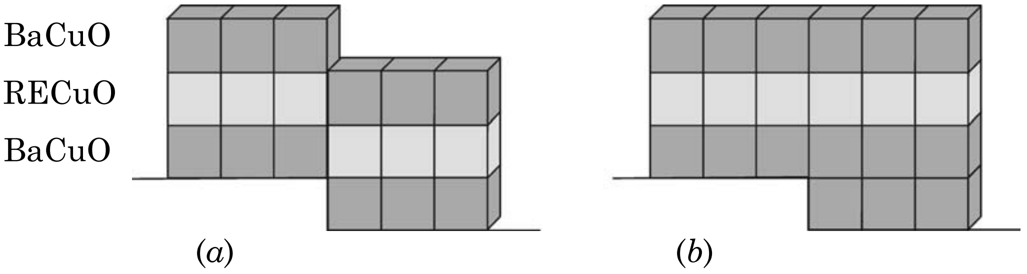

Figure 5.2: Schematic view of an anti-phase boundary (a) at a $SrTiO_3$ substrate step with displacement vector $[00\frac{1}{3}]$ *and the variable stacking sequence (b).*

5.3.1 Influence of the vicinal angle on the growth mode

$SrTiO_3$ substrates used for deposition of RE123 typically have a vicinal angle between 0.05° and 0.5°, resulting in a step-terrace surface morphology. Assuming 3.905 Å as the average step height, i.e., the lattice parameter of $SrTiO_3$, an average terrace length between ~500 and ~50 nm is expected. The step edges of the substrate act as a preferential adsorption site for atoms diffusing on the surface of the substrate. The nucleation and growth are, therefore, expected to depend on the relation between the terrace length l_T and the surface diffusion length l_D. If $l_D > l_T$, nucleation on the terrace is prevented resulting in step flow like growth[14,29,30,31,32]. On the other hand, if $l_D < l_T$, nucleation on the terrace occurs resulting in 2D growth. Nevertheless, preferential nucleation will also take place at the step edges[33,14].

The diffusion length of Y123 in PLD[IV] is determined by STM studies[34] on vicinal substrates. The crossover from step flow like growth to 2D nucleation and growth is observed on substrates with 1.2° vicinal angle. From this, a surface diffusion length l_D ~20 nm was determined.

5.3.2 Influence of the vicinal angle on structural defects

At the initial growth, nucleation and growth towards steps in the substrate lead to the formation of anti-phase boundaries[14,29,30,35] (APB's). These APB's are perpendicular to the interface and can be described by a displacement vector $R=[00\frac{1}{3}]$, see figure 5.2 (a). Mechanisms preventing APB's being formed at the substrate steps or annihilating APB's have been proposed in literature. A variable stacking mode[4] at the substrate steps during nucleation of Y123 creates the possibility of partial overgrowth at these steps, see figure 5.2 (b). Here, on the lower terrace, an additional $BaCuO_x$ layer (~4Å) prevents the formation of the APB. This additional $BaCuO_x$ layer can be seen as non-unit cell growth and

---

[IV] At 0.2 mbar oxygen pressure and 760 C.

changes the stacking sequence at the initial growth. As a result, the terrace length of the film is larger than that of the substrate. Due to the displacement vector R=$[00\frac{1}{3}]$, however, not all APB's at the substrate steps are prevented by the proposed variable stacking sequence[V].

Non-unit cell growth, like the variable stacking sequence, is not only observed at the initial growth, but also during subsequent growth. APB's in the film that originate from steps in the substrate annihilate[35] by non-unit cell growth at later stages of the growth, enabling an energetically more favorable growth.

5.3.3 Influence of strain on the growth

As described in chapter 3, lattice mismatch between film and substrate gives rise to epitaxial strain, which is relieved by the introduction of misfit dislocations above the critical thickness h_C. Several strain relieving mechanisms during heteroepitaxial growth of RE123 on $SrTiO_3$ (lattice mismatch ~1.6%) have been proposed[36,37,38,39,40,41]. Although the mechanisms for dislocation nucleation differ in nature, pseudomorphic growth has been found for layer thickness smaller than the critical thickness h_C. Values of h_C between 5 and 20 nm, i.e., between ~4 and ~16 unit cell layers[42,43,44,45,46,47], have been found for RE123 deposited on $SrTiO_3$ by PLD using molecular oxygen. Huijbregtse *et al.*[22] found that the critical thickness depends strongly on the $SrTiO_3$ substrate termination. A value for h_C of 7.3 nm on SrO terminated substrates and 19 nm for TiO_2 terminated substrates was found. From this, they concluded that the larger substrate-film interface energy for the TiO_2 termination enabled stabilization of a thicker pseudomorphic layer.

Not only the substrate termination, but also the growth conditions determine the critical thickness h_C. The film surface morphology, which is a direct product of the growth process, has a large influence on the nucleation of dislocations. Stress relaxation via dislocation nucleation at the critical thickness depends, therefore, on the growth conditions. For instance, nucleation of dislocations in a structurally perfect film with a smooth surface is extremely difficult. As a result, a large critical thickness h_C is expected. The large difference in the experimentally determined h_C values is, therefore, probably a result of the growth conditions. Note that control of the surface morphology during growth can be used to increase the critical thickness for pseudomorphic growth.

[V] Another stacking sequence is necessary to obtain $[00\frac{2}{3}]$ displacement.

5.4 Experiments: RE123 on $SrTiO_3$

The questions presented in the introduction of this chapter have been discussed in many papers in the last ten years. Most discussions, however, are based on RE123 films deposited on $SrTiO_3$ substrates with unknown termination. As a result, the first atomic layer and stacking sequence of the individual atomic layers of the first unit cell layer of RE123 remains ambiguous.

In this study accurate control of the terminating layer of the $SrTiO_3$ substrate as well as *in situ* diagnostics by high-pressure RHEED have been used. Chemical treatment followed by heat treatment has proved to be a suitable method to obtain single TiO_2 terminated $SrTiO_3$ with atomically smooth terraces, see chapter 2. The use of these substrates enables the determination of the stacking sequence unambiguously with, for instance, HREM.

5.4.1 Experimental settings

The deposition conditions used in PLD of RE123 influences the growth significantly. This holds true especially for the laser energy density at the target[48,49,50], the growth temperature and the oxygen deposition pressure[51,52] and these are, therefore, important parameters. Although a wide range of the parameter values have been investigated, only a small range have been found for optimized growth. As a result the parameter “space” converged to a typical set of values. The growth conditions used in this work are comparable to this set.

During growth of RE123, the substrate was heated to a temperature of 780°C and an oxygen background pressure of 18 Pa was applied. A sintered ceramic target was used which contained cations in nominal ratio RE:Ba:Cu = 1:2:3. The energy density at the target[53,54,55,VI] was 1.3 J/cm^2. The distance between substrate and target was 58 mm. At this position, the substrate is just at the end of the visible plasma. Using these settings, films with transition temperatures of typically 90 K are produced. AFM measurements show surface morphologies resulting from a 2D growth mechanism. No growth spirals are observed at these

---

[VI] Stoichiometric transfer from target to substrate is typically found above 1.3 J/cm^2. Lower densities leads to preferential ablation (between 1.0 and 1.3 J/cm^2) or phase separation in the target (below 1.0 J/cm^2). Phase separation at these low energy densities occurs due to the incongruent melting of RE123. Due to repetitive irradiation below the threshold of 1.3 J/cm^2, both, composition and morphology of the target surface is altered. As a consequence, the film characteristics during deposition change.

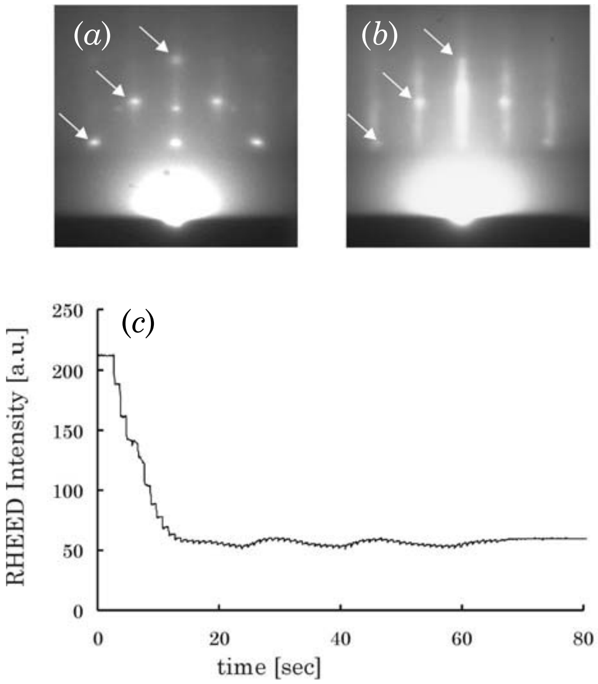

Figure 5.3: RHEED patterns recorded after deposition of 1 (a) and 4 (b) unit cell layers of Y123 on TiO_2 terminated $SrTiO_3$ and the specular RHEED intensity recorded during initial growth (c).

growth conditions[VII,56,57,58]. In the remainder of this chapter the mentioned growth conditions are referred to as *standard* growth conditions.

The RE123 films are deposited on TiO_2 terminated (001) $SrTiO_3$ substrates using the PLD equipment described in chapter 2. The typical vicinal angle of the substrates is between ~0.05 and ~0.2°, yielding an average terrace length of ~400 to ~100 nm, respectively. All RHEED measurements are performed with 20 KV acceleration voltage. The angle of incidence was ~1°. The azimuthal angle was ~0° with respect to the [010] or [100] orientation of the $SrTiO_3$ substrate.

[VII] The thermalization of ejected particles from the target is heavily influenced by the deposition pressure and determines the impingement energy of the particles arriving at the substrate (see chapter 2 for a detailed description). Generally, 2D nucleation and growth is observed at typical PLD conditions for RE123 growth, i.e., pO_2 ~10-30 Pa and substrate placed at the end of the visible laser plasma. Higher deposition pressure decreases the impingement energy and, therefore, the diffusion length of the deposit. A transition from the 2D nucleation and growth mode to the spiral growth mode is observed when the diffusion length between the deposition pulses becomes sufficiently small.

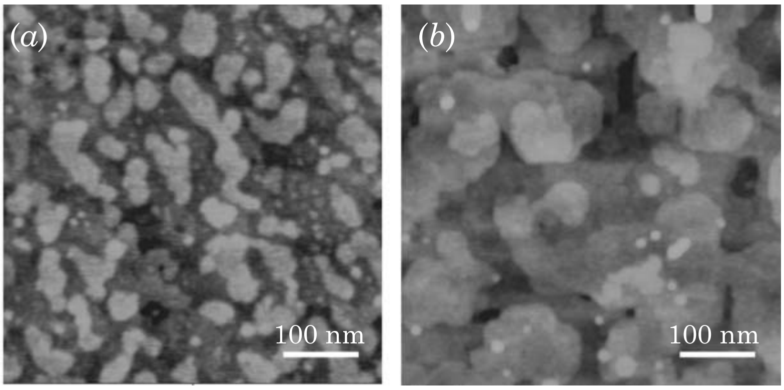

Figure 5.4: AFM micrographs of a 4 (a) and 20 (b) unit cell thick Y123 film on TiO_2 terminated $SrTiO_3$.

5.4.2 Initial growth of RE123 on TiO_2 terminated $SrTiO_3$

The RHEED patterns recorded after the deposition of 1 and 4 unit cell layers Y123 on TiO_2 terminated $SrTiO_3$ are depicted in figure 5.3 (a) and (b), respectively. Already at the initial growth, i.e., the deposition of the first few unit cell layers, the sharp 2D spots, originating from the $SrTiO_3$ substrate, are blurred into streaks. These streaks originate from the unit cell of Y123. The corresponding specular RHEED intensity shows a sharp decrease during deposition of the first unit cell layer without a large recovery, see figure 5.3 (c). Intensity oscillations are damped after deposition of approximately 4 unit cell layers. The observed streaks in the RHEED pattern and loss of RHEED intensity are indications of a roughened surface, i.e., the step density at the surface is increased[VIII].

This increase can be seen in the AFM micrographs depicted in figure 5.4 (a) and (b), showing the surface morphology of 4 and 20 unit cell thick Y123 layers, respectively. Clearly the growth proceeds by 2D nucleation and subsequent spreading into larger 2D islands. Besides steps with heights corresponding to the c-axis lattice parameter, smaller steps, corresponding to sub-unit cell heights, are visible.

Note that the average island size is small compared to the terrace width of the vicinal substrate. The vicinal substrate steps are, therefore, not responsible for most of the sub-unit cell steps at the surface of the Y123 film. The morphology of the 20 unit cell thick film is a result of 2D nucleation and growth. Here, nucleation and incorporation of adatoms at step edges is proceeding on an increasing number of unit cell levels. For example, in figure 5.4 (b) up to 4 unit cell levels can be seen.

[VIII] Bulk lattice parameters of substrate and film influence the specular RHEED intensity because of the small penetration depth of the electron beam and multiple scattering effects. The angle of incidence used in the experiments is set to ~1°. At this angle, the specular RHEED intensity is maximal on $SrTiO_3$. A small increase (~10%) of the specular RHEED is always observed by a small change of the angle of incidence of the electron beam after deposition.

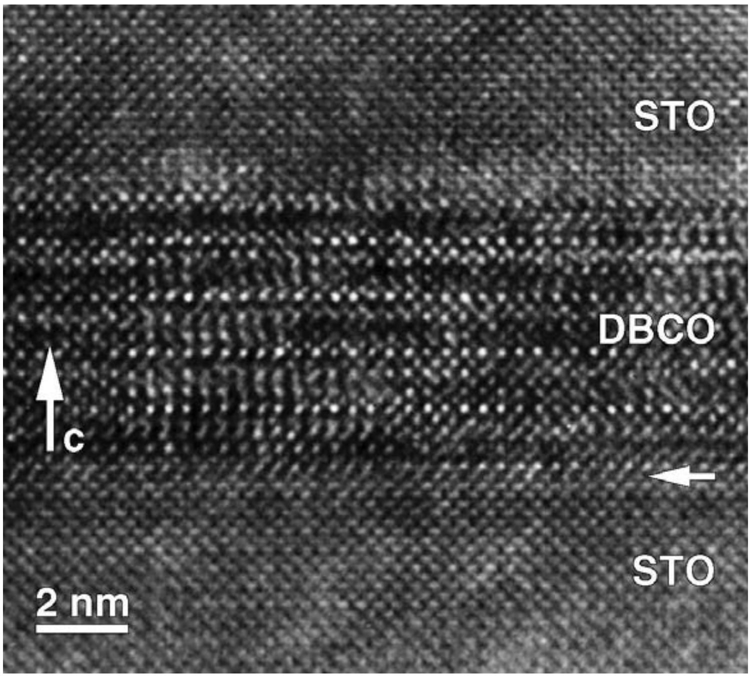

Figure 5.5: Overview transmission electron micrograph of 4 unit cell layers Dy123 on TiO_2 terminated $SrTiO_3$. The horizontal arrow indicates the interface. $SrTiO_3$ was deposited on top of the Dy123 layer to serve as a protection layer during HREM sample preparation.

In figure 5.3 (a) and (b), besides the observed streaks, clear 3D spots are visible as indicated by the arrows. From the intensity and sharpness of the spots one can conclude that on top of the Y123 film many small crystallites are formed. From the horizontal and vertical distance between the spots[IX] a lattice parameter of ~4.3 Å can be determined. From the applied constituents, i.e., Dy, Ba, Cu and O, only cubic cuprite, Cu_2O, can be identified to be responsible for these 3D spots. The lattice parameter of Cu_2O is 4.27 Å, which fits with the observed lattice parameter. The position of the spots revealed that the Cu_2O precipitates are aligned with the [010]Cu_2O//[010]Y123 and [001]Cu_2O//[001]Y123.

Assuming a perovskite stacking sequence, stoichiometric deposition of Y123 on TiO_2 (B-site) terminated $SrTiO_3$ should lead to B-site terminated Y123, e.g., either a CuO_2 plane or the CuO chain layer. Furthermore, a symmetric unit cell with stacking sequence *bulk-BaO-CuO_2-Y-CuO_2-BaO-CuO_x-bulk* leads to the CuO chain layer as the terminating atomic layer. As mentioned earlier, it is expected that the small oxidation power at standard PLD conditions gives rise to an unstable CuO_x chain layer. As a consequence, BaO becomes the terminating atomic layer of Y123 and Cu_2O precipitates are formed.

[IX] Not all spots are observed in the RHEED pattern. Some spots are extinct and, therefore, not visible.

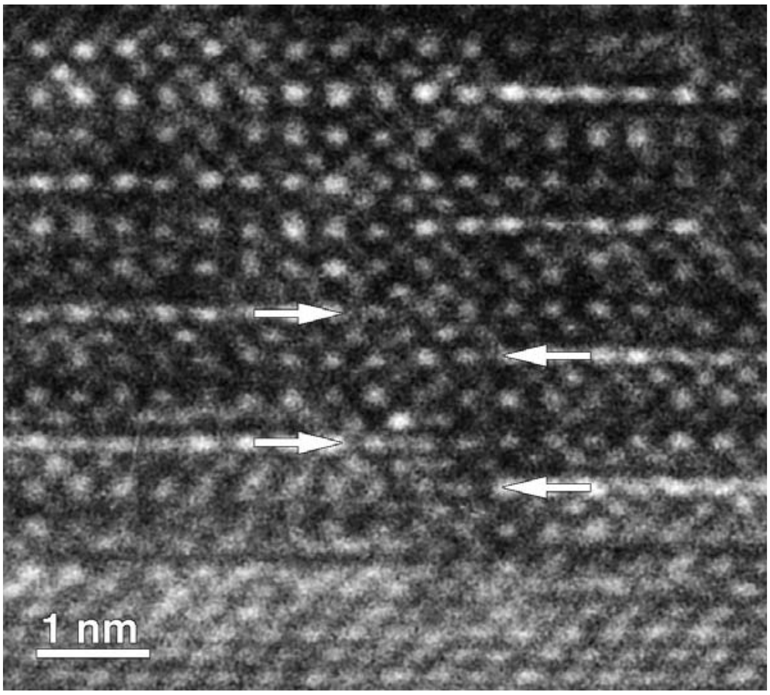

Figure 5.6: HREM image of an anti-phase boundary in Dy123 film on TiO_2 terminated $SrTiO_3$. The arrows indicate the CuO chain layers.

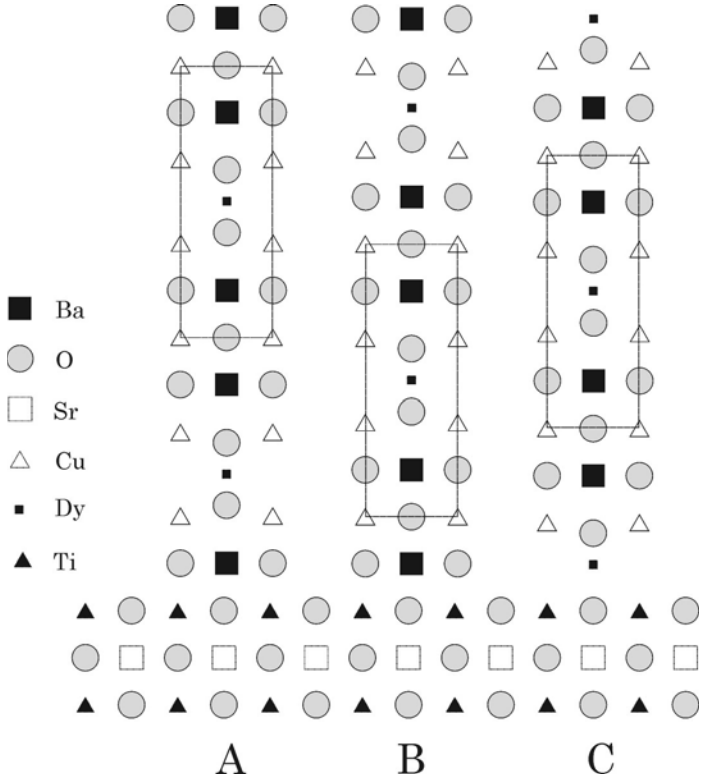

Figure 5.7: Schematic of the three possible perovskite atomic layer stacking sequences of Dy123 on TiO_2 terminated $SrTiO_3$.

To comprehend the RHEED and AFM measurements of the first few unit cell layers on TiO_2 terminated $SrTiO_3$, high-resolution electron microscopy (HREM) was carried out[59]. HREM is performed along the perovskite cube directions; i.e. along [100] or [010] of the RE123 film. Imaging both the film and the substrate under ideal conditions is not straightforward; the lattice mismatch between film and substrate (about 1.6 %) causes local bending of the ultra-thin film. Figure 5.5 shows an overview HREM image of 4 unit cell layers Dy123. No interface dislocations or surface steps in the substrate have been noticed in this overview. The unit cells are clearly visible and the epitaxy is perfect all over the film with [001]Dy123//[001]$SrTiO_3$. The interface between film and substrate is atomically flat and no amorphous or secondary phases were observed.

The most prominent defects that occur are APB's. They start at the substrate-film interface and persist over the total film thickness. The average distance between the APB's is ~20 nm. An enlargement of an APB is shown in figure 5.6.

A perovskite stacking sequence is found at the substrate-film interface, allowing three possible atomic layer sequences at the interface of Dy123 on TiO_2 terminated $SrTiO_3$. These are visualized in figure 5.7. Because the size of a Ba-block (4.14Å) is larger than the size of a Dy-block (3.39Å), the position of the Dy-layer on both sides of the APB can be located. Figure 5.8 shows a detailed HREM image of the interface for a very small sample thickness and a defocus around 25 nm. Image simulations indicate that the cations are imaged as dark dots and that oxygen columns are imaged as bright dots. The substrate-film interface is indicated by two arrowheads in figure 5.8; an APB is present in the middle of the figure, indicated by the vertical arrow.

The atomic layer sequence on both sides of the APB is determined using intensity line scans. Intensity scanning along the vertical [001] direction allows determination of the first atomic layer of the Dy123 film, see insets in figure 5.8. The first atomic layer of the Dy123 film was found to be at the same level on both sides of the APB; excluding a surface step as the reason for the APB formation.

A clear shift of the Dy layer is observed over $R=[00\frac{1}{3}]$, leading to a structural misfit and, unavoidably, two different interface configurations. The structural misfit and the change in interatomic spacing at the APB also cause a relaxation and a slight bending of the atomic (001) planes close to the APB. This is clearly visible in the detailed HREM micrograph in figure 5.6. The interface stacking sequence is different on both sides of the APB. The interface stacking on the left side is determined to be: *bulk substrate-SrO-*TiO_2*-BaO-CuO-BaO-*CuO_2*-Dy-*CuO_2*-BaO-bulk film*. For the stacking of the layers at the interface on the right side the following sequence is found: *bulk substrate-SrO-*TiO_2*-BaO-*CuO_2*-Dy-*CuO_2*-BaO-CuO-BaO-bulk film*. These two interface configurations were observed throughout the complete film. Image simulations for both interface models were performed and the contrast was matched with the experimental images. These simulated images are shown in figure 5.8 as insets.

The third possible interface stacking: *bulk substrate-SrO-TiO*$_2$*-Dy-CuO*$_2$*-BaO-CuO-BaO-CuO*$_2$*-Dy-bulk film* was never observed. Apparently, an interface with BaO as a first layer of the film is more stable than one with Dy as the first layer.

The instability of an interface with Dy as the first atomic layer can be understood by taking into account the co-ordination environment of the Ti^{4+} cations. The *-SrO-TiO*$_2$*-Dy-CuO*$_2$*-* stacking sequence would imply an incomplete square-pyramid polyhedron for the Ti cation whereas it is favorably disposed towards an octahedral co-ordination. The absence of oxygen atoms in the Dy layer also results in an increase of the lattice energy associated with the interface due to repulsion between the highly charged Ti^{4+} and Dy^{3+} cations. As a semiquantitative measure of the lattice energy and hence the stability of different interfaces, one can use the Madelung's constant α. The Madelung energy is the electrostatic contribution to the binding energy of ionic crystals. It should be noted that an absolute value of the electrostatic energy is meaningless for RE123 compounds because of the strong covalent bonding in the (CuO_2) planes. Nevertheless, it is possible to compare α values for different types of interface configurations since the interaction between Ti^{4+}, Dy^{3+}, Ba^{2+} and oxygen can be considered as mostly ionic. The Madelung constant was computed using the Ewald's method of

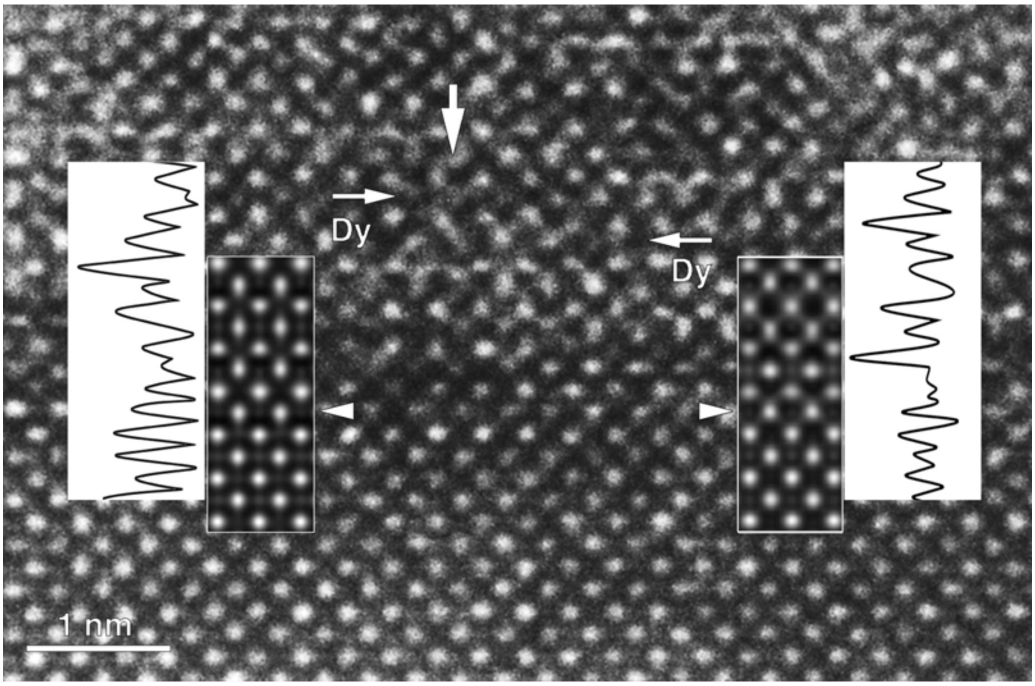

Figure 5.8: HREM image of an APB at the interface region (vertical arrow indicate the APB, the arrowheads indicate the interface). Line scans and image simulations (a focus value of -24 nm and a thickness of 2.4 nm were used for the left part of the image while a thickness of 3.2 nm was used for the right part) are shown as insets.

convergent series with an algorithm described by Popov *et al.*[60]. The charges associated with statistically occupied positions were chosen in accordance with the site occupancies. The unit cell constructed for these calculations consists of one unit cell of Dy123 and one unit cell of $SrTiO_3$. With this model the Madelung constants have been computed for the three possible stacking sequences, depicted in figure 5.7, which contain equal amounts of atomic layers of the same type and differ only by layer sequences. The α value is drastically lower for the interface C ($\alpha = 52.05$) compared to interfaces A ($\alpha = 64.18$) and B ($\alpha = 63.85$). This rough estimate suggests that the C interface is unstable in comparison with the interfaces A and B. Furthermore, similar lattice energies have been found for the interfaces A and B. As a consequence, formation probability of both interfaces is (almost) equal.

5.4.3 Discussion

From the above presented data we can conclude that the initial growth of RE123 on TiO_2 terminated $SrTiO_3$ is dominated by two effects: the unstable terminating CuO chain layer at deposition conditions and the two possible stacking sequences at the substrate-film interface. The first effect will lead to BaO termination and Cu_2O precipitates, while the latter gives rise to the formation of APB's. Both hamper the unit cell layer-by-layer growth. The formation of Cu-rich precipitates on the surface of RE123 has been studied using PLD[61,62], MBE[63] and off-axis sputter deposition[64]. The formation and growth kinetics were especially subject to these studies. Using a light scattering technique[62] together with *ex situ* AFM, it was demonstrated that at the initial stage of Y123 growth on TiO_2 terminated $SrTiO_3$ formation of CuO precipitates occur. These act as a nucleation site for $BaCuO_2$ and CuO by subsequent gettering of Ba and Cu. It was shown that deposition of CuO_x[63] on the surface of Dy123[X] using strong oxidizing conditions[XI] leads to the formation of Cu_2O precipitates, which act as an effective sink for the rest of the deposited CuO_x.

In general it is believed that, independent of the deposition technique, Cu-rich composition during deposition of RE123 will lead to the nucleation of CuO_x precipitates. At the initial growth stage, i.e., the deposition of the first unit cell layer, of Y123 on TiO_2 terminated $SrTiO_3$ the composition can be regarded as Cu-rich because of the BaO termination. In other words, the surplus of CuO_x, which is not incorporated in the first unit cell layer, leads to Cu enrichment. Due to the high reactivity[63] between the nucleated Cu_2O and BaO during subsequent deposition, $BaCu_xO_y$ phases are formed. These stable phases hamper the

---

[X] The terminating atomic plane of the Dy123 film was not determined in this study.

[XI] The MBE system was equipped with an atomic oxygen source.

reincorporation in the growing film. Consequently, the film will be Ba and Cu depleted.

From HREM measurements of Dy123 growth on TiO_2 terminated $SrTiO_3$, the following conclusions can be made:

(1) The substrate-film interface is perovskite like. The first atomic layer on TiO_2 terminated $SrTiO_3$ is BaO.

(2) The stacking sequence at the interface is either *SrO-TiO₂-BaO-CuO-BaO-CuO₂-Dy-CuO₂-BaO-bulk* or *SrO-TiO₂-BaO-CuO₂-Dy-CuO₂-BaO-bulk* resulting in formation of $[00\frac{1}{3}]$ APB's during deposition of the first unit cell layer.

(3) The diffusion length of the RE123 deposit during initial growth is ~20 nm, determined from the average distance between the APB's.

Various authors reported the presence of APB's in thin RE123 films, grown on $SrTiO_3$. However, in these cases the presence of the APB's was attributed to unit cell steps at the substrate. For instance, Dam *et al.*[35] concluded from cross-section TEM analysis that the APB density is closely related to the substrate step density. They observed $[00\frac{1}{3}]$ APB's with average spacing ~10 to 20 nm on $SrTiO_3$ substrates with a vicinal angle of 0.5°[XII].

In our case, however, the density of the APB's is large compared to the density of substrate unit cell steps[XIII], determined from the vicinal angle of the substrate surface[XIV]. From this one can conclude that APB's are formed on the atomically smooth terraces and not only at the substrate steps. Here, APB's are formed by the coalescence of neighboring islands with a different stacking sequence. Consequently, the APB density is found to be larger than the substrate step density.

An APB will be formed at the substrate step if the stacking sequence on both terraces adjacent to the substrate step is identical. On the other hand, APB formation at the substrate step can be prevented by different stacking sequences on adjacent terraces. A large influence of the substrate steps on the growth of RE123 can be expected if the APB density becomes comparable to the substrate

---

[XII] From the vicinal angle (~0.5°) of the used substrate an average terrace length of ~50 nm can be determined.

[XIII] The density of substrate steps, observed in cross-section HREM, depends on the orientation of the step ledges with respect to the crystallographic orientation of the sample during observation. The maximum density is observed if the cross-section HREM sample is cut perpendicular the step ledges.

[XIV] The average terrace width, determined from the vicinal angle (<0.2°), is larger than 120 nm.

step density. This has been observed on substrates with a high vicinal angle by Haage *et al.*[34]. They attributed the presence of the variable stacking sequence to the substrate steps and proposed a model where partial overgrowth at the substrate steps occurs. This overgrowth leads to step flow like growth if the average terrace length of the substrates becomes comparable to or smaller than the surface diffusion length. They found that a vicinal angle larger than 1°[XV] has to be used at typical PLD conditions, since a surface diffusion length of ~20 nm is expected[34].

The initial growth of Dy123 on TiO_2 terminated $SrTiO_3$ can be described qualitatively by the following sequence (see schematic view in figure 5.9):

(1) 2D islands nucleate on the substrate surface until saturation in the density is reached. This density depends on the diffusion length of the deposit.
(2) During subsequent deposition coalescence of the spreading islands occurs. Coalescence of islands with different stacking sequence at the substrate-film interface leads to the formation of $[00\frac{1}{3}]$ APB's. The surface step density is increased because of the height difference (~4Å) between the islands. Consequently, the RHEED intensity is decreased.
(3) After coalescence of islands in the first unit cell layer, 2D unit cell layer-by-layer growth occurs indicated by the RHEED oscillations. The period of the observed oscillations equals the time necessary for deposition of one unit cell layer.

Thus, APB's are not only created at substrate step edges but also on the atomically smooth terraces of the substrate.

As shown, precipitation of Cu_2O and, consequently, BaO (A-site) termination occur during growth of the first RE123 unit cell layer on TiO_2 (B-site) terminated $SrTiO_3$. To avoid precipitation, substrates with SrO (A-site) termination can be an alternative. Here, stoichiometric deposition of RE123 leads to A-site termination and the supplied CuO will be incorporated in the thin film. Hence, precipitation of Cu_2O is prevented. So far, however, no chemical treatments have been reported that produces single SrO terminated $SrTiO_3$ while heat treatment of $SrTiO_3$ usually results in a mixed termination. To obtain SrO termination we deposited a monolayer of SrO on TiO_2 terminated $SrTiO_3$ (see chapter 2 for the experimental details).

[XV] The calculated average terrace length at 1° is 22 nm.

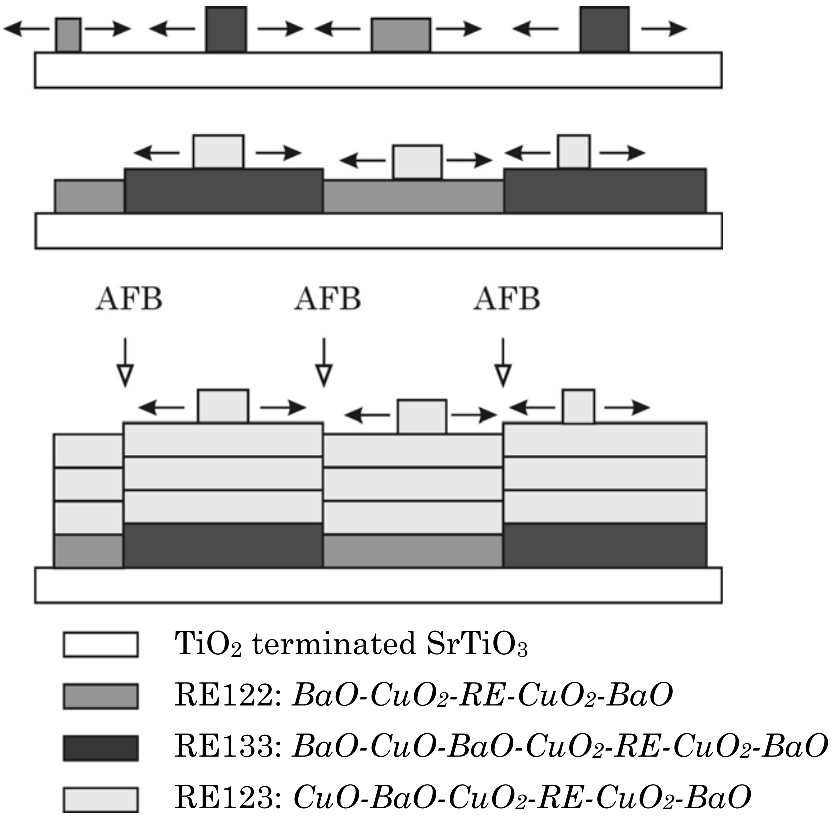

Figure 5.9: Schematic representation of the initial RE123 growth on TiO_2 terminated $SrTiO_3$. Coalescence of islands with different stacking sequence causes formation of anti-phase boundaries (APB's).

The RHEED patterns recorded after growth of SrO and, subsequently, 4 unit cell layers of Y123 are depicted in figure 5.10 (a) and (b), respectively. Now, only streaks, originating from the Y123 layer, can be seen. No indication of Cu_2O formation has been found, i.e., no 3D transmission spots have been observed. During the deposition of Y123 the supplied CuO_x is incorporated in the unit cell layer and A-site termination is preserved. Still a large drop in the RHEED intensity is observed without large recovery indicative for an increased step density, see figure 5.10 (c). In fact, the RHEED intensity resembles the RHEED intensity recorded during growth on TiO_2 terminated $SrTiO_3$. So, no difference in the growth mode is expected. Here, also the occurrence of two stacking sequences is likely, i.e., *bulk substrate-SrO-*TiO_2*-SrO-CuO-BaO-*CuO_2*-Dy-*CuO_2*-BaO-bulk film* and *bulk substrate-SrO-*TiO_2*-SrO-*CuO_2*-Dy-*CuO_2*-BaO-CuO-BaO-bulk film*. Equal nucleation probability at the initial growth leads to an increase in the step density and formation of APB's. From both RHEED and AFM measurements we conclude that the growth mode on SrO terminated $SrTiO_3$ resembles the growth mode on TiO terminated $SrTiO_3$.

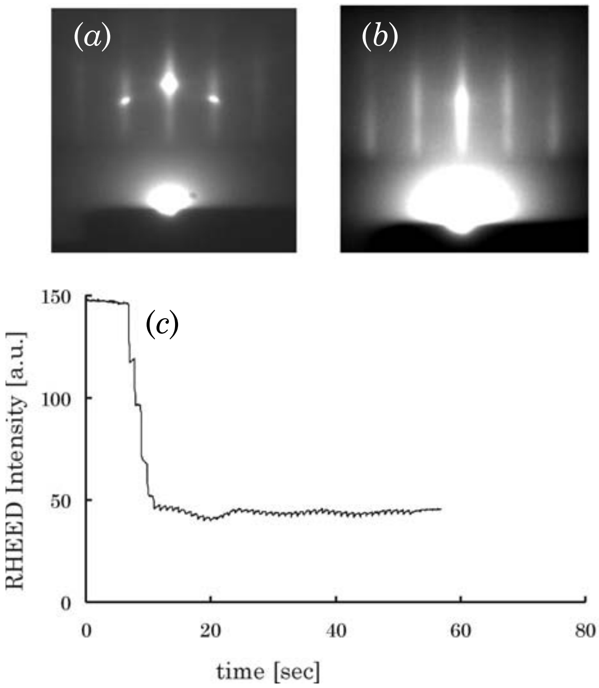

Figure 5.10: RHEED patterns recorded after deposition of 1 ML SrO (a) and, subsequently, 4 unit cell layers of Y123 (b) on TiO_2 terminated $SrTiO_3$ and the specular RHEED intensity recorded during Y123 growth (c).

5.4.4 Manipulating the initial growth of RE123

To avoid precipitation of Cu_2O during the deposition of the first unit cell layer on TiO_2 terminated $SrTiO_3$, stoichiometric deposition is a prerequisite at all stages during the film growth. The cation ratio RE:Ba:Cu of the first unit cell layer should be 1:2:2 or 1:3:3, see figure 5.9, rather then 1:2:3. A 1:3:3 cation ratio, however, leads to the two observed stacking sequences. To avoid the latter we propose to use the 1:2:2 cation ratio.

5.4.4.1 Initial growth of $DyBa_2Cu_2O_x$ on TiO_2 terminated $SrTiO_3$

Deposition was performed using a target with nominal 1:2:2 composition. Figure 5.11 (a) shows an AFM micrograph after deposition of approximately 1 unit cell layer[XVI] using the standard deposition conditions[XVII]. The inset shows the RHEED pattern after deposition. The terrace structure of the substrate is still visible in the AFM micrograph. The terraces consist of coalesced islands with height ~4 Å. The step density is clearly increased and, consequently the 2D spots in the RHEED pattern are somewhat blurred. Since no 3D spots are observed it is expected that nucleation of Cu_2O precipitates is prevented.

[XVI] One unit cell layer of Dy122, unit cell height ~10 Å.

[XVII] Here, the deposition conditions are equal to the conditions used for Dy123 deposition.

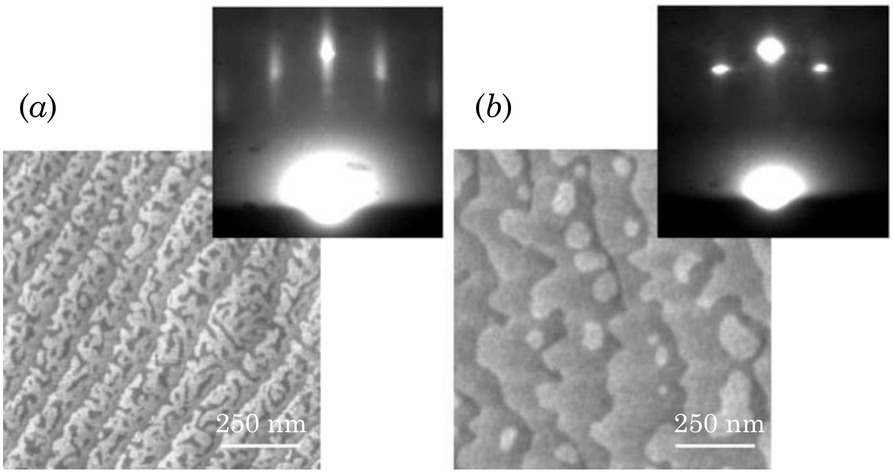

Figure 5.11: AFM micrographs of Dy122 unit cell layer on TiO_2 terminated $SrTiO_3$, at typical deposition conditions for RE123 (a) and optimized deposition conditions (b). The insets show the corresponding RHEED patterns.

The intended stacking sequence is *bulk substrate-SrO-*TiO_2*-BaO-*CuO_2*-Dy-*CuO_2*-BaO*. Deposition of a single RE122 unit cell layer requires exact control of the supplied constituents. First, the amount of deposited material must exactly match to 1 unit cell layer. Second, the ratio between the constituents should be exactly 1:2:2. No improvement in the surface morphology has been observed by adjustment of the amount of deposited material. Excessive deposition leads to a more roughened surface. Obviously, supplying more material with a ratio close to 1:2:2 leads to nucleation of other phases. It is, therefore, expected that off stoichiometric deposition is the cause for the observed morphology. If the stacking sequence of the deposited Dy122 unit cell layer equals *BaO-*CuO_2*-Dy-*CuO_2*-BaO*, depletion of Ba and Cu is most probable. This can also be regarded as a surplus of Dy.

Several attempts were performed to obtain atomically smooth terraces by improving stoichiometry. Especially the energy density in the laser spot, the deposition temperature and pressure have been optimized. Although islands were always found on the terraces and atomic smooth terraces were never observed, the step density is clearly diminished by the optimalization, as shown by clear 2D RHEED spots. Figure 5.11 (b) shows an example of the AFM micrograph and corresponding RHEED pattern of a Dy122 unit cell layer deposited at an energy density of 7 J/cm^2. Just after deposition the film was *in situ* annealed at a temperature of 880 °C for 1.5 h. The ledges of the terraces are roughened through coalescence of islands with the ledges.

5.4.4.2 Initial growth of Dy123 on $DyBa_2Cu_2O_x$

Figure 5.12 shows the RHEED intensity during growth of Dy123 on top of a Dy122 unit cell layer. Clear intensity oscillations are observed indicating 2D

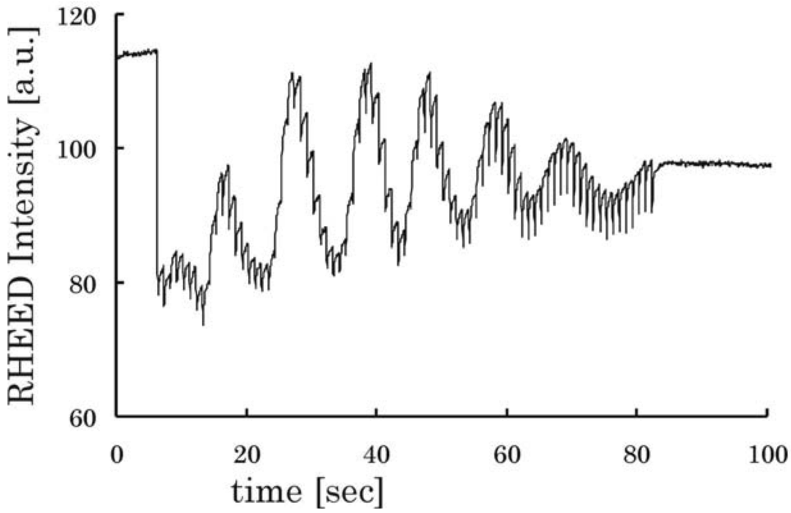

Figure 5.12: Specular RHEED intensity recorded during growth of Dy123 on Dy122.

nucleation and growth of the first unit cell layers. Compared to the initial growth on TiO_2 and SrO terminated $SrTiO_3$ the oscillations are more pronounced. Almost full recovery of the specular RHEED intensity is observed during deposition of the first few unit cell layers. Since the observed intensity is a direct measure of the surface step density, we conclude that no additional roughening takes place during initial growth. During subsequent growth, however, the oscillations are damped and the RHEED intensity decreases, indicating roughening of the surface.

HREM analysis indicates the nucleation and initial growth mechanism to be different compared to Dy123 growth on TiO_2 terminated $SrTiO_3$. No APB's have been observed at the substrate-film interface, see cross-section image in figure 5.13 and HREM cross-section in figure 5.14 (a). However, non-unit cell growth has been observed remote from the interface, visualized by the Burgers vector in the HREM image in figure 5.14 (b).

5.4.4.3 Discussion

As shown, deposition of the first unit cell layer with a cation ratio RE:Ba:Cu = 1:2:2 on TiO_2 terminated $SrTiO_3$ prevents Cu_2O precipitation. Apparently, it also prevents formation of APB's at the substrate-film interface. As discussed, APB's are formed during Dy123 deposition on TiO_2 as well as SrO terminated substrates by the coalescence of domains with different stacking sequence. The stacking sequence of the first unit cell layer in the domains is either *BaO(or SrO)-*CuO_2*-Dy-*CuO_2*-BaO* or *BaO(or SrO)-CuO-BaO-*CuO_2*-Dy-*CuO_2*-BaO*. The first can be considered as Dy122 whereas the latter can be considered as Dy133[XVIII]. Formation

---

[XVIII] Dy133 can be considered as a Dy122 unit cell on top of a BaCuO block.

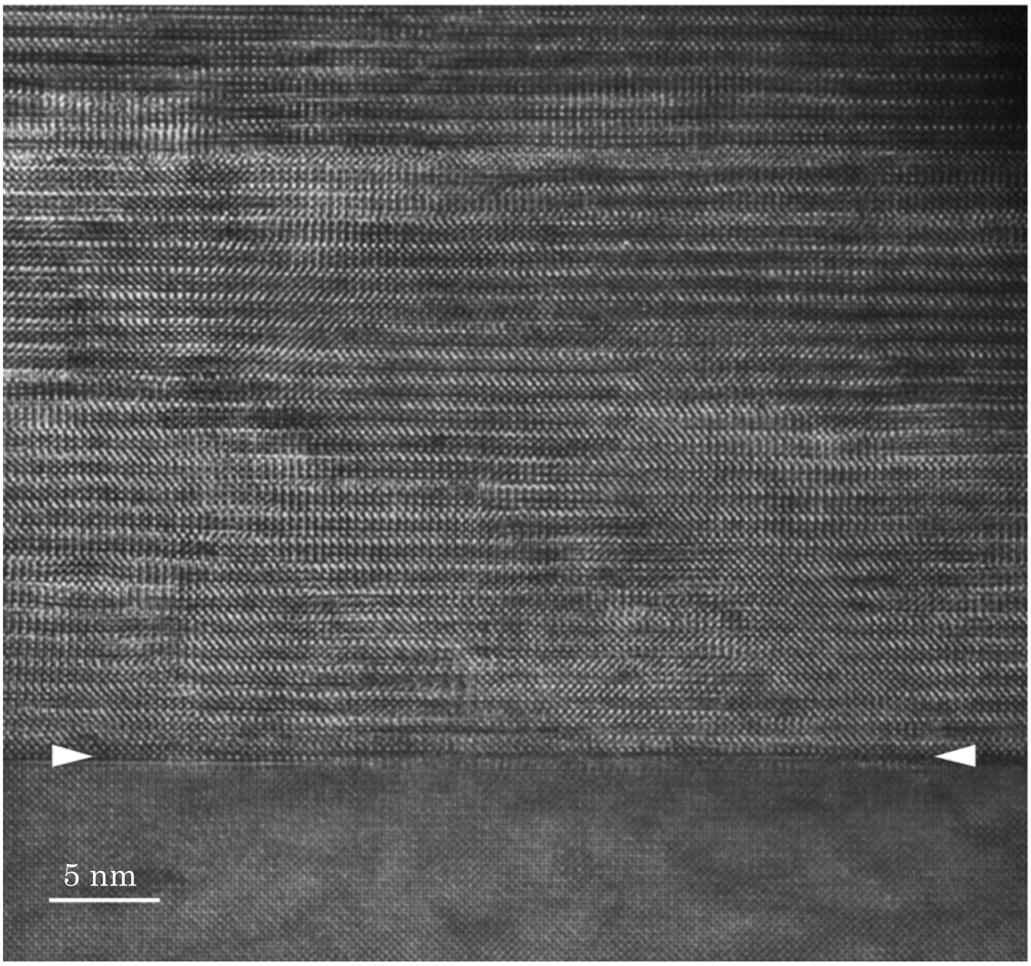

Figure 5.13: Overview cross-section image of Dy123/Dy122 deposited on TiO_2 terminated $SrTiO_3$. The arrowheads indicate the substrate-film interface.

of the Dy133 domains is suppressed in the case of Dy122 deposition, leading to one stacking sequence, i.e., *bulk substrate-SrO-TiO_2-BaO-CuO_2-Dy-CuO_2-BaO-bulk film*. Subsequently, formation of APB's is prevented.

5.5 Conclusions

Although in many studies a perovskite stacking sequence has been found at the interface of RE123 and $SrTiO_3$, the determination of the terminating atomic layer of the $SrTiO_3$ substrate as well as the starting atomic layer of RE123 remained ambiguous. Determination of the starting atomic layer with *ex situ* techniques like HREM and XSW requires the terminating layer of the substrate to be predetermined. The termination of $SrTiO_3$, however, can be SrO, TiO_2 or a mixture of both, depending on the surface treatment. Since most of the studies were performed using thermally treated substrates, a mixed termination has to be

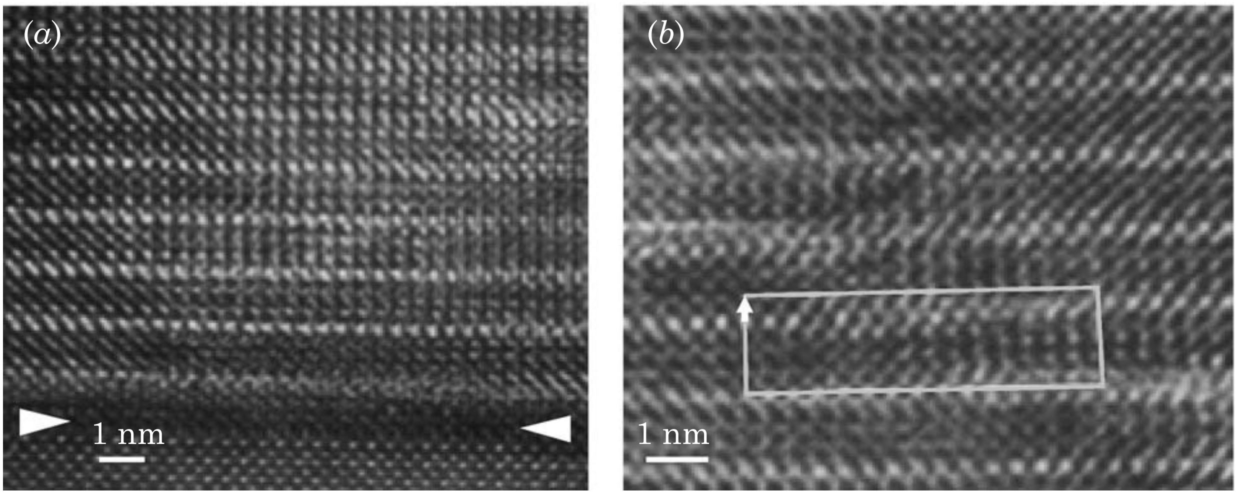

Figure 5.14: Cross-section HREM images of the film-substrate interface of Dy123/Dy122 deposited on TiO_2 terminated $SrTiO_3$ (a). Non-unit cell growth during deposition of Dy123, indicated by the Burgers vector (b).

expected. Reliable determination of the first atomic layer is, therefore, not straightforward.

The terminating atomic layer of RE123 has been studied extensively using *in situ* and *ex situ* measurements. *Ex situ* determination usually requires surface cleaning by heat treatment and/or ion beam treatments. Modification of the surface is likely. Consequently, the measured termination layer may differ from the terminating layer during growth. Both CuO_x and BaO have been found as the terminating layer. The growth conditions, especially the oxidation power during growth, determines the thermodynamically stable terminating layer at these conditions. Mostly, CuO_x termination is found at high oxidation power using ozone, atomic oxygen or other activated oxygen, whereas BaO is found at lower oxidation power using molecular oxygen. At standard PLD conditions the terminating atomic layer is BaO. Consequently, Cu_2O precipitation occurs during initial growth on TiO_2 terminated $SrTiO_3$ at these conditions.

Two methods have been successfully applied to avoid Cu_2O precipitation. In the first method, i.e., using SrO terminated $SrTiO_3$ substrates, A-site termination is preserved during deposition of the first unit cell layer and, hence, all CuO is incorporated in the thin film. The second method ensures “stoichiometric” deposition during the first unit cell layer. The exact amount of material, needed for one unit cell layer, is supplied. Since both the starting and terminating atomic layer of the first unit cell layer is BaO, a cation ratio of RE:Ba:Cu = 1:2:2 has to be used.

Ultra-thin films of Dy123 prepared by PLD on TiO_2-terminating $SrTiO_3$ apparently contain numerous APB’s. Such boundaries were already observed in RE123 thin films and often related to unit cell steps on the substrate. The vicinal angle of the substrate used in this study was less than 0.2°, implying that the minimum width of a substrate terrace is 112 nm. Since HREM showed that the average width of an anti-phase domain is of the order of 20 nm, unit cell steps at the substrate cannot be the only reason for the formation of APB’s, which are unavoidably created during the growth of the film. As a consequence two different stacking sequences at the interface are found. This causes a structural and chemical misfit and will lead to the formation of APB’s, which will negatively influence the superconducting properties of the film. Formation of APB’s is successfully prevented by the deposition with cation ratio RE:Ba:Cu =1:2:2 of the first unit cell layer.

References

1 T.L. Hylton and M.R. Beasley, *Phys. Rev. B* **41**, 11669 (1990)

2 B. Dam, J.M. Huijbrechtse, F.C. Klaassen, R.C.F. van der Geest, G. Doornbos, J.H. Rector, A.M. Testa, S. Freisem, J.C. Martinez, B. Stäuble-Pümpin and R. Griessen, *Nature* **399**, 439 (1999)

3 M. McElfresh, T.G. Miller, D.M. Schaefer, R. Reifenberger, R.E. Muenchausen, M. Hawley, S.R. Foltyn and X.D. Wu, *J. Appl. Phys.* **71**, 5099 (1992)

4 T. Haage, J. Zegenhagen, J.Q. Li, H.-U. Habermeier, M. Cardona, CH. Joos, R. Warthman, A. Forkl and H. Kronmüller, *Phys. Rev. B.* **56**, 8404 (1997)

5 T. Terashima, Y. Bando, K. Iijima, K. Yamamoto, K. Hirata, K. Hayashi, K. Kamigaki and H. Terauchi, *Phys. Rev. Lett.* **65**, 2684 (1990)

6 J.G. Wen, C Traeholt and H.W. Zandbergen, *Physica C* **205**, 354, (1993)

7 G. Koster, B.L. Kropman, G.J.H.M. Rijnders, D.H.A. Blank and H. Rogalla, *Appl. Phys. Lett.* **73**, 2920 (1998)

8 M. Nakanishi, H. Hashizume, T. Terashima, Y. Bando, O. Michikami, S. Maeyama and M. Oshima, *Phys. Rev. B* **48**, 10524 (1993)

9 J. Zegenhagen, T. Siegrist, E. Fontes, L.E. Berman and J.R. Patel, *Solid State Comm.* **93**, 763 (1995)

10 S. Tanaka, T. Nakamura, H. Tokuda and M. Liyama, Appl. Phys. Lett. **62**, 3040 (1993)

11 T. Nakamura, S. Tanaka and M. Liyama, Appl. Phys. Lett. **66**, 3362 (1995)

12 K. Shimura, Y. Daitoh, Y. Yano, T. Terashima, Y. Bando, Y. Matsuda and S. Komiyama, *Physica C* **228**, 91 (1994)

13 B. Stäuble-Pümpin, V.C. Matijasevic, B. Ilge, J.E. Mooij, W.J.A.M. Peterse, P.M.L.O. Scholte, F. Tuinstra, H.J. Venvik, D.S. Wai, C. Træholt, J.G. Wen and H.W. Zandbergen, *Phys. Rev. B* **52**, 7604 (1995)

14 V.C. Matijasevic, B. Ilge, B. Stäuble-Pümpin, G. Rietveld, F. Tuinstra and J.E. Mooij, *Phys. Rev. Lett.* **76**, 4765 (1996)

15 H. Behner, K. Rührnschopf, G. Wedler and W. Rauch, *Physica C* **208**, 419 (1993)

16 S.J. Pennycook, M.F. Chisholm, D.E. Jesson, D.P. Norton, D.H. Lowndes, R. Feenstra, H.R. Kerchner and J.O. Thomson, *Phys. Rev. Lett.* **67**, 765 (1991)

17 M. Badaye, W. Ting, K. Fukushima, N. Koshizuka, T. Morishita and S Tanaka, *Appl. Phys. Lett.* **67**, 2155 (1995)

18 M Badaye, J.G. Wen, K Fukushima, N Kohizuka, T, Morishita, T. Nishimura and Y Kido, *Supercond. Sci. Technol.* **10**, 825 (1997)

19 M. Badaye, F. Wang, Y. Kanke, K. Fukushima and T. Morishita, *Appl. Phys. Lett.* **66**, 2131 (1995)

20 Z. Liu, M. Badaye, S. Ogota and T. Morishita, *Appl. Surf. Sci.* **115**, 180 (1997)

21 J. Rao, T. Morishita, *Physica C* **291**, 223 (1997)

22 J.M. Huijbregtse, J.H. Rector, B. Dam, *Physica C* **351**, 183 (2001)

23 T. Haage, J. Zegenhagen, H.-U. Habermeier, C. Cardona, *Phys. Rev. Lett.* **80**, 4225 (1998)

24 M. Kawasaki and M. Nantoh, *MRS Bulletin* **IX**, 33 (1994)

25 G. Frank, Ch. Ziegler and W. Göpel, *Phys. Rev. B* **43**, 2828 (1991)

26 G.J.H.M. Rijnders, G. Koster, D.H.A. Blank and H. Rogalla, *IEEE Transactions on Appl. Supercond.* **9**, 1547 (1999)

27 R.C. Baetzhold and J. Mir, J. of Cryst. Growth **135**, 145 (1994).

28 J.G. Lopez, D.H.A. Blank, H. Rogalla and J. Siejka, *Physica C* **307**, 298 (1998)

29 T. Haage, J. Zegenhagen, Ch. Jooss, R. Warthmann, J.Q. LI, H.-U. Habermeier, C. Cardona, *Physica C* **282-287**, 557 (1997).

30 T. Haage, J. Zegenhagen, C. Cardona, H.-U. Habermeier, *J. of Alloys and Compounds* **251**, 23 (1997)

31 F. Wellhöfer, P. Woodall, D.J. Norris, S. Johnson, D. Vassiloyannis, M. Aindow, M. Slaki and C.M. Muirhead, *Appl. Surf. Sc.* **127-129**, 525 (1998)

32 J. Kim, D.B. Chrisey, J.S. Horwitz, M.M. Miller and C.M. Gilmore, *J. Mater. Res.* **15**, 596 (2000).

33 M.G. Norton, C.B. Carter, *J. Cryst. Growth* **110**, 641 (1991)

34 T. Haage, H.-U. Habermeier, J. Zegenhagen, *Surf. Sci.* **370**, L158 (1997).

35 B. Dam, C. Træholt, B. Stäuble-Pümpin, J. Rector and D,G. de Groot, *J. of Alloys. and Compounds.* **251**, 27 (1997)

36 M. Yeadon, M. Aindow, F. Wellhöfer and J.S. Abell, *J. Cryst. Growth.* **172**, 145 (1997)

37 J. Kim, D.B. Chrisey, C.M. Gilmore and J.S. Horwitz, *Supercond. Sci. Technol.* **13**, 417 (2000)

38 X.-Y. Zheng, D.H. Lowndes, S. Zhu, J.D. Budai and R.J. Warmack, *Phys. Rev. B* **45**, 7584 (1992)

39 J.-L. Maurice, O. Durand, M. Drouet and J.-P. Contour, *Thin Solid Films* **319**, 211 (1998)

40 I.A. Ovid'ko, *J.Phys: Condens. Matter* **13**, L97 (2001)

41 S.J. Pennycook, M.F. Chisholm, D.E. Jesson, R. Feenstra, S. Zhu, X.Y. Zheng and D.H. Lowndes, *Physica C* **202**, 1 (1992)

42 A. Abert, J.P. Contour, A. Défossez, D. Ravelosona, W. Schwegle and P. Ziemann, *Appl. Surf. Sc.* **96-98**, 703 (1996)

43 H.Y. Zhai and W.K. Chu, *Appl. Phys. Lett.* **76,** 3469 (2000)

44 D. Hüttner, O. Meyer, J. Reiner and G. Linker, *Appl. Phys. Lett.* **66**, 1273, (1995)

45 T.-S Gau, S.-L Chang, H.-H. Hung, C.-H. Lee, T.-W. Huang, H.-B. Lu, S.-J. Yang and S.-E Hsu, *Appl. Phys. Lett.* **65**, 1720 (1994)

46 L.X. Cao, J. Zegenhagen, E. Sozontov and M. Cardona, *Physica C* **337**, 24 (2000)

47 D.H. Lowndes, X.-Y Zheng, S. Zhu, J.D. Budai and R.J. Warmack, *Appl.Phys. Lett.* **61**, 852 (1992)

48 M.C.Foote, B.B. Jones, B.D. Hunt, J.B. Barner, R.P. Vasquez and L.J. Bajuk, *Physica C* **201**, 176 (1992)

49 B. Dam, J. Rector, M.F. Chang, S. Kars, D.G. de Groot and R. Griessen, *Appl. Surf. Sc.* **86**, 13 (1995)

50 R.I. Tomov, V.P. Manolov, P.A. Atanasov, V.N. Tsaneva, D.G. Ouzounov and V.I. Tsanev, Physica C 274, 187 (1997)

51 R.H. Hammond and R. Bormann, *Physica C* **162-164**, 703 (1989)

52 A. Gupta, B.W. Hussey and M.Y. Chern, *Physica C* **200**, 263 (1992).

53 B. Dam, J.H. Rector, M.F. Chang, S. Kars, D.G. de Groot and R. Griessen, *Appl. Phys. Lett.* **65**, 1581 (1994)

54 B. Dam, J.H. Rector, J. Johansson, S. Kars and R. Griessen, *Appl. Surf. Sc.* **96-98**, 679 (1996)

55 M. Murakami, M.Morita, K.Doi, K.Miyamoto etc, *Jpn. J. Appl. Phys.* **28**, L399 (1989)

56 B. Dam, J.H. Rector, J.M. Huijbregtse and R. Griessen*, Physica C* **296**, 179 (1998)

57 B. Dam, B. Stäuble-Pümpin, *J. of Mat. Sc.*, **9**, 217 (1998)

58 B. Dam, J.H. Rector, J. Huijbrechtse and R. Griessen, *Physica C* **282-287**, 559 (1997)

59 S. Bals, G. Rijnders, D.H.A. Blank and G. Van Tendeloo, *Physica C* **355**, 225 (2001)

60 S.G. Popov and V.A. Levitzky, *Zh. Phys. Khim (Russ.) LV* **87**, 87 (1981)

61 J.P.Gong, M. Kawasaki, F. Fujito, R. Tsuchiya, M. Yoshimoto and H. Koinuma, *Phys. Rev. B* **50**, 3280, (1994)

62 N. Kanda, M. Kawasaki, T. Kitajima, H. Koinuma, *Phys. Rev. B* **56**, 8419, (1997)

63 J-P. Locquet, Y. Jaccard, C. Gerber and E. Mächler, *Appl. Phys. Lett.* **63**, 1426 (1993)

64 Z. Han, T.I. Selinder and U. Helmersson, *J. Appl. Phys.* **75**, 2020 (1994)

Chapter 6

Sub-unit cell layer epitaxy of $YBa_2Cu_3O_{7-\delta}$

6.1 Introduction

As discussed in the previous chapter, the initial growth of $REBa_2Cu_3O_{7-\delta}$ (RE123) on $SrTiO_3$ during pulsed laser deposition (PLD) is affected by the nucleation of islands with different atomic layer stacking sequences[1] at the substrate-film interface. This leads to the formation of anti-phase boundaries (APB's) and to increased roughness of the film surface. Control of the stacking sequence is used to prevent formation of APB's and roughening during the initial stage of growth. In fact, unit cell layer-by-layer growth is observed during deposition of the first few unit cells. During subsequent deposition, however, 3D island growth is observed due to stress relaxation mechanisms.

The resulting surface morphology of the thin films hampers the application in planar multilayer devices. The very small coherence length in RE123 (or cuprate superconductors in general) determines the electrical properties of the interfaces in these heterostructures. Interfaces must, therefore, be controlled and engineered on an atomic level. For this, atomically smooth surfaces and interfaces are a prerequisite. Because the film surface morphology is a direct product of the growth process, control of the growth process is necessary. In this chapter an alternative deposition scheme for the growth of $YBa_2Cu_3O_{7-\delta}$ (Y123) will be addressed. Here, sub-unit cell layers are grown using pulsed laser *interval* deposition (PLiD)[2], see chapter 3 for details. The resulting crystallinity and surface morphology of the thin film as well as their electrical properties will be discussed.

6.2 Deposition schemes

In epitaxial growth of ionic oxides, the growth unit is generally charge neutral and is determined by the ionic bond character in the different atomic layers. Depending on the energetically most favorable growth unit, three different growth methods can be distinguished[3]:

(1) Atomic layer epitaxy (ALE)
(2) Molecular layer epitaxy (MLE)
(3) Block layer epitaxy (BLE)

The first method is mostly used for metals and semiconductors while the second is generally applied for (complex) oxides. In atomic layer-by-layer molecular beam epitaxy (ALL-MBE),[5] one or more species are deposited *simultaneously* until the desired phase is formed. The ratio of the different supplied constituents can be controlled with high accuracy and is chosen such that formation of secondary

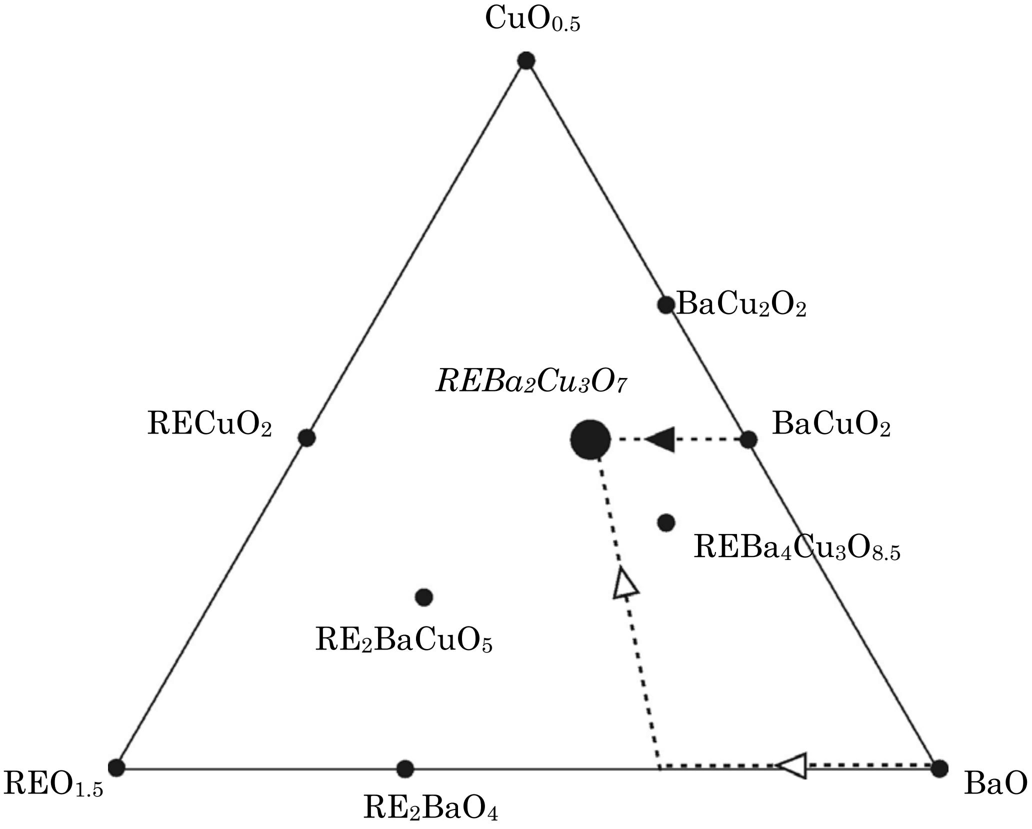

Figure 6.1: Phase diagram of the RE-Ba-Cu-O system[4] at deposition conditions including proposed sequence by Loquet et al.[7] (open arrowheads) of BLE growth of Dy123 using MBE. The sequence, used in the sub-unit cell layer epitaxy of Y123 described in this thesis, is indicated by the closed arrowhead.

phases is avoided. The growth is, therefore, controlled on an atomic level. The term atomic layer-by-layer is, in the case of deposition of complex oxides, somewhat misleading since usually molecular layers, not atomic layers, are deposited. In fact this growth technique could be better considered as MLE. The growth of $SrTiO_3$, $SrRuO_3$ and RE123 by PLD, shown in previous chapters, are other examples of MLE. Constituents are supplied simultaneously through stoichiometric transfer from target to substrate.

In BLE,[6] blocks are deposited *sequentially* and are allowed to react with each other until the desired compound is formed. A block is any amount of material or compound and is not necessarily stable. The main advantage of this method is the controlled reaction path: the sequence of the deposited blocks is chosen such that reaction between the blocks only leads to formation of the desired phase without stable intermediate phases. Nucleation of the desired phase is initiated after deposition of all the necessary constituents, preventing uncontrolled local nucleation, subsequent lateral growth and island coalescence. Note that the deposition temperature has to be sufficiently high, since inter-diffusion is necessary to form the desired phase. Employing MBE, Locquet *et al.*[7] used this method to grow $DyBa_2Cu_3O_{7-\delta}$ (Dy123) thin films on $SrTiO_3$ at 700 °C in a mixture of atomic and molecular oxygen. Typically, blocks of BaO (2 ML), DyO (1ML) and CuO (3 ML) were deposited, see the reaction path in the phase diagram depicted in figure 6.1. Formation of the Dy123 phase starts after deposition of the CuO block, indicated by the appearance of clear RHEED streaks.

Another BLE method is solid-phase epitaxy. Hussey *et al.*[8,9] used this method to grow Y123 thin films by *sequential* PLD from separate precursor oxide targets. Two oxide pairs, i.e., YBa_2O_x/CuO and $Y_2Cu_2O_5$/$BaCuO_2$ were investigated at standard deposition conditions for Y123. In their case an oxygen pressure of 27 Pa and a substrate temperature of 750 °C was used. Formation of Y123 was observed due to intermixing and reaction of species deposited from the two targets. At the deposition conditions, fast[I] intermixing was observed over a wide thickness range of the individual component layers. Epitaxial nucleation of the Y123 phase was observed at the substrate interface due to grain-boundary diffusion of the second precursor species through the first precursor oxide layer. The initial nuclei act as a template for subsequent epitaxial growth of the Y123 phase during deposition of the second precursor until the entire first oxide layer is consumed. Above the critical thickness, approximately 100 nm[II] for the individual oxide layers, the intermixing was found to be insufficient for Y123 formation.

Inter-diffusion and reaction between the applied constituents is necessary to form the desired phase in most of the deposition schemes for complex oxides.

[I] The time scale for inter-diffusion and reaction was estimated to be ~10-100 ms.

[II] A quartz crystal monitor was used to measure the deposition rate of each individual constituent.

Either the constituents are supplied *simultaneously*, as in the case of MLE, or *sequentially*, in the case of BLE. In the latter case, the reaction between the constituents as well as the nucleation of the desired phase could be controlled.

As shown in the previous chapter, nucleation and subsequent growth of RE123 with two different stacking sequences occurs on TiO_2 terminated $SrTiO_3$ using PLD at standard deposition conditions. Control of the stacking sequence by deposition of a nominal 1:2:2 composition of the first unit cell layer is successfully applied to prevent the different stacking sequences and the concomitant initial roughening. Roughening of thicker films by formation of 3D islands is, however, still observed due to the lattice mismatch[10,11,12,13,14,15] between film and substrate[III]. The size of the islands and, thus, the roughness of the film depend on the surface diffusion and are, therefore, kinetically determined. Lower growth temperature[16] can be used to decrease the surface diffusion and, consequently, the island size and the surface roughness. High deposition temperatures are, however, necessary to obtain epitaxial growth of a stable RE123 phase and cannot be used to minimize the film surface roughening[IV]. The kinetic energy of the impinging adatoms affects the surface diffusivity in PLD more effectively and has been used to change the growth mode. Depending on the surface diffusivity either spiral growth or 2D nucleation and growth is observed.

Although the RE123 growth mode can be changed during PLD, roughening of the film surface is not sufficiently decreased by adjustment of the deposition conditions. To obtain further improvement, a different deposition method of the RE123 is necessary, satisfying following requirements:

(1) Controlled stacking sequence during nucleation and subsequent growth.
(2) Epitaxial growth with c-axis perpendicular to substrate surface.
(3) Growth of a stable phase.
(4) Roughening originating from stress relaxation mechanisms in heteroepitaxial growth should be prevented or minimized.

These requirements can be fulfilled using an alternative deposition scheme by sequential deposition of sub-unit cell layers, i.e., $BaCuO_x$ and $RECuO_x$, using pulsed laser interval deposition (PLiD). This method has been successfully applied for the preparation of the $CuBa_2(Sr_xCa_{1-x})_nCu_{n-1}O_y$ compound, by fabrication of layered structures by sequential deposition[17] of $BaCuO_x$ and $(Sr_xCa_{1-x})CuO_y$.

[III] During heteroepitaxy of RE123, pseudomorphic growth is observed until a critical thickness is reached, see chapter 3 and 5. At larger film thickness, the substrate-film interface energy cannot compensate for the increased elastic energy and strain relaxation occurs. As a result, (coherent) 3D islands form.

[IV] At lower deposition temperatures, also a-axis growth is observed, which should be avoided.

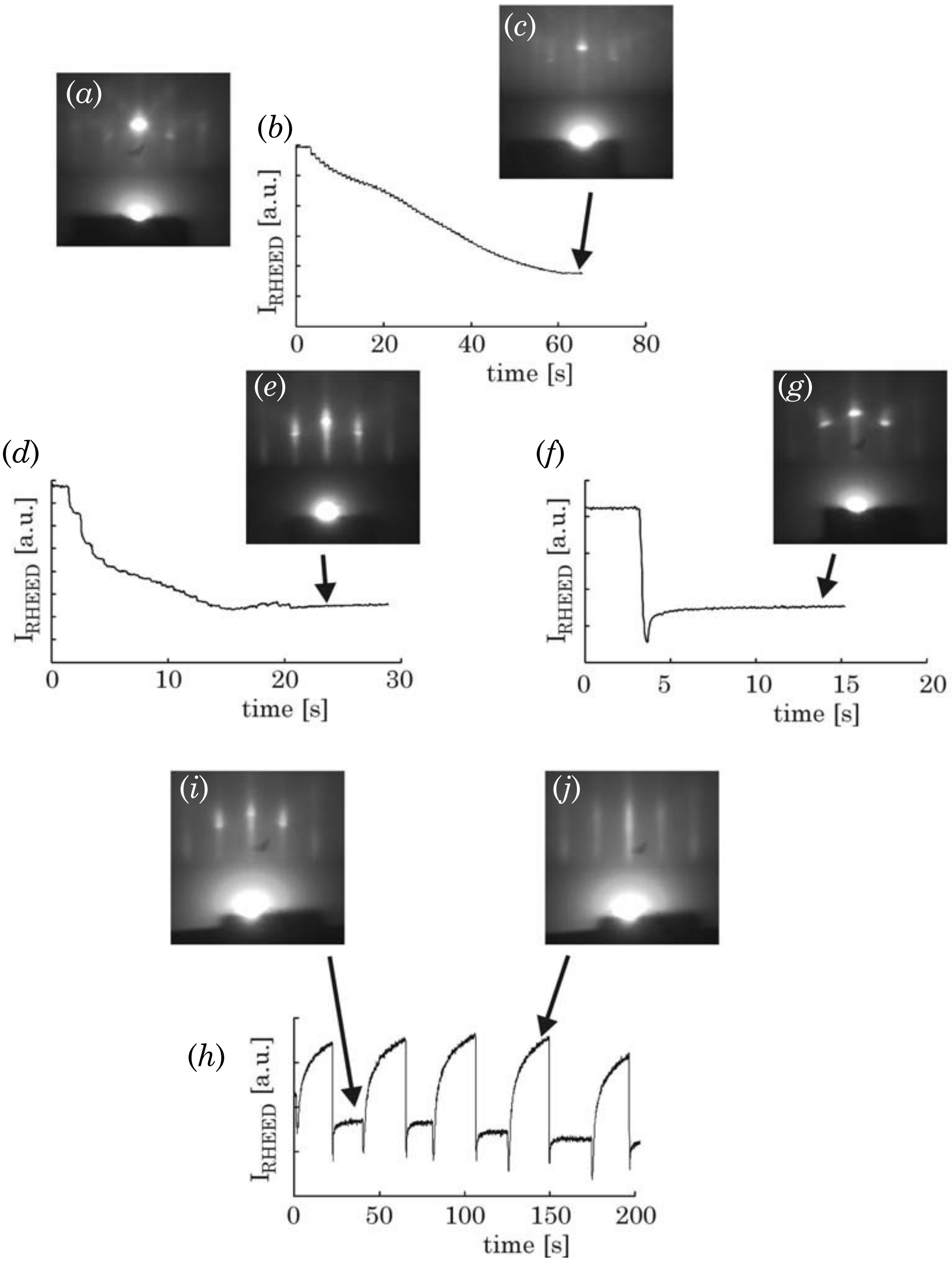

Figure 6.2: RHEED patterns after deposition and intensity variations during deposition of:
SrO: 10 pulses @ 50 Hz, 4 Pa of oxygen, T =800°C (a),
$YCuO_x$: 60 pulses @ 2 Hz (b) and (c),
$BaCuO_x$: 20 pulses @ 1 Hz (d) and (e),
$BaCuO_x$, 20 pulses @ 50 Hz (f) and (g).
Sub-unit cell layer-by-layer epitaxy of 5 ml Y123 (h): $BaCuO_x$, 20 pulses @ 50 Hz (i) and $YCuO_x$, 56 pulses @ 50 Hz (j).
Deposition conditions for $BaCuO_x$ and $YCuO_x$: 14 Pa of oxygen, T =600 °C,
(b) and (d) using “standard” PLD, (f) and (h) using PLiD.

Note that this deposition scheme is not comparable to the BLE methods mentioned above, since no inter-diffusion is necessary between the stable sub-unit cell layers and the growth temperature can, therefore, be low, provided that the sub-unit cell layers can be epitaxially grown at these low temperatures.

6.3 Sub-unit cell layer epitaxy of $YBa_2Cu_3O_{7-\delta}$

6.3.1 Deposition procedure

Sub-unit cell layer epitaxy of Y123 films is applied by sequential deposition of two $BaCuO_x$ unit cell layers and one $RECuO_x$ unit cell layer. To impose layer-by-layer growth, we applied PLiD. For this to be successful, the growth rate, i.e., the number of pulses needed to complete one unit cell layer of the individual oxides, must be known. This is feasible by realtime monitoring of RHEED intensity oscillations during standard PLD, if the growth mode is unit cell layer-by-layer. Using standard PLD, however, $BaCuO_x$ as well as $YCuO_x$ do not exhibit this growth mode. Figure 6.2 (b) and (d) show typical RHEED intensity variations during growth of $YCuO_x$ and $BaCuO_x$ on SrO[V] terminated $SrTiO_3$ using a pulse repetition rate of 2 and 1 Hz, respectively. The deposition conditions are similar to those used for deposition of Y123 from stoichiometric targets, see chapter 5, except for the deposition temperature. The required tetragonal $BaCuO_x$ phase could only be stabilized by the substrate at relatively low temperatures, i.e., 600 °C, which also limits the growth temperature of $YCuO_x$. At this temperature, an exponential decay in the RHEED intensity has been observed during deposition of $YCuO_x$, indicative for a roughened surface. The reason for this roughening is either island growth due to the lattice mismatch or that the desired structure cannot be stabilized by SrO terminated $SrTiO_3$. The latter assumption is likely, since faint streaks are observed in the RHEED pattern, corresponding to a different phase, probably $Y_2Cu_2O_5$[18].

A large drop in the RHEED intensity is also observed during deposition of $BaCuO_x$. Although epitaxial growth of the desired phase occurs, indicated by the in-plane lattice parameter determined from the RHEED pattern[VI] in figure 6.2 (e), roughening by 3D island growth takes place due to stress relaxation[VII]. Still, maxima are observed in the RHEED intensity variations and the corresponding

---

[V] One monolayer of SrO was deposited on TiO_2 terminated $SrTiO_3$, see chapter 2 for the experimental details.

[VI] The lattice constant is comparable to that of $SrTiO_3$.

[VII] Due to the large size of the Ba ion, i.e., 1.42 Å, a considerable compressive stress is to be expected in the epitaxial, tetragonal $BaCuO_x$ film on $SrTiO_3$. No bulk lattice data is available since tetragonal $BaCuO_x$ is not stable in bulk.

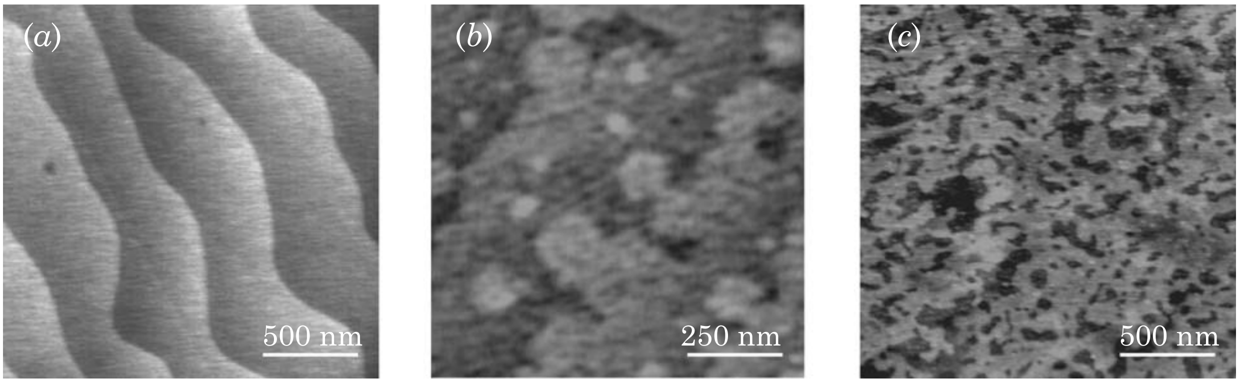

Figure 6.3: AFM micrographs after deposition at 600 °C of 1 (a) and 20 unit cell layers of Y123 before (b) and after (c) subsequent in situ anneal at 800 °C in high oxygen pressure.

periods can be used to estimate the growth rate.[19] Interval deposition is optimized for the growth of a $BaCuO_x$ stack consisting of two unit cell layers[VIII] by observation of the intensity recovery, applying different numbers of pulses. The optimum number of pulses is found at the maximum RHEED intensity after deposition. For the above-mentioned deposition condition an optimum value of 20 pulses at a pulse repetition rate of 50 Hz was determined, see figure 6.2 (f). The corresponding RHEED pattern shows clear 2D dots, indicative of a smooth surface.

A different procedure has been performed for optimizing PLiD of $YCuO_x$, since it is not stabilized by the substrate at the used deposition conditions. The optimum number of pulses was determined by monitoring the RHEED intensity during deposition of a number of Y123 unit cell layers, using the proposed growth method. The number of pulses for $BaCuO_x$ is kept constant, while the number of pulses for $YCuO_x$ is varied. The recovery of the RHEED intensity is found to be very sensitive for the number of $YCuO_x$ deposition pulses. An optimum number of pulses, i.e., at maximum RHEED intensity, of 56 (@50 Hz) is found for $YCuO_x$. Figure 6.2 (h) shows the RHEED intensity during deposition of five Y123 unit cell layers using the optimum number of pulses. After deposition of $BaCuO_x$, clear spots are observed in the RHEED pattern, whereas streaks are observed after deposition of $YCuO_x$, see figure 6.2 (i) and (j), respectively. At the used electron diffraction condition, a larger RHEED intensity is found after deposition of the $YCuO_x$ unit cell layer.

[VIII] It is found that stable $BaCuO_x$ growth proceeds in double unit cell layers and not in single unit cell layer during PLD[19].

6.3.2 Thin film properties

6.3.2.1 Surface morphology

The surface morphology of one Y123 unit cell layer, fabricated by interval deposition of two $BaCuO_x$ and one $YCuO_x$ unit cell layers, is shown in the AFM micrograph depicted in figure 6.3 (a). The initial substrate morphology is clearly visible with terrace step heights of the $SrTiO_3$ unit cell, indicating layer-by-layer growth of the sub-unit cell layers. After deposition of 20 Y123 unit cell layers, the imprint of the substrate morphology is still visible, although the ledges are roughened and the terraces consist of small islands, see figure 6.3 (b). The height differences of the ledges as well as the islands are ~4 Å. The appearance of the small islands could be a direct result of the interval deposition method, if the amount of deposited material deviates from the required amount of material needed to complete one unit cell layer. Small deviations arise from the fact that only an integer number of pulses[IX] can be applied as well as fluctuations of the pulse deposition rate[X]. Figure 6.3 (c) shows the surface morphology after an *in situ* anneal step at a temperature of 800 °C and high oxygen pressure, typically 0.5 atm. After the anneal step, the maximum step height is ~12Å, comparable to the c-axis lattice parameter of Y123, and indicates recrystallization of the film surface.

6.3.2.2 Electrical properties

The as deposited films, i.e., at 600 °C and oxygen pressure of 14 Pa, show a high resistance[XI] of typically kΩ's at room temperature, no superconducting transition has been observed above 4.2 K. Superconducting films could only be obtained after the (*in situ*) anneal step.

Figure 6.4 shows the dependence of the ratio $BaCuO_x/YCuO_x$, given in number of pulses, on the resistance during cooling from room temperature to 4.2 K. The resistance at room temperature is given in table 6.1. As shown, changing the number of pulses for one unit cell layer of $YCuO_x$ has a dramatic effect on the electrical properties. A clear transition to the superconducting state has been found at the critical temperature (T_C) of 75 K for the optimum number of pulses.

[IX] Since only 20 pulses are needed for completion of two $BaCuO_x$ unit cell layers, the accuracy of the amount of deposited material is limited to ~10% for one unit cell layer. Other deposition parameters, like pressure and energy density on the target, can be varied to adjust the amount. However, only small variations of the parameters are allowed to ensure stoichiometric deposition. Variation of the spot size and shape is a better way to adjust the amount of material deposited in one pulse and has, therefore, been applied to optimize PLiD of the sub-unit cell layers.

[X] The used excimer laser has a pulse-to-pulse stability of ~5%. If the number of pulses for one unit cell layer is sufficiently high, the fluctuation will be averaged.

[XI] Four-probe resistance-versus-temperature measurements were performed in a He cryostat. A distance between the voltage contacts (bond pads of 25 μm Al wire) of ~2 mm was used.

Table 6.1: Overview of deposition conditions and four-probe resistance at 300 K. Deposition: T =600 °C, P_{O_2} =14 Pa, Post-anneal: T =800 °C at P_{O_2} =0.5 atm, layer thickness 40 Y123 unit cell layers.

#BaCuO/#YCuO	Energy in spot [mJ]	R300 [Ω]
20/54	26	134
20/56	26	45
20/58	26	285
20/61	26	327
20/56	24	72
20/56	28	21

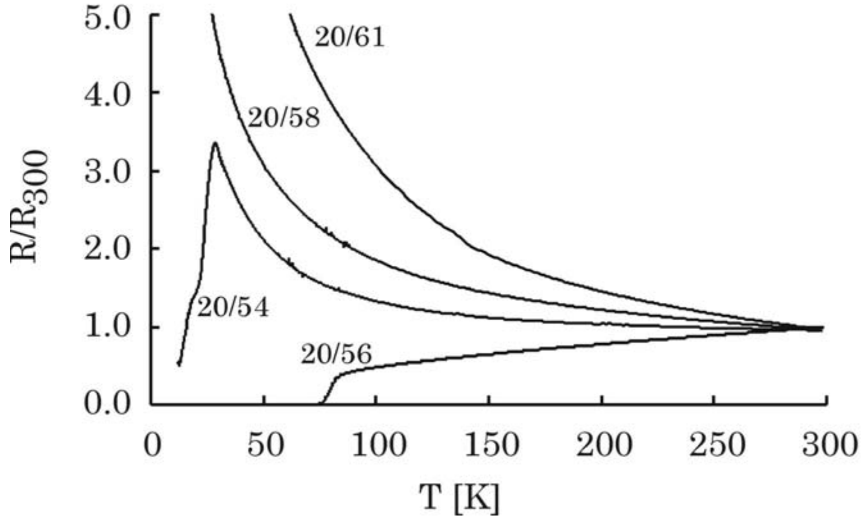

Figure 6.4: Normalized four-probe resistance of Y123 versus temperature for different ratios $BaCuO_x/YCuO_x$, given in number of pulses applied for 2 and 1 unit cell layer, respectively. The resistance values at 300 K are given in table 6.1.

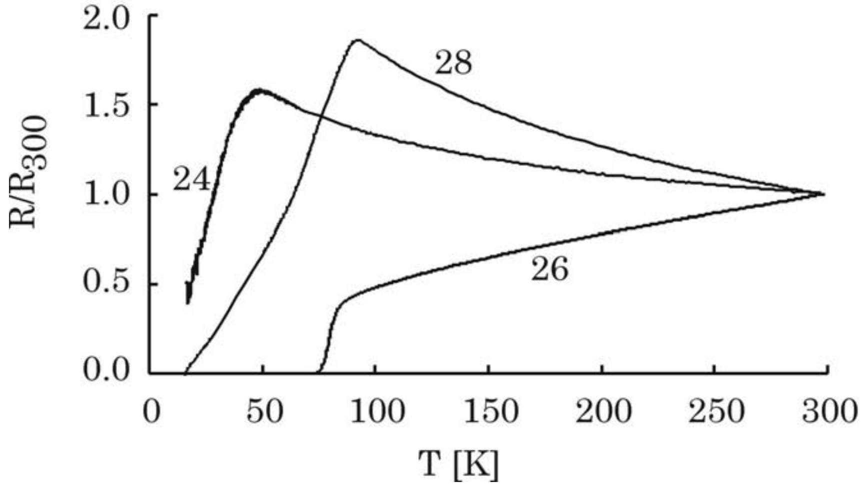

Figure 6.5: Normalized four-probe resistance of Y123 versus temperature for different energies in the spot at the target. The resistance values at 300 K are given in table 6.1.

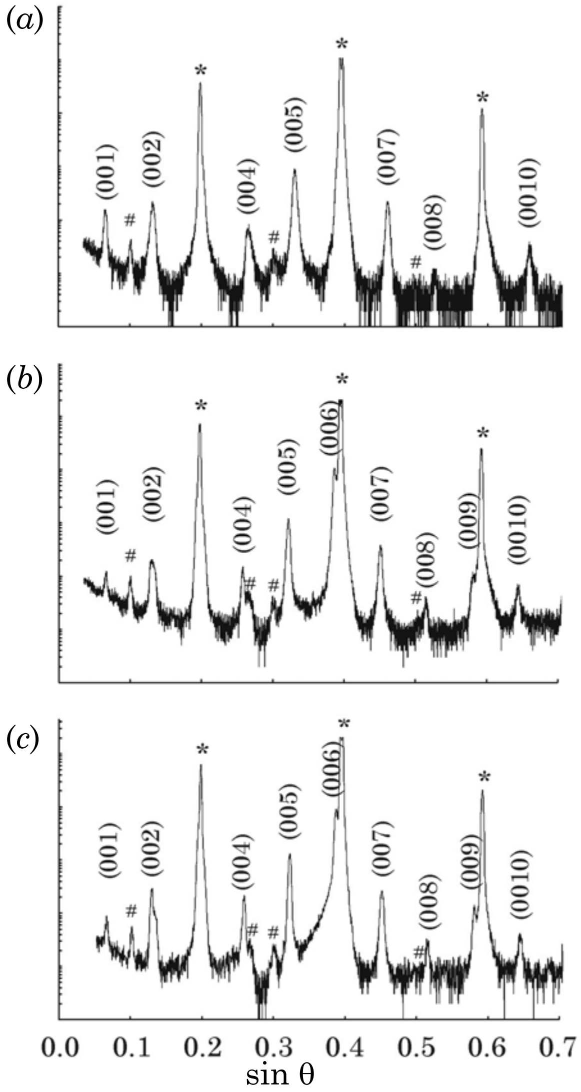

Figure 6.6: XRD θ-2θ scans of 40 Y123 unit cell layers on $SrTiO_3$; optimized deposition conditions, $BaCuO_x/YCuO_x = 20/56$ and laser energy density = 1.3 J/cm^2 (a); 20/58 and 1.3 J/cm^2 (b), 20/56 and 1.25 J/cm^2 (c). The $SrTiO_3$ substrate reflections are indicated with an asterisk and spectral contributions ($\lambda/2$ and $\lambda/3$) with a cross.

Not only the ratio, but also the amount of material applied for deposition of the sub-unit cell layers affects the electrical properties, as shown in figure 6.5. Here the optimum ratio in the number of pulses of 20/56 ($BaCuO_x/YCuO_x$) is kept constant. The amount of deposited material is changed by small adjustment of the laser energy density[XII] in the spot at the target.

[XII] The optimum ratio was determined at the energy density of 1.3 J/cm^2 (energy 26 mJ, spot area 2 mm^2). A difference of ~4 % of the deposition rate per pulse is estimated for a change in the spot energy from 26 to 28 mJ.

6.3.2.3 Structural properties

Figure 6.6 shows typical XRD θ-2θ scans of 40 Y123 unit cell layers on $SrTiO_3$. From figure 6.6 (a), i.e., at optimum growth conditions, a c-lattice parameter of 11.71 Å is derived, close to the expected value of 11.68 Å for fully oxidized Y123. In figure 6.6 (b) the number of pulses for one $YCuO_x$ unit cell layer was changed from 56 to 58, leading to a c-lattice parameter of 11.96 Å. Changing the amount for both $BaCuO_x$ and $YCuO_x$ unit cell layers by decreasing the energy density on the targets from 1.3 to 1.25 J/cm^2 results in a c-lattice parameter of 11.94 Å, derived from figure 6.6 (c).

The enlarged c-lattice parameter is probably caused by disordering of Y and Ba atoms or lattice defects introduced during growth[20,21]. The latter could be confirmed by HREM, see transmission micrograph in figure 6.7 (a). A selective area electron diffraction pattern of an Y123 film consisting of lattice defects, indicating the enlarged c-lattice parameter, is given in figure 6.7 (b) and (c). Besides lattice defects, occasionally formation of $YBa_2Cu_4O_8$ (Y124)[22] is observed, as shown in the transmission micrograph depicted in figure 6.7 (d).

6.3.3 Discussion

The main results of the previous section are summarized as follows.

(1) Two unit cell thick $BaCuO_x$ layers are sufficiently stabilized by the $SrTiO_3$ substrate, whereas $YCuO_x$ is only stabilized in the Y123 structure.
(2) Using the PLiD method, the necessary layer-by-layer growth for sub-unit cell epitaxy is achieved, indicated by RHEED and AFM.
(3) Superconducting Y123 films are obtained after *in situ* annealing.
(4) The morphology of the as deposited Y123 films shows a smooth surface with maximum step heights of 4 Å, which increased during the anneal procedure to maximum step heights comparable to the c-lattice parameter of Y123.
(5) Non-optimized growth conditions lead to lattice defects in the Y123 films resulting in an elongated c-lattice parameter and suppressed T_C[23].

The surface morphology of the as-deposited films clearly changes during the *in situ* anneal step due to recrystallization, indicating that inter-diffusion and reaction at the surface do occur at the anneal conditions. This is supported by the fact that only superconducting films are obtained after the anneal step. The inter-diffusion is limited and cannot be compared to the intermixing observed in solid phase epitaxy. Structural defects, introduced during growth, are frozen in the film and are not healed by the anneal procedure, as clearly shown by HREM. The success of the proposed method is, therefore, strongly dependent on the exact growth control of the individual constituents.

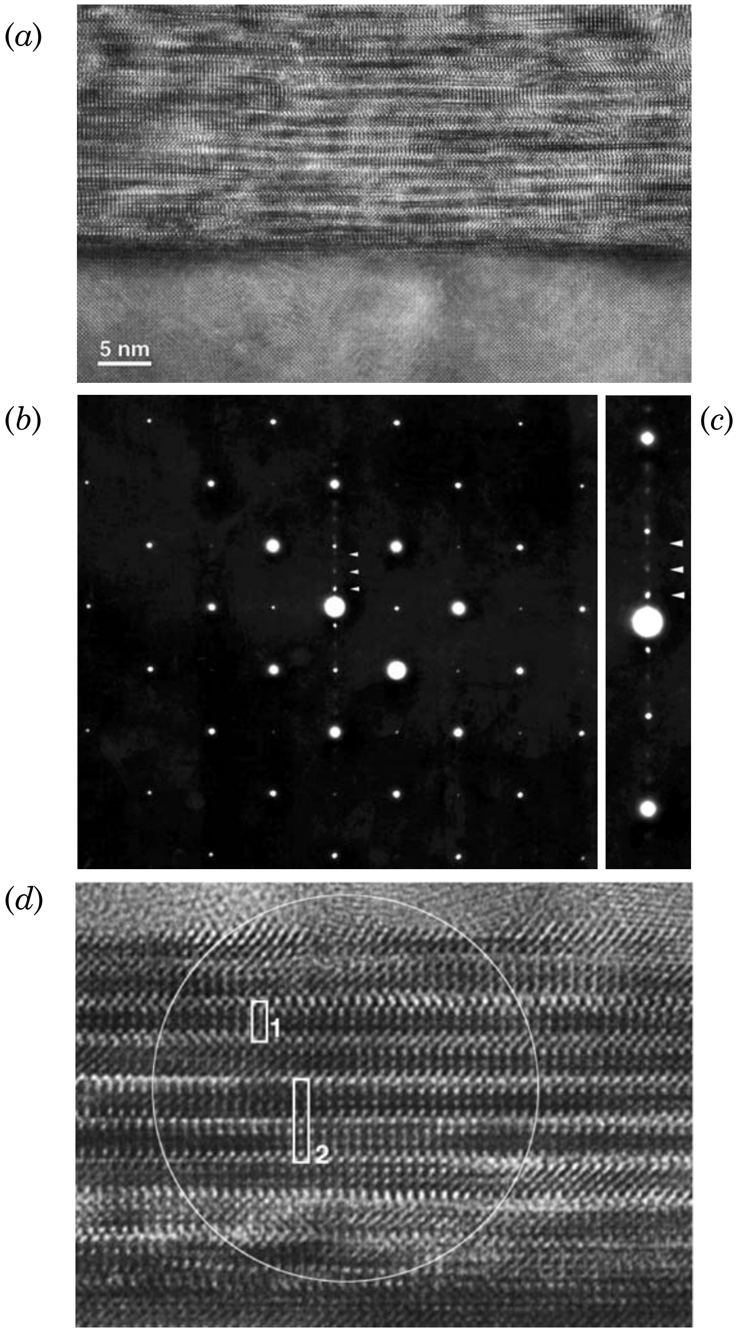

Figure 6.7: Cross-section transmission image of a highly defective Y123 film, deposited using the wrong number of pulses for $YCuO_x$ layer (a). Selected area electron diffraction (SAED) pattern (b) and close-up near the (00l) reflections (c) of an Y123 film as in figure 6.6 (b) indicating the enlarged c-lattice parameter; the (003) reflection, indicated by the topmost arrowhead, does not coincide with the (001) reflection of $SrTiO_3$, as would be in the case of a correct c-lattice parameter. Cross-section transmission image showing $YBa_2Cu_4O_8$ (Y124) phase (d). The Y124 unit cell is indicated by the rectangle with index 2, showing the ½a shift between the adjacent CuO planes in the Y124.

Small variations have a dramatic effect on the structural and electrical properties. Most of the deposition parameters can be adjusted with high accuracy, like growth temperature and deposition pressure as well as the laser spot size. The laser pulse energy and, consequently, the energy density on the target are, however, not well defined. Due to the aging[XIII] of the excimer laser gasses, higher voltages have to be applied to the laser to obtain the required pulse energy, resulting in a change of the laser pulse shape. The energy density distribution in the laser beam as well as the time dependent power output in the laser pulse will change. The latter is of special importance, since it affects the ablation of the target and, therefore, the pulse deposition rate.

6.4 Conclusions

The proposed sub-unit cell layer epitaxy, employing PLiD from separate $BaCuO_x$ and $YCuO_x$ targets, has been successfully applied for the fabrication of Y123 thin films. At the deposition conditions of 600 °C and 14 Pa oxygen pressure, tetragonal $BaCuO_x$ is stabilized by the $SrTiO_3$, whereas $YCuO_x$ could only be stabilized in the Y123 structure. The necessary layer-by-layer growth was imposed by the interval deposition. Accurate control of the pulse deposition rate is found to be essential and make demands on the laser specifications, especially the pulse energy stability at high repetition rate.

The highest T_C value obtained using the proposed deposition method is 85 K[XIV]. The surface morphology of the *in situ* annealed films resulted from surface recrystallization. At optimum conditions, a maximum step height of 12 Å, comparable to the c-lattice parameter of Y123 was found. This recrystallization indicated that reaction and inter-diffusion between the deposited oxides occur. The surface morphology differs from Y123 films using standard PLD, since no island growth has been observed. The new approach opens possibilities for the use of Y123 films in all-oxide heterostructures, necessary for fabrication of superconducting devices and electronics using planar technology.

[XIII] The aging depends on the usage of the laser. In our case aging takes place in approximately two weeks, after which the laser has to be refilled.

[XIV] This value was obtained by lowering the oxygen deposition pressure from 14 to 12 Pa, leading to a small increase of the deposition rate.

References

1 S. Bals, G. Rijnders, D.H.A. Blank and G. Van Tendeloo, *Physica C* **355**, 225 (2001)

2 G. Koster, G. J. H. M. Rijnders, D. H. A. Blank, and H. Rogalla, *Appl. Phys. Lett.* **74**, 3729 (1999)

3 R. Gross, J. Klein, B. Wiedenhorst, C. Höfener, U. Schoop, J.B. Philipp, M. Schonecke, F. Herbstritt, L. Alff, Y. Lu, A. Marx, S. Schymon, S. Thienhaus and W. Mader in *Superconducting and Related Oxides: Physics and Nanoengeneering IV*, D. Pavuna and I. Bozovic Eds. (Proceedings of SPIE) **4058** (2000)

4 K.G. Frase, E.G. Liniger and D.R. Clarke, *J. Am. Ceram. Soc.* **70**, C-204 (1987)

5 I. Bozovic and J.N. Eckstein, *Appl. Surf. Sci.* **113/114**, 189 (1997)

6 J.-P. Locquet and E. Mächler, *Mater. Res. Bull.* **9**, 39 (1994)

7 J.-P. Locquet, A. Catana, E. Mächler, C. Gerber and J. G. Bednorz, *Appl. Phys. Lett.* **64**, 372 (1994)

8 B.W. Hussey, A. Gupta and E. Olsson, *J. Appl. Phys.* **76**, 2807 (1994)

9 B.W. Hussey and A. Gupta, *J. Appl. Phys.* **72**, 287 (1992)

10 A. Abert, J.P. Contour, A. Défossez, D. Ravelosona, W. Schwegle and P. Ziemann, *Appl. Surf. Sc.* **96-98**, 703 (1996)

11 H.Y. Zhai and W.K. Chu, *Appl. Phys. Lett.* **76,** 3469 (2000)

12 D. Hüttner, O. Meyer, J. Reiner and G. Linker, *Appl. Phys. Lett.* **66**, 1273, (1995)

13 T.-S Gau, S.-L Chang, H.-H. Hung, C.-H. Lee, T.-W. Huang, H.-B. Lu, S.-J. Yang and S.-E Hsu, *Appl. Phys. Lett.* **65**, 1720 (1994)

14 L.X. Cao, J. Zegenhagen, E. Sozontov and M. Cardona, *Physica C* **337**, 24 (2000)

15 D.H. Lowndes, X.-Y Zheng, S. Zhu, J.D. Budai and R.J. Warmack, *Appl.Phys. Lett.* **61**, 852 (1992)

16 D.P. Norton, D.H. Lowndes, X.-Y. Zheng, S. Zhu and R.J. Warmack, *Phys. Rev. B* **44**, 9760 (1991)

17 G. Koster, K. Verbist, G. Rijnders, H. Rogalla, G van Tendeloo and D.H.A. Blank, *Physica C* **353**, 167 (2001)

18 N. Ilynych, S. Zaitzeva, G. Moiseev, J. Šesták and N. Vatolin, *Thermochimica Acta* **266**, 285 (1995)

19 G. Koster, *Artificially layered oxides by pulsed laser deposition*, PhD Thesis ISBN 9036513367, University of Twente, 1999

20 J. Ye and K. Nakumura, Phys. Rev. B **48**, 7554 (1993)

21 J.L. MacManus-Driscoll, J.A. Alonso, P.C. Wang, T.H. Geballe and J.C. Bravman, *Physica C* **232**, 288 (1994)

22 Y. Xin, W. Zhou and C.J. Humphreys, *Physica C* **249**, 319 (1995)

23 G. Gibson, L.F. Cohen, R.G. Humphreys and J.L. MacManus-Driscoll, *Physica C* **333**, 139 (2000)

Summary

In this thesis, the initial growth stage, i.e., nucleation and growth of the first few unit cell layers, of complex oxides was studied in *real time* during pulsed laser deposition (PLD). These studies were performed at their optimal epitaxial growth conditions, i.e., high temperature and high oxygen pressure, and revealed the kinetics in the homoepitaxial growth of $SrTiO_3$ as well as the unexpected growth mechanisms in the heteroepitaxial growth of $SrRuO_3$ and $REBa_2Cu_3O_{7-\delta}$ (RE123, RE is Y or rare earth element) on $SrTiO_3$. The outcome of these studies was utilized in growth manipulation by means of modified deposition schemes, i.e., pulsed laser *interval* deposition and sub-unit cell epitaxy.

Two developments were crucial for the growth study as well as manipulation: perfect crystalline, *single* TiO_2 terminated $SrTiO_3$ substrates and *high-pressure* reflection high-energy electron diffraction (RHEED).

The first was obtained by a two-step chemical treatment, consisting of a soak in water followed by a short dip in buffered HF solution (BHF). Due to the enhanced etch selectivity of SrO, by formation of the Sr-hydoxide complex, with respect to TiO_2 the etching time could be reduced and, furthermore, the pH value of the BHF solution increased. Both were essential to prevent damage to the substrate surface and avoid etch-pits. Proper subsequent heat treatment resulted in perfect crystalline single terminated $SrTiO_3$ surfaces.

The second development enabled *in situ* real time growth monitoring with RHEED at the relatively high oxygen pressures used during PLD of oxides. Electron beam intensity losses due to scattering in high-pressure background gasses are minimized by reducing the travel length of the electrons in the high-

pressure region. As a result, growth control and growth manipulation on an atomic level became feasible at optimal epitaxial growth conditions of the complex oxides.

Homoepitaxial growth studies of $SrTiO_3$ with this monitoring system showed, besides the growth mode during deposition, unique features of PLD, i.e., pulsed deposition and the high deposition rate in the pulse. The latter is exploited in growth kinetics experiments as well as growth manipulation. After every deposition pulse, relaxation and recovery of the RHEED intensity is observed during two-dimensional (2D) growth and step flow growth, respectively. Both are related to the diffusion of the deposit and have been used to extract the energy barriers for diffusion during homoepitaxial growth of $SrTiO_3$ and heteroepitaxial growth of $SrRuO_3$ on $SrTiO_3$. The pulsed, high deposition rate, leading to a high supersaturation, is utilized in a new deposition approach, pulsed laser *interval* deposition (PLiD). By depositing the number of pulses needed for completion of one unit cell layer in a short time interval, the supersaturation is maintained until the complete unit cell layer is deposited. After the deposition, the film can rearrange. Using this approach, layer-by-layer growth could be imposed in a growth regime where otherwise island growth takes place.

The ferromagnetic $SrRuO_3$ is structurally similar to $SrTiO_3$ and is used in this thesis as a model system for studying heteroepitaxial growth. The observed growth mode was dependent on the average terrace width of the $SrTiO_3$ substrate. If the average terrace width of the vicinal substrate is comparable to the migration length of the deposit, step flow growth is observed, whereas increasing the terrace width results in a mixture of step flow and 2D growth. After a few unit cells, a steady state surface step density is obtained where advancing steps engulf the growing 2D islands. As a result a steady RHEED intensity is observed.

The oxidation power of molecular oxygen at the high pressures used in PLD during growth of perovskite oxides is sufficiently high to form a stable, epitaxial thin film structure of $SrRuO_3$ as well as RE123. The terminating atomic layer, however, of both oxides is affected by the oxidation power. Starting with TiO_2 terminated $SrTiO_3$, i.e., B-site termination, stoichiometric deposition and a perovskite stacking sequence should lead to B-site termination. However, RHEED experiments indicated that the expected RuO_2 and CuO_x termination for $SrRuO_3$ and Y123, respectively, did not occur. The oxidation power at the deposition conditions was insufficient to stabilize the B-site termination. This resulted in evaporation of the volatile RuO_x during the initial growth, i.e., the first unit cell layer, of $SrRuO_3$, and, consequently, to a termination conversion from RuO_2 (B-site) to SrO (A-site). In the case of Y123, the non-stabilized CuO_x layer leads to Cu_2O precipitates. Therefore, SrO terminated $SrTiO_3$ is used to avoid the precipitation during the initial growth of Y123. In this case, A-site termination is preserved and all the deposited material is incorporated in the epitaxial film. Even a better way to avoid Cu_2O precipitation is the control of the cation ratio during deposition of the first unit cell layer. Since the terminating CuO_x layer is not incorporated in the first unit cell layer, the cation ratio for RE:Ba:Cu should be 1:2:2 rather than 1:2:3 and the stoichiometry of the deposited material is, therefore, adjusted to the stoichiometry of the actual growing unit cell layer.

The initial growth of Dy123 on single TiO_2 terminated $SrTiO_3$ is extensively studied and high-resolution electron microscopy (HREM) revealed the existence of two possible stacking sequences in the first unit cell layer. The single termination and the perfect crystalline surface of the substrate were essential for the determination of the stacking sequence at the substrate-film interface. The two stacking sequences resulted in a high density of anti-phase boundaries (APB's) as well as initial surface roughness of the Dy123 on the atomically flat substrate terraces. The dramatic decrease of the RHEED intensity after deposition of one unit cell layer is also an indication for this increased roughness. Stoichiometry control by deposition with 1:2:2 cation ratio not only prevented Cu_2O precipitation but also influenced the stacking sequence. No APB's were observed in HREM, indicating the existence of one stacking sequence. Unit cell layer-by-layer growth is observed during subsequent deposition with 1:2:3 cation ratio. Island growth due to stress relaxation mechanisms in the heteroepitaxial of Dy123 growth, however, could not be avoided by adjustment of the PLD conditions.

A different deposition approach, the sub-unit cell epitaxy, is proposed to control the growth of RE123. Sub-unit cell layers of $YCuO_x$ and $BaCuO_x$ are sequentially deposited at significantly lower temperature compared to standard PLD conditions. To impose layer-by-layer growth at these conditions, interval deposition was applied. Using this approach, the Cu_2O precipitation is prevented and the stacking sequence controlled. Films with peak-to-peak roughness comparable to the c-lattice parameter of RE123, i.e., 12 Å, and maximum superconducting transition temperatures of 85 K were obtained. The absence of island growth, observed in films deposited using standard PLD, indicates a different stress relaxation mechanism. The growth is controlled on an atomic level and requires accurate adjustment of the deposition parameters. Small variations cause differences in the pulse deposition rate and have to be avoided. The laser pulse energy distribution is found to be crucial, since it could not be adjusted reproducibly on the required level.

The achieved results mentioned above, i.e., the ability to control growth on an atomic level at the most favorable PLD conditions, can be applied in the fabrication of complex epitaxial multi-layered structures. As an example, $SrRuO_3$-$SrTiO_3$-$SrRuO_3$ epitaxial heterostructures have been constructed. These structures are model systems to study the spin-dependent electrical transport properties, provided that the crystalline $SrRuO_3$ films are single domain and the interfaces

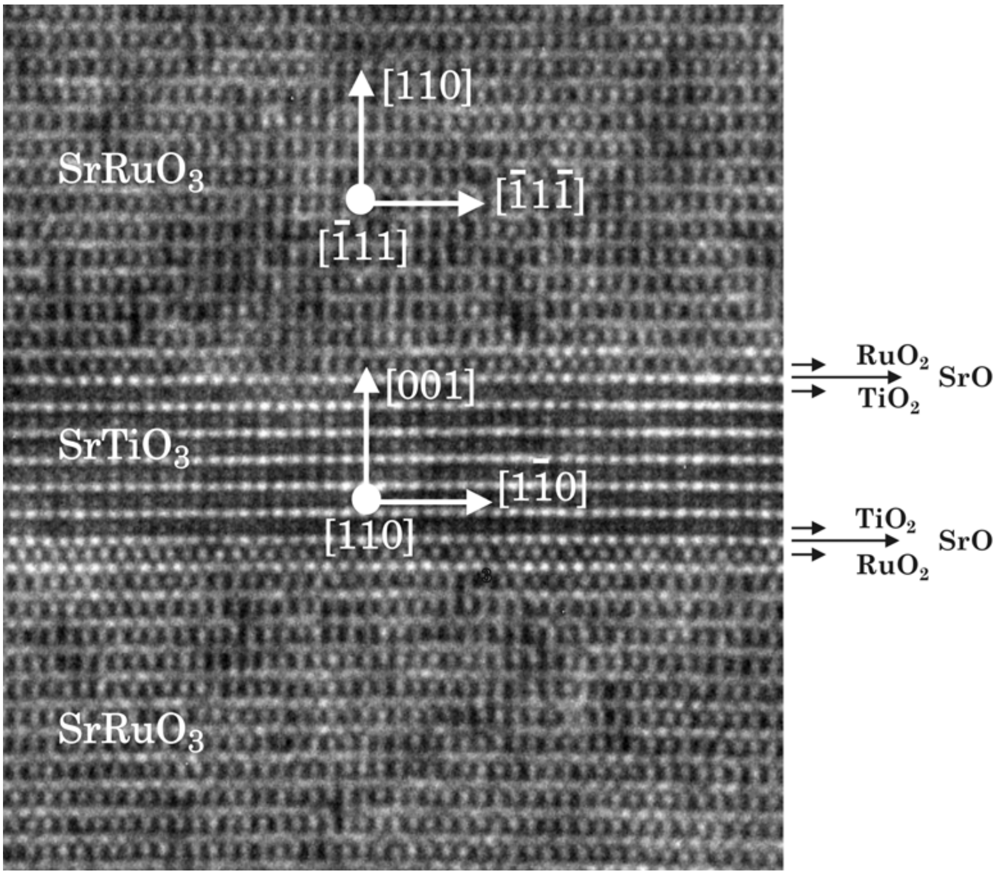

Figure 1: Cross-section HREM of an all-oxide epitaxial heterostructure; $SrRuO_3$-$SrTiO_3$-$SrRuO_3$, indicating the atomically smooth interfaces. The bottom and top $SrRuO_3$ electrodes have a single domain structure with film thickness of 50 and 35 nm, respectively. The $SrTiO_3$ barrier layer is 2.4 nm, i.e., 6 unit cell layers.
(HREM image: X. Q. Pan, University of Michigan, Ann Harbor)

atomically smooth. These requirements could be fulfilled by the controlled growth at optimal deposition conditions by high-pressure RHEED on the perfect crystalline and single TiO_2 terminated $SrTiO_3$ substrates. A cross-section HREM of such a heterostructure is depicted in figure 1 indicating the perfect epitaxy throughout the structure. The requirements reflect almost all the studied subjects in this thesis: epitaxially layered growth on atomically smooth, prefect crystalline substrates as well as control of the (interface) termination layer, the growth mode and growth rate by high-pressure RHEED in pulsed laser (*interval*) deposition of (sub) unit cell layers.

Samenvatting

Oxidische materialen vertonen naast optische, dielektrische en magnetische eigenschappen een rijk spectrum aan elektrische transporteigenschappen. Oxides kunnen zowel isolerend, halfgeleidend, normaalgeleidend als supergeleidend zijn. Gebruik makend van de grote verscheidenheid aan materiaaleigenschappen is een nieuw onderzoeksgebied ontstaan, "*oxide-electronics*" genaamd. Nieuwe elektronische schakelingen, gebaseerd op epitaxiale heterostructuren van oxidische materialen zoals de magnetische tunneljuncties, supergeleidende elektronische schakelingen en piezo-elektrische schakelingen, hebben een groot potentieel in toekomstige elektronische toepassingen en zijn daarom onderwerp van onderzoek in veel researchgroepen.

De oxiden die in dit proefschrift behandeld worden behoren tot de perovskieten met de algemene structuurformule ABO_3 (zie figuur 2.10). Deze structuur kan worden beschouwd als een kubisch kristalrooster met B-atomen op de hoekposities en zuurstof atomen in het midden van elke ribbe. De A-atomen zijn gesitueerd in het centrum van het rooster. Vele vervormingen van de ideale kubische structuur, zoals kanteling van de octaëders[I] en verplaatsing van de kationen, zijn mogelijk en beïnvloeden de fysische eigenschappen van de perovskieten.

Deze eigenschappen worden bepaald door zeer kleine karakteristieke lengteschalen. Bijvoorbeeld de coherentielengte in hoge-temperatuur supergeleiders, zoals $REBa_2Cu_3O_{7-\delta}$ (RE123, RE is Y of een zeldzame aarde element), is ~10 tot 20 Å; vergelijkbaar met de eenheidscelparameters. Deze kleine karakteristieke afstanden hebben een grote invloed op de toepasbaarheid van

---

[I] De zuurstof atomen rondom elk B-atoom vormen een octaëder.

perovskieten in heterostructuren. Het grensvlak, de interface, tussen twee verschillende oxiden bepaalt in belangrijke mate de fysische eigenschappen van de heterostructuren. Controle en engineering van de interface op eenheidscel, of zelfs atomair, niveau zijn daarom noodzakelijk. Dit stelt hoge eisen aan de fabricage van heterostructuren. Niet alleen depositietechnieken moeten adequaat zijn maar ook de filmgroei moet op atomair niveau worden gecontroleerd en zonodig gemanipuleerd.

Dit proefschrift beschrijft zowel de studie als de manipulatie van de initiële groei van perovskiet-oxiden tijdens gepulste laser depositie (PLD). Nucleatie en groei van de eerste eenheidscellagen zijn *real time* bestudeerd m.b.v. reflectie hoge-energie elektron diffractie (RHEED) onder optimale groeiomstandigheden. Vooral de groeitemperatuur en de zuurstofdruk zijn belangrijke parameters tijdens de groei van deze complexe oxiden. Epitaxiale groei van een stabiele structuur vereist zowel hoge temperaturen (typisch 500-900 °C) als relatief hoge zuurstofdrukken (typisch 1-100 Pa).

Twee onwikkelingen zijn zeer belangrijk gebleken voor de groeistudie en -manipulatie en worden in dit proefschrift behandeld: perfect kristallijne $SrTiO_3$ substraten met een *enkelvoudig* TiO_2 eindvlak en *hoge-druk* RHEED.

Groeistudie en -manipulatie op een atomair niveau vereisen substraten met een zeer goed gedefinieerd oppervlak. De morfologie, microstructuur en eindvlak van het oppervlak beïnvloeden de epitaxiale groei en controle van deze parameters is derhalve essentieel. Het eindvlak van een $SrTiO_3$ substraat kan zowel uit SrO, TiO_2 of een mengsel van beide bestaan. Een combinatie van een chemische en thermische behandeling is succesvol toegepast om een $SrTiO_3$ substraatoppervlak met de gewenste eigenschappen te verkrijgen. Door gebruik te maken van het verschil in oplosbaarheid van de twee mogelijke oxiden in een gebufferde waterstoffluoride-oplossing is een enkelvoudig TiO_2 eindvlak verkregen. Tijdens de thermische behandeling wordt een perfect kristallijn oppervlak gevormd, zie figuur 2.11.

RHEED is een veelgebruikte techniek om filmgroei te monitoren. T.g.v. de verstrooiing van elektronen werd RHEED alleen toegepast onder (ultra) hoog-vacuum omstandigheden. Het gebruik van RHEED tijdens PLD van oxiden bij hoge zuurstofdruk werd dus niet mogelijk geacht. Het ontwikkelde hoge-druk RHEED systeem minimaliseert de verstrooiingsverliezen van elektronen en maakt *real time* studie van filmgroei bij relatief hoge depositiedrukken mogelijk. Dit betekent dat de groei van oxiden tijdens PLD onder optimale groeicondities kan worden bestudeerd.

Homoepitaxiale groeistudies van $SrTiO_3$ laten een invloed van de gepulste depositie zien. Na elke depositiepuls is een grote afname in de RHEED-intensiteit waargenomen gevolgd door relaxatie en herstel van de intensiteit. Dit is het gevolg van de mobiliteit van het gedeponeerde materiaal aan het oppervlak van de film. Het relaxatiegedrag van de intensiteit kan daarom worden gebruikt om energiebarrières voor diffusie te bepalen. De hoge depositiesnelheid tijdens de depositiepuls leidt tot een zeer hoge oververzadiging aan het oppervlak van de film en is toegepast in een nieuw depositieschema: gepulste laser *interval* depositie. Precies het benodigde materiaal voor één eenheidscellaag wordt in een korte interval[II] gedeponeerd. Na depositie kan het materiaal zich reorganiseren en een gesloten eenheidscellaag vormen. Met deze depositiemethode kan 2-dimensionale groei worden verkregen onder omstandigheden waar normaliter 3-dimensionale groei optreedt.

Ferromagnetisch $SrRuO_3$ is gedeponeerd op $SrTiO_3$ substraten met TiO_2 als eindvlak. De initiële groei van $SrRuO_3$ kan worden gezien als een modelsysteem voor het bestuderen van heteroepitaxiale groei. $SrRuO_3$ heeft unieke structurele, magnetische en elektronische eigenschappen en is bovendien chemisch zeer stabiel. Het is een van de best geleidende oxiden en daarom een belangrijke kandidaat als elektrodemateriaal in oxidische componenten. Epitaxiale groei van stabiel $SrRuO_3$ vereist specifieke groeiomstandigheden tijdens PLD, zoals een temperatuur van ~600 °C en zuurstofdruk tussen 10 en 20 Pa. Het hoge-druk RHEED systeem is uitermate geschikt gebleken om de initiële groei te bestuderen tijdens deze groeiomstandigheden. De geobserveerde groeimode hangt sterk af van de gemiddelde terraslengte van de substraten. Een combinatie van *step flow* en 2-dimensionale groei leidt tot een opmerkelijke groeimode; 2-dimensionale eilanden op de terrassen worden “opgeslokt” door de aangroeiende stapranden. Na depositie van enkele eenheidscellagen wordt een evenwicht in de dichtheid van stapranden bereikt, resulterend in een constante RHEED-intensiteit.

Het oxiderend vermogen van moleculair zuurstof is voldoende groot voor de vorming van een stabiele fase van zowel $SrRuO_3$ als RE123 tijdens PLD. Het atomaire eindvlak van beide oxiden is echter sterk afhankelijk van het oxiderend vermogen. Stoichiometrische depositie op een $SrTiO_3$ substraat met TiO_2 als eindvlak en een perovskiet stapelingsvolgorde zou moeten leiden tot een BO_2 eindvlak van de ABO_3 film. RHEED experimenten tijdens de initiële groei van $SrRuO_3$ en RE123 tonen echter aan dat niet de verwachte RuO_2 en CuO_x het eindvlak vormen. Het oxiderend vermogen van moleculair zuurstof is ogenschijnlijk niet voldoende om een BO_2 eindvlak in beide oxiden te stabiliseren. In het geval van $SrRuO_3$ leidt dit tot sublimatie van vluchtige RuO_x componenten tijdens de initiële groei. Als gevolg treedt een conversie in de compositie van eindvlak op; van BO_2 (RuO_2) naar AO (SrO). In het geval van RE123 leidt het onstabiele CuO_x eindvlak tot de vorming van Cu_2O precipitaten. Vorming van deze

---

[II] De tijdsduur wordt bepaald door het totaal aantal pulsen dat nodig is voor de vorming van een eenheidscellaag en de maximaal haalbare pulsfrequentie.

ongewenste precipitaten kan worden voorkomen door een $SrTiO_3$ substraat te gebruiken met SrO als eindvlak. Een andere methode is de verhouding tussen de kationen tijdens de depositie van de eerste eenheidscellaag te controleren. Doordat het CuO_x eindvlak niet wordt geïntegreerd, is de RE:Ba:Cu verhouding in de eerste eenheidscellaag gelijk aan 1:2:2 en niet 1:2:3. Depositie met een 1:2:2 verhouding voorkomt daarom de vorming van Cu_2O precipitaten.

$SrTiO_3$ substraten met een enkelvoudig eindvlak zijn essentieel voor de juiste bepaling van de stapelingsvolgorde van de film m.b.v. hoge-resolutie elektronen microscopie (HREM). De initiële groei van RE123 op $SrTiO_3$ substraten met TiO_2 eindvlak wordt gedomineerd door verschillende stapelingsmogelijkheden van de verschillende atomaire vlakken in de eerste RE123 eenheidscellaag. Dit leidt tot een verruwing van het oppervlak tijdens de initiële groei en tot de vorming van anti-fase grensvlakken. Beide kunnen worden voorkomen door de depositie van de 1:2:2 eenheidscellaag.

Een nieuwe depositieschema, sub-eenheidscellaag epitaxy genaamd, is gebruikt om de groei van RE123 te controleren. Sub-eenheidscellagen van $BaCuO_x$ en $YCuO_x$ zijn afwisselend gedeponeerd. De interval depositiemethode is toegepast om een laag-bij-laag groeimode te verkrijgen. Deze groeimode bleek mogelijk bij een depositietemperatuur die beduidend lager is dan bij stoichiometrische depositie. M.b.v. het nieuwe depositieschema wordt de stapelingsvolgorde gecontroleerd en de vorming van Cu_2O precipitaten voorkomen. Na thermische behandeling in zuurstof vertonen de RE123 films een piek-tot-piek ruwheid vergelijkbaar met de c-as eenheidscelparameter (12 Å) en een maximale supergeleidende transitietemperatuur van 85 K. De groei wordt gecontroleerd op atomair niveau en vereist een nauwkeurige instelling van de depositieparameters. Kleine afwijkingen leiden tot variaties van de depositiesnelheid en moeten worden voorkomen. Kritisch hierbij is de pulsenergie van de laser omdat deze niet voldoende nauwkeurig reproduceerbaar kan worden ingesteld[III].

De mogelijkheid om groei te controleren op een atomair niveau onder optimale groeiomstandigheden kan worden toegepast in de fabricage van complexe oxidische epitaxiale meerlagenstructuren, zoals bijvoorbeeld de epitaxiale $SrRuO_3$-$SrTiO_3$-$SrRuO_3$ heterostructuren. Deze structuren dienen als modelsysteem voor de studie van spin-afhankelijke elektrische transporteigenschappen. De $SrRuO_3$ films moeten éénkristallijn zijn en de grensvlakken tussen $SrRuO_3$ en $SrTiO_3$ atomair vlak. Aan deze voorwaarden zijn voldaan door de groei op $SrTiO_3$ substraten met een enkelvoudig eindvlak te controleren met hoge-druk RHEED onder optimale groeiomstandigheden. Figuur 1 toont een HREM opname van een $SrRuO_3$-$SrTiO_3$-$SrRuO_3$ heterostructuur. Het laat een perfecte epitaxy door de gehele structuur zien en weerspiegelt bijna alle onderwerpen in dit proefschrift: epitaxiale gelaagde

---

[III] De gebruikte laser is een KrF excimeerlaser met een puls-tot-puls energiestabiliteit van ~5%.

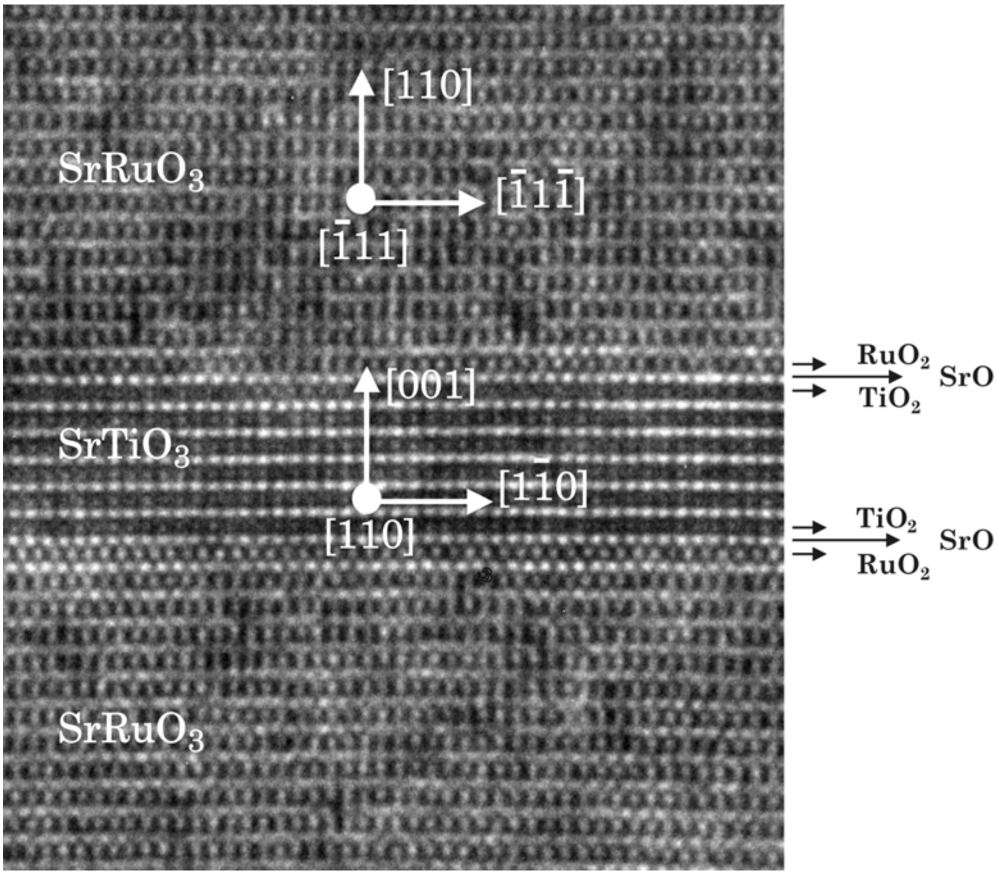

Figuur 1: HREM opname van een oxidische epitaxiale heterostructuur; $SrRuO_3$*-*$SrTiO_3$*-*$SrRuO_3$*. De grensvlakken zijn atomair glad. De onderste en bovenste* $SrRuO_3$ *elektroden hebben een enkelvoudige domeinstructuur met een filmdikte van respectievelijk 50 and 35 nm. De* $SrTiO_3$ *barrièrelaag is 2.4 nm, d.w.z 6 eenheidscellagen. (HREM opname: X. Q. Pan, University of Michigan, Ann Harbor)*

groei op atomair-vlakke perfect-kristallijne substraten, de controle van de (interface) eindvlakken, de controle van zowel de groeimode als de groeisnelheid m.b.v hoge-druk RHEED tijdens gepulste laser (interval) depositie van (sub) eenheidscellagen.

Dankwoord

Nu het proefschrift voltooid is, wordt het tijd om al diegenen te bedanken die hebben bijgedragen aan de totstandkoming van dit proefschrift. Ik realiseer me echter dat het niet mogelijk is een dankwoord te schrijven dat recht doet aan alle steun en stimulans die ik heb gekregen van een groot aantal personen. In de 12 jaar dat ik werkzaam ben in de leerstoel Lage Temperaturen zijn veel medewerkers, promovendi en studenten de revue gepasseerd. Eenieder heeft wel bijgedragen aan de goede werksfeer en/of het proefschrift. Onmogelijk kan ik allen persoonlijk bedanken. Ik hoop dat dit proefschrift voldoende bewijs is van jullie steun.

Allereerst wil ik Horst bedanken voor het vertrouwen dat hij mij gegeven heeft voor en tijdens de promotietijd. Zijn vertrouwen leek bijna groter dan de mijne. Ondanks zijn veel te drukke agenda was er gelukkig tijd om het een en ander te bespreken.

Heel veel dank ben ik verschuldigd aan Dave. Niet alleen heeft hij een grote rol gespeeld in de aanloopfase van de promotie, hij is de spil van het materiaalkundig onderzoek binnen de leerstoel. Zijn enthousiasme voor het onderzoek is een stimulans voor elke onderzoeker. Zijn manier van onderzoek initiëren en begeleiden is uniek en een voorbeeld voor velen. Juist daardoor geniet het onderzoek een wereldwijde erkenning. Dave, bedankt voor je vriendschap, je niet aflatende steun en de grote bijdrage die je hebt geleverd bij de totstandkoming van dit proefschrift.

Veel promovendi (studenten) zijn in de afgelopen jaren gepromoveerd (afgestudeerd) in de leerstoel of zijn bezig hun promotie (studie) af te ronden. Veel van hen hebben mij gestimuleerd om te gaan promoveren en zijn daarom veel dank verschuldigd. Speciaal Doeco en Gertjan moet ik vermelden omdat ik juist bij hun onderzoek veel betrokken ben geweest. Ik ben dan ook bijzonder blij dat ze mij als paranimf begeleiden tijdens de laatste fase van de promotie.

Het onderzoek dat beschreven is in dit proefschrift kon niet tot stand komen zonder de samenwerking met andere researchgroepen. Het onderzoek betreffende $SrRuO_3$ is een samenwerking met de groep van prof. dr. Chang-Beom Eom (University of Wisconsin-Madison, USA). I thank Junghoon, Land and Chang-Beom for their scientific support. It was a pleasure to work with you. I'm sure that our collaboration will continue and will lead to more beautiful results. Het onderzoek betreffende $REBa_2Cu_3O_{7-\delta}$ is een samenwerking met de groep van prof. dr. Staf van Tendeloo (Universiteit Antwerpen, Belgie). De prachtige hoge-resolutie elektronen microscopie opnamen en de juiste analyse, gemaakt door Sara, hebben richting gegeven aan het onderzoek, bedankt hiervoor.

Wetenschappelijk onderzoek is niet mogelijk zonder de secretariële, administratieve en technologische steun. Deze heb ik vooral ontvangen in de leerstoel van Ans, Dick, Frank, Harry en Inke maar ook daarbuiten.

Tot slot bedank ik mijn directe familie, vrienden en kennissen voor hun interesse en mijn lieve Heidi, Pim en Daan voor hun onvoorwaardelijke liefde en steun. Hun geduld leek eindeloos. Ik hoop dat ik de zin “Nu even niet, papa moet werken op zolder” in de toekomst wat minder vaak hoef uit te spreken. Pim en Daan, leg de voetbal maar klaar.

Kortom, allen BEDANKT.